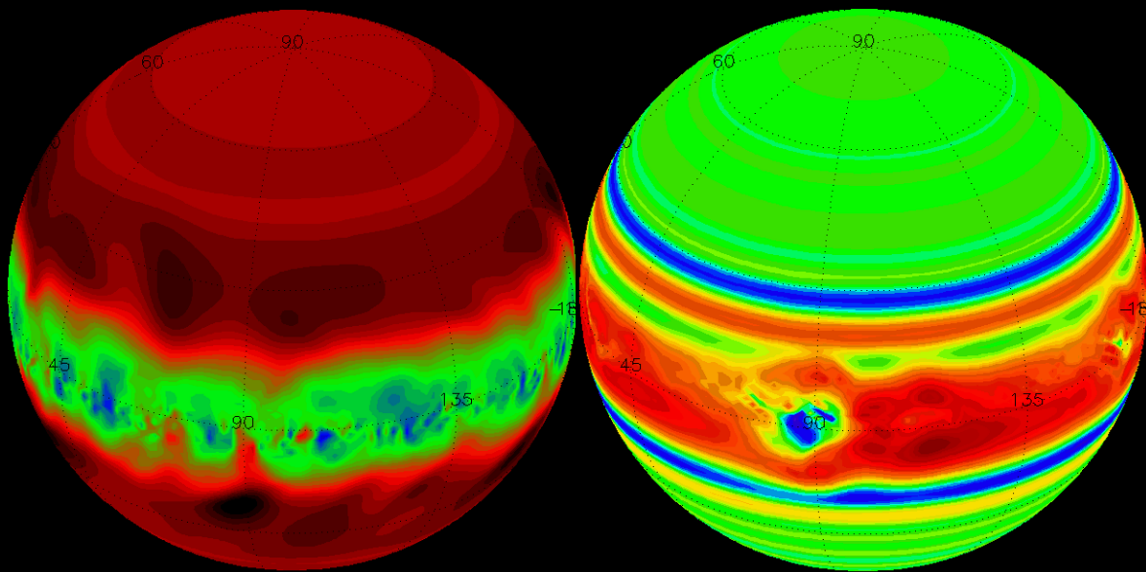


Three-dimensional modeling of the stratospheres of gas giants



Jisesh Ajitha Sethunadh

International Max Planck Research School
on Physical Processes in the Solar System and Beyond
at the Universities of Braunschweig and Göttingen

Three-dimensional modeling of the stratospheres of gas giants

vorgelegt von

Jisesh Ajitha Sethunadh
Master of Science in Physics
aus Kerala, Indien

Von der Fakultät II - Mathematik und Naturwissenschaften
der Technischen Universität Berlin
zur Erlangung des akademischen Grades
Doktor der Naturwissenschaften
Dr. rer. nat.

genehmigte Dissertation

Promotionsausschuss:

Vorsitzender: Prof. Dr. Mario Dähne
Gutachter: Prof. Dr. Heike Rauer
Gutachter: Dr. Paul Hartogh

Tag der wissenschaftlichen Aussprache: 17. February 2014

Berlin 2014
D 83

Bibliografische Information der Deutschen Nationalbibliothek

Die Deutsche Nationalbibliothek verzeichnet diese Publikation in der Deutschen Nationalbibliografie; detaillierte bibliografische Daten sind im Internet über <http://dnb.d-nb.de> abrufbar.

ISBN 978-3-944072-04-3

uni-edition GmbH 2014

<http://www.uni-edition.de>

© Jisesh Ajitha Sethunadh



This work is distributed under a
Creative Commons Attribution 3.0 License

Printed in Germany

Abstract

Stratospheres of giant gas planets of the Solar System (Jupiter and Saturn) extend above the cloud top layers near the tropopause to the lower thermosphere, and have a thickness of about 14 density scale heights. Their stratospheric dynamics are poorly understood, and are very distinctive from that of terrestrial-like planets due to peculiarities of the gas giants: the size, fast rotation, absence of solid surfaces, weak radiative forcing, and strong influence of the interiors.

The main objectives of this work were to develop a three-dimensional general circulation model (GCM) suitable for simulating the stratospheres of gas giants, and to apply it for studying the global circulations in the stratospheres of Jupiter, Saturn, and generic extrasolar planets. Such models are computationally demanding, because they have to resolve horizontal scales shorter than the Rossby deformation radii that are very small compared to the planet sizes. In addition, weak radiative forcing requires long-time integration for equilibration of the fields, and small time steps for maintaining the stability. The developed model is based on a grid-point dynamical core, and solves the nonlinear primitive equations under the hydrostatic approximation. It covers altitudes from 1–2 bars to 1–10 microbars, and uses the observed distributions of zonal winds at the cloud layers as a lower boundary condition.

Application of the GCM to the stratosphere of Saturn allowed to explore the sensitivity of the simulated fields to the numerical aspects like resolution, strength of horizontal diffusion, time-stepping algorithms. Further simulations were focused on studying the zonal mean circulation and the resolved wave activity on Saturn and Jupiter. They revealed, in particular, that the meridional transport on both planets is weak, and represents an upward extension of multiple cells imposed by the alternating zonal winds in the zones and belts at the lower boundary. The simulated mean fields and non-zonal disturbances were compared with available observations, and showed a good agreement in low latitudes, where the model resolution was the most sufficient.

The developed GCM was applied to studying the change of the circulation regimes on gas giants induced by an increased heating due to stellar radiation absorption. Such “warm” gas exoplanets have been found in large quantities at distances intermediate between those for cold and hot transiting giants. The analysis showed that the meridional transport intensifies on such planets, and most of the changes are due to the momentum deposited by vertically propagating thermal tides.

The developed GCM showed methodological suitability for studying atmospheric dynamics of giant gas planets under a variety of conditions. It represents a major step in developing model capabilities, and is in a great synergy with the planned Jupiter Icy Moon Explorer (JUICE) mission. The model can provide an insight into the stratospheric dynamics of Jupiter, and help with the interpretation of observational data.

Kurzfassung

Die Stratosphären der Gasriesen (Jupiter und Saturn) dehnen sich über 14 Skalenhöhen aus, mit der Tropopause, die knapp über den sichtbaren Wolken beginnt als Untergrenze und der Thermosphäre als Obergrenze. Die stratosphärische Dynamik ist bisher nur in Ansätzen verstanden und unterscheidet sich in vielen Punkten von derjenigen der terrestrischen Planeten, weil die Randbedingungen für den Antrieb der stratosphärischen Zirkulation der Gasriesen recht verschieden sind: Die Planeten sind größer, rotieren schneller, haben keine feste Oberfläche und absorbieren vergleichsweise wenig Energie von der Sonne. Sie setzen stattdessen Energie durch Vorgänge im Innern frei, die starken Einfluss auf die Zirkulation der Stratosphäre haben.

Das Ziel dieser Arbeit war, ein dreidimensionales allgemeines Zirkulationsmodell (engl. GCM) zu entwickeln, das die Stratosphären von Gasriesen simuliert und dieses Modell auf Jupiter, Saturn und extrasolare Planeten anzuwenden. Das Modell ist sehr rechenintensiv, weil es in der Lage sein muss, kleinere Strukturen als die Rossby Verformungsradien aufzulösen, was Rechnungen mit sehr hoher räumlicher Auflösung erfordert. Der schwache Strahlungsantrieb erfordert zudem aus Stabilitätsgründen kleine Zeitschritte und darüber hinaus lange Integrationszeiten bis die Felder ihren Gleichgewichtszustand erreicht haben. Das hier entwickelte Modell besteht aus einem dynamischen Gitterpunktkern und löst die nichtlinearen primitiven Gleichungen mittels hydrostatischer Näherung. Es deckt den Höhenbereich von 1-2 bar bis 1-10 μ bar ab und setzt die Verteilung der beobachteten zonalen Windgeschwindigkeiten an der oberen Wolkengrenze als untere Randbedingung an.

Die Anwendung des Modells auf die Saturnstratosphäre ermöglichte die Empfindlichkeit der simulierten Felder auf numerische Parameter wie Auflösung, Intensität der horizontalen Diffusion sowie der verwendeten Zeitschritt -Algorithmen zu untersuchen. Weitere Simulationen konzentrierten sich auf das Studium der mittleren zonalen Zirkulation sowie der räumlich aufgelösten Wellenaktivität in den Atmosphären von Jupiter und Saturn. Es zeigte sich, dass der meridionale Transport auf beiden Planeten nur schwach ausgeprägt ist und eine Aufwärtserweiterung der mannigfaltigen Zirkulationszellen darstellt, die durch die alternierenden zonalen Winde in den Zonen und Gürteln an der Untergrenze der Modellatmosphäre erzeugt werden. Die simulierten mittleren Felder und nichtzonale Störungen zeigten eine gute Übereinstimmung mit verfügbaren Beobachtungen, insbesondere in niedrigen Breiten, die vom Modell am höchsten aufgelöst werden.

Mit dem hier entwickelten GCM wurden zudem die Veränderungen der Zirkulationsregime von Gasriesen durch atmosphärische Erwärmung als Folge erhöhter Absorption solarer, bzw. stellarer Einstrahlung untersucht. Warme Gas-Exoplaneten wurden in großer Anzahl in Entfernungen entdeckt, die zwischen denen von kalten und heißen Gasriesen liegen. Die Analyse der Simulationen zeigt einen verstärkten meridionalen Transport, in erster Linie hervorgerufen durch Impulsübertrag vertikal wandernder thermischer Gezeiten.

In der vorliegenden Arbeit wurde die methodische Eignung des neuentwickelten GCM für das Studium der atmosphärischen Dynamik von Gasriesen aufgezeigt und ein großer Fortschritt in deren Modellierbarkeit erreicht. Die Fähigkeit, die Dynamik der Jupiteratmosphäre zu modellieren liefert neue Grundlagen und Perspektiven zur Interpretation von Beobachtungsdaten und zeigt eindeutige Synergien mit der JUICE (JUperiter ICy moon Explorer) Mission der ESA.

Contents

1	Introduction	15
1.1	General properties of the giant planets	16
1.2	Giant planets interiors and thermospheres	17
1.3	Giant planet atmospheres	19
1.3.1	Giant planet tropospheres	19
1.3.2	Giant planets middle atmospheres	21
1.4	Atmospheric dynamics of the giant planets	23
1.4.1	Characteristic length scales of the atmospheric flows	24
1.4.2	Waves	26
1.5	Turbulent flow on giant planets	27
1.6	Motivation	27
2	Model description	29
2.1	Outline of the model	29
2.2	Model grids	31
2.2.1	Horizontal discretization	31
2.2.2	Vertical discretization	33
2.3	Time stepping scheme and time filter	34
2.4	Boundary conditions	37
2.5	Dissipation terms	38
2.5.1	Subgrid-scale horizontal diffusion	38
2.5.2	Vertical diffusion	39
2.5.3	Molecular diffusion and thermal conduction	39
2.6	Computational aspects of the model - Polar values	39
2.6.1	Polar filters	39
2.7	Parameterization of the thermal forcing	40
2.8	Convective adjustment scheme	40
2.9	Other computational aspects	41
2.10	Simulations	41
3	Three-dimensional modeling of Saturn's middle atmosphere	45
3.1	Observational constraints on dynamics	45
3.2	Simulations	49
3.2.1	Experiments setup	49
3.2.2	Sensitivity to the diffusion coefficient	49
3.2.3	Higher resolution simulations	58

Contents

3.2.4	Wave activity in the middle atmosphere	63
3.3	Summary of results for Saturn stratosphere modeling	65
4	Three-dimensional modeling of Jupiter’s middle atmosphere	67
4.1	Observational constraints	67
4.1.1	Jovian troposphere	67
4.1.2	Middle atmosphere temperature	68
4.1.3	Winds and the meridional circulation	71
4.1.4	Previous simulation studies	73
4.2	GCM simulations	74
4.2.1	Experiments setup	74
4.2.2	Global circulation	76
4.2.3	Waves and non-zonal eddies	81
4.3	Summary of results for Jupiter stratosphere modeling	91
5	Simulations of extrasolar “warm” gas giant planets	93
5.1	Motivation	93
5.2	Formulation of the problem and experiment setup	96
5.3	Results of simulations	97
5.3.1	Cold giant	97
5.3.2	Cold giant with a latitudinal temperature gradient	99
5.3.3	Warm giant planet with diurnally varying irradiation	101
5.4	Summary of results for “warm” gas giant planet simulations	106
6	Conclusions	107
	List of symbols	109
	Bibliography	111

List of Figures

1.1	Observed wind speed on Jupiter’s cloud layer	18
1.2	The interior of Jupiter	18
1.3	Taylor’s columns	20
1.4	The Saturn great storm of 2010-2011	22
1.5	The spinning vortex of the Saturn’s north polar storm	22
1.6	Residual mean meridional circulation of the Earth atmosphere	23
2.1	The horizontal grids	32
2.2	The horizontal distribution of model variables	32
2.3	Charney-Phillips grid configuration of the model variables in vertical	33
2.4	Global view on the grid system	34
2.5	The standard Robert-Asselin filter and the modified family of filters	37
2.6	A flowchart describing the processes involved in the model	42
2.7	A flowchart describing author’s contribution	43
3.1	Profiles of equilibrium temperature and radiative relaxation time	47
3.2	Zonal wind applied at the lower boundary	48
3.3	The diffusion coefficient profiles used in the sensitivity simulations.	50
3.4	Simulated zonal mean temperature.	51
3.5	Latitude-longitude cross-section of temperature at 60 mb simulated with low diffusion coefficient.	51
3.6	Zonal mean temperature simulated with the high diffusion coefficient	52
3.7	Latitude-longitude cross-section of temperature at 60 mb simulated with the high diffusion coefficient.	52
3.8	Difference between the simulated zonal mean temperature in the runs with high and low diffusion coefficient.	53
3.9	Latitude-longitude cross-sections of temperature at 60 mb in simulations with high and low diffusion coefficient.	53
3.10	Simulation with the low diffusion coefficient	55
3.11	Simulation with the high diffusion coefficient	56
3.12	Difference between simulations with high and low diffusion.	57
3.13	Ratio of Rossby radius of deformation and grid length in the latitudinal direction for “high-resolution GCM setup”.	59
3.14	Ratio of Rossby radius of deformation and grid length in the meridional direction	59
3.15	A global view on the simulated Saturn atmosphere: zonal wind at 6 mb	60

List of Figures

3.16	Saturnian zonal mean temperature from the “high-resolution” simulation.	61
3.17	Latitude-longitude distribution of the simulated temperature at 60 mb in the “high resolution” run.	61
3.18	Higher resolution simulations of Saturn	62
3.19	Root-mean square variations of the simulated fields	64
4.1	Temperature and the thermal wind on Jupiter	69
4.2	Profiles of the equilibrium temperature and radiative relaxation time . . .	70
4.3	Jupiter’s radiative heating and cooling due to minor atmospheric components	70
4.4	Equilibrium temperature profile and heating balance	71
4.5	Distribution of the zonal mean wind used for nudging the model at the lower boundary of the model.	72
4.6	Ratio of Rossby radius of deformation and grid length in the latitudinal direction for the “high-resolution GCM setup”.	75
4.7	Ratio of Rossby radius of deformation and grid length in the meridional direction	75
4.8	A global view on the simulated Jupiter atmosphere	77
4.9	Latitude-altitude cross-section of the simulated Jovian zonal mean temperature.	78
4.10	Latitude-longitude cross-section of the simulated temperature at 60 mb. .	78
4.11	Simulated fields on Jupiter	79
4.12	Residual meridional circulation and residual vertical velocity	80
4.13	Chevrons on Jupiter	82
4.14	Latitude–longitude distribution of streamlines at 20 mb	82
4.15	Longitude-height cross-sections of the simulated temperature	83
4.16	Northern Jovian stratosphere in the UV	84
4.17	North polar stereographic plot of the simulated zonal wind at 15 mb. . . .	84
4.18	Longitude–height cross-sections of the simulated non-zonal disturbances .	85
4.19	Longitude–height cross-sections of the simulated zonal wind	85
4.20	Latitude–longitude cross section of the simulated temperature	86
4.21	Latitude–longitude cross-section of the simulated temperature deviations from the zonal mean.	87
4.22	Temporal variations of the simulated temperature	88
4.23	Equatorial oscillations of the simulated fields	89
4.24	Root-mean square variations of the simulated fields	90
5.1	An illustration of the warm gas giants orbit	93
5.2	Simulation with the imposed meridional gradient and diurnal temperature variations	94
5.3	Residual vertical velocities and simulated zonal mean temperature	95
5.4	One-day averaged fields from the simulation for the cold giant	98
5.5	Longitude-height cross-sections of the simulated non-zonal disturbances .	100
5.6	Latitude-height cross-sections of the fields simulated	102
5.7	Snapshot showing the applied diurnally varying irradiation	103

5.8	Simulation with the imposed meridional gradient and diurnal temperature variations	104
5.9	Simulation with the imposed meridional temperature gradient and diurnal temperature variations	105

List of Tables

1.1	Basic parameters of Jupiter and Saturn used in the model	16
1.2	The energy balance of the outer planets	17
1.3	Standard nomenclature for the belts and zones of Jupiter	19
1.4	A comparison of basic parameters of planets and satellites	25

1 Introduction

The giant planets (also called “Jovian planets” or “gas giants”) are rapidly rotating outer planets of the Solar System, which have very large planetary radii compared to Earth, and no obvious surface. This study is focused on Jupiter and Saturn-like planets, and does not consider icy giants like Uranus and Neptune. Jupiter, the largest planet of the Solar System, is named after the Roman god, and has been well-known to ancient times astronomers. This is evident from many available historic observations of Jupiter, which date back to hundreds of years. Thus, the giant storm on Jupiter “the Great Red Spot” is known to have existed since 17th century. This demonstrates that Jupiter has been an interesting object for older-times astronomers. Despite being very far, Jupiter can be seen as a faint banded disc even by using primitive telescopes. The second largest giant planet of the Solar System, Saturn (also named after the Roman god Saturn), was first observed through telescope by the Italian astronomer Galileo Galilei in 1610. Later in 1659, the Dutch astronomer Christian Huygens discovered its rings.

The exploration of gas giants has a very rich history. Historically, the speed and banded structure of the zonal winds were studied by means of low resolution telescopic observations only. Today, there is a multitude of ground-based and space-borne observations of the gas giants. Recent advances in technology allowed the gas giants to be heavily explored in detail. For instance, the atmospheric entry probe of the Galileo mission was by far one of the most direct attempts to measure the interior properties of giant planets. High-resolution measurements of temperature fields and trace gases from recent space missions extended our knowledge of the gas giants atmospheres. Space missions to both Jupiter and Saturn include Pioneer 11, Voyager 1, Voyager 2 and Cassini. Other missions to Jupiter are Pioneer 10, Galileo, Ulysses, New Horizons, and an ongoing mission Juno. Even though there were many attempts to understand the properties of the middle atmospheres of gas giants, its circulation remains to a large extent a mystery.

To unfold the mysteries of Jupiter and its moons, a new mission “JUICE” (stands for Jupiter Icy Moon Explorer) has been proposed (Grasset et al. 2013). This new large-scale mission will observe Jupiter and its largest moons. This work is in a great synergy with the proposed mission. The newly developed in the course of this study general circulation model (GCM) can provide an insight into the dynamics of the least explored atmospheric region, and may help with the interpretation of observational data on the gas giants. Besides that, the atmospheric dynamics of fast rotating giant gas planets is quite different from that of the better known terrestrial-like planets. Understanding it is a great scientific task. Moreover, studying the dynamics of such planets with GCMs is quite challenging from the technical point of view, and, thus, motivates the development of the GCM modeling technology. For the fundamental fluid dynamics reasons outlined further, the resolution of the appropriate GCMs must be very high. Weak radiative forcing requires

long simulations, while high-speed winds demand short time steps due to stability concerns. All this makes simulations of atmospheric circulation of the gas giants with GCMs very difficult, since they call for huge amounts of computer resources. Taking together, this work represents an important step toward resolving an important and overarching scientific goal - understanding the mystery of the atmospheric dynamics of giant gas planets.

1.1 General properties of the giant planets

The gas giants differ from inner planets in many ways. Notable features include ring systems, lack of solid rock surface, abundance of moons, and fast rotation. The physical properties of Jupiter and Saturn used in the model and corresponding physical properties of Earth are given in Table 1.1. The giant planets show differential rotation, because they are not solid bodies. For example, the rotation of Jupiter’s polar atmosphere is ≈ 5 minutes longer than that of the equatorial atmosphere. Jupiter’s radio rotation period (System III) corresponds to the mean rotation period of the planet’s magnetosphere, and is, generally, considered as the official rotation period. This rotation of magnetic field shows how fast the planet’s interior spins, because the magnetic field originates in the planet’s core. Wind speeds on Jupiter are normally measured with respect to System III. Upwelling chromophores (organic and non-icy materials) are another interesting feature of gas giants, which can give an important information about the interior circulation patterns. The biggest giant planet, Jupiter, has four large natural satellites known as “The Galilean satellites” discovered by Galileo Galilei, and a number of much smaller moons. Saturn also has a number of small moons, and the second-largest moon in the Solar System, Titan.

Parameter	Jupiter [♃]	Saturn [♄]	Earth [♁]
Radius at 1 bar, a (km)	71,492	60,268	6,378
Mass(10^{24} kg)	1,898	568	5.973
Mean density (kg/m^3)	1,326	687	5,515
Density at 1 bar (kg/m^3)	0.16	0.19	1.225
Gravity, g (m/s^2)	24.79	10.44	9.81
Atmospheric scale height, H (km)	27	60	7.4
Length of Year	11.86 Earth years	29.46 Earth years	1
Length of Day	9 hours, 55 minutes	10 hours, 40 minutes	23 hours, 56 minutes
Obliquity (deg)	3.13	26.73	23.44
Planetary angular velocity, Ω (rad s^{-1})	1.75×10^{-4}	1.64×10^{-4}	7.29×10^{-5}
Specific gas constant, R ($\text{J kg}^{-1} \text{K}^{-1}$)	3605.38	3757.2	287.10
Specific heat capacity, C_p ($\text{J kg}^{-1} \text{K}^{-1}$)	12359.1	12619.0	1004.0

Table 1.1: Basic parameters of Jupiter and Saturn used in the model

1.2 Giant planets interiors and thermospheres

The gas giant's gaseous material atmosphere becomes denser with depth. The interiors of these planets are primarily composed of liquid metallic hydrogen, contain ionized atoms, protons and electrons, which makes the interior electrically conducting. The strong deep interior convection of metallic-hydrogen generates the strong magnetic field of Jupiter.

There are many obstacles for getting information about the deep interior of the giant planets. Most important among them are tropospheric opaque cloud layers, which block the interior view of the planets, magnetic fields and high interior pressure. The zonal wind structure (see Figure 1.1) and circulation pattern of giant planets are known at the tropospheric levels only, because the circulation was inferred by using the motions of tropospheric clouds. Measurements of internal properties of Jupiter by the atmospheric entry probe of the Galileo mission could not accomplish *in situ* beyond 200 km below the cloud tops because of the high level of internal heat flux. A schematic of the interior structure of Jupiter is depicted in Figure 1.2. Details of the interior structure of giant planets are largely unknown due to the lack of measurements.

The giant planets radiate more energy than they receive from the Sun. This implies a strong generation of internal energy by the interiors. The extra energy is generated via gravitational contraction (Kelvin-Helmholtz mechanism through adiabatic contraction,) which leads to shrinking the planet by ~ 2 cm each year, continued cooling of residual heat left over from the collapse of the primordial nebula from which the planet has formed, thermal energy generated by conversion of gravitational energy produced by settling heavy elements towards the center, and radioisotope heating and demixing of helium from metallic hydrogen. Knowledge about the interior structure of the giant planets can provide important information about the formation of the Solar System. The total energy emitted by the giant planets was estimated by Ingersoll (1990). The measured values constituting the radiative balance are shown in Table 1.2.

Parameter	Jupiter [24]	Saturn [25]
Geometric albedo	0.274 ± 0.013	0.242 ± 0.012
Bond albedo	0.343 ± 0.032	0.342 ± 0.030
Absorbed power, 10^{16} W	50.14 ± 2.48	11.14 ± 0.50
Emitted power, 10^{16} W	83.65 ± 0.84	19.77 ± 0.32
Energy balance	1.67 ± 0.09	1.78 ± 0.09
Effective temperature, K	124.4 ± 0.3	95.0 ± 0.4
Internal power, 10^{16} W	33.5 ± 2.6	8.63 ± 0.60
Internal energy flux, 10^{-4} W/cm ²	5.44 ± 0.43	2.01 ± 0.14
Internal power/unit mass, 10^{-11} W/kg	17.6 ± 1.4	15.2 ± 1.1

Table 1.2: The energy balance of the outer planets, as determined from Voyager IRTS-Data (adapted from Table 7 of Pearl and Conrath (1991))

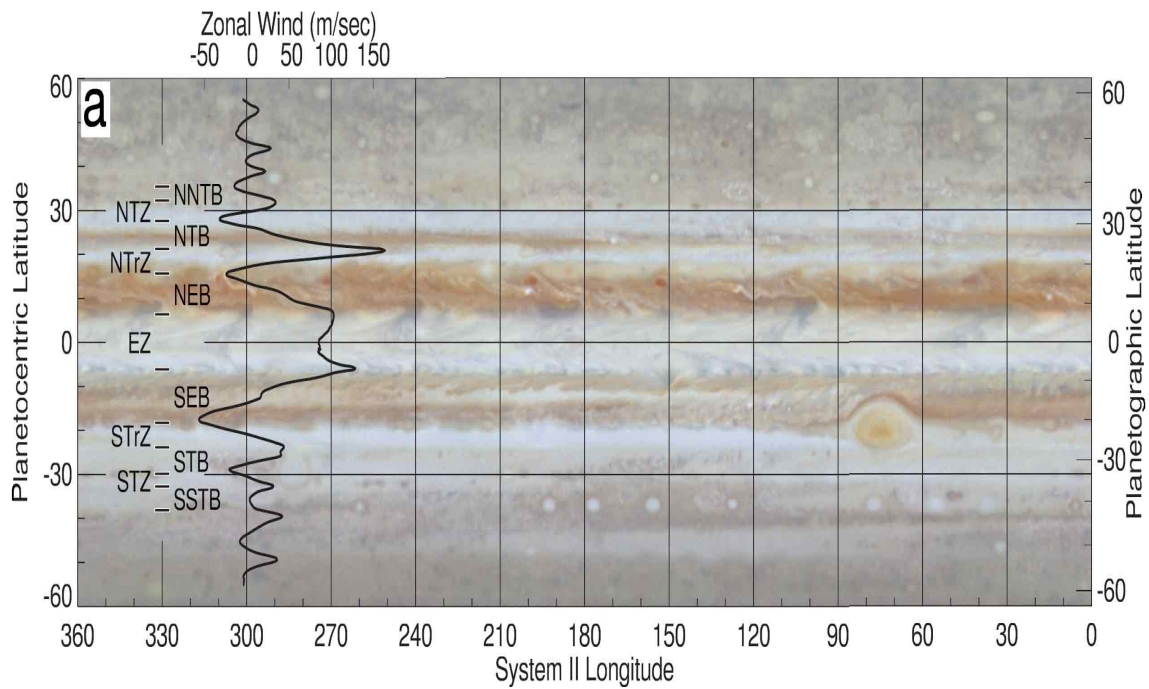


Figure 1.1: Observed wind speed on Jupiter's cloud layer. (Image: reproduced from Bangen et al. (2004) / ©Cambridge Univ. Press 2004)

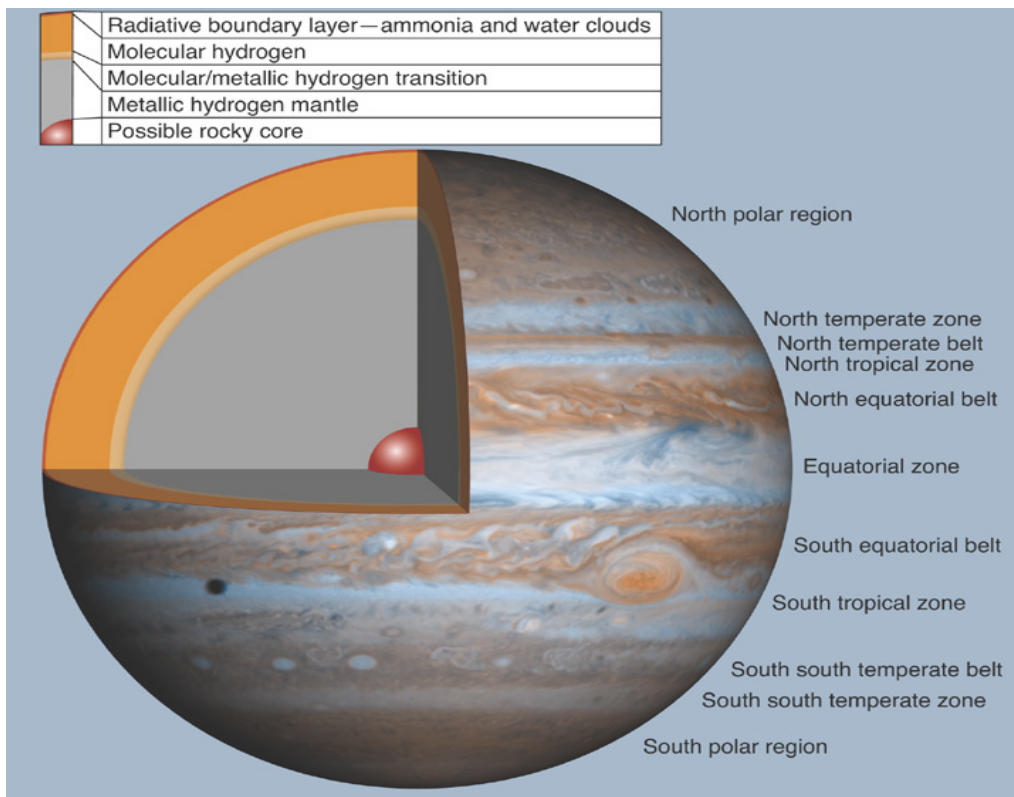


Figure 1.2: The interior of Jupiter. (Image: reproduced from Bangen et al. (2004) / ©Cambridge Univ. Press 2004)

SSTB	South South Temperate Belt
STZ	South Temperate Zone
STB	South Temperate Belt
STrZ	South Tropical Zone
SEB	South Equatorial Belt
EZ	The Equatorial Zone
NEB	North Equatorial Belt
NTrZ	North Tropical Zone
NTB	North Temperate Belt
NTZ	North Temperate Zone
NNTZ	North North Temperate Zone

Table 1.3: Standard nomenclature for the belts and zones of Jupiter (Vincent et al. 2000)

1.3 Giant planet atmospheres

The atmospheres of Jupiter and Saturn are primarily made up of hydrogen-helium gas ($\approx 87\%$ of the total mass). The gas giants atmospheres are very dynamically active regions, and even show Earth-sized turbulent structures. There are many interesting features observed in their atmospheres. They include banded structure of zonal jets (see Figure 1.1), observed lightning on Saturn and Jupiter (Cook et al. 1979, Gibbard et al. 1995), Jupiter's Great Red Spot (GRS), observed large-scale waves and gravity waves on Jupiter (Reuter et al. 2007, Arregi et al. 2009, Flasar and Gierasch 1986), Saturn's huge storm and polar hexagon (see Figures 1.4 and 1.5), etc. The amount of intrinsic heat fluxes generated by the giant planets is approximately equal to the solar energy they receive. Hence, the dynamics of the giant planet stratospheres are assumed to be controlled approximately equally by intrinsic heat and solar radiation. Like on other planets, the upper atmospheres show high temperatures, which reach extremely large values in the thermosphere. The thermospheric structure and dynamics of gas giants are strongly influenced by auroral and Joule heating. Temperatures in the thermosphere grow sharply with height. For example, there is a 700-Kelvin temperature increase in the Jovian thermosphere. There are several mechanisms proposed to explain this steep rise, one of which is associated with gravity waves in this region (Young et al. 1997, 2005). However, there are contradictory views about the gravity wave dissipation in the thermosphere and their thermal effects (Hickey et al. 2000, Schubert et al. 2003).

1.3.1 Giant planet tropospheres

The tropospheres of giant planets differ in many ways from that of terrestrial planets. The maximum wind speed of hurricanes on terrestrial planets is about 110 m s^{-1} . On the other hand, the wind speed on gas giants can be much higher. For example, on Saturn, the maximum wind speed can reach about 500 m s^{-1} . There are no direct wind speed measurements in the atmospheres of gas giants, but the tropospheric circulation can be inferred by tracking visible cloud features as a proxy (Del Genio and Barbara 2012). The cloud layer on Jupiter is $\sim 50 \text{ km}$ deep. Available Jupiter cloud observations include

ground based thermal-infrared measurements, Hubble Space Telescope (HST) and various space missions. In the case of Saturn, even though the rings make it difficult to get a full planet view, thermal-infrared, HST and various space missions observations do exist. The opacity of the lower atmospheres and tropospheres are high. In this atmospheric regions, convection plays a major role in the transfer of heat. The turbulent eddies and atmospheric waves are also assumed to play a vital role in the poleward transport of heat. The alternating eastward and westward high speed jets, which form the banded structure in the Jupiter troposphere, is shown in Figure 1.1, and the standard nomenclature of the jets is given in Table 1.3. To date, it is not clear what drives these zonal jets. There are several theories proposed for explaining them. They are briefly summarized below.

Deep winds hypothesis

The deep wind hypothesis suggests that the zonal winds originate due to the thermal convection of the deep hydrogen-helium interior of the planet, and are projections of the Taylor columns, which can be explained via the Taylor-Proudman theorem (Busse 1976, Christensen 2001, Aurnou and Olson 2001, Busse 2002, Heimpel et al. 2005, Vasavada and Showman 2005). This theorem holds good for barotropic liquid. Figure 1.3 shows an illustration of Taylor's columns parallel to the axis of rotation.

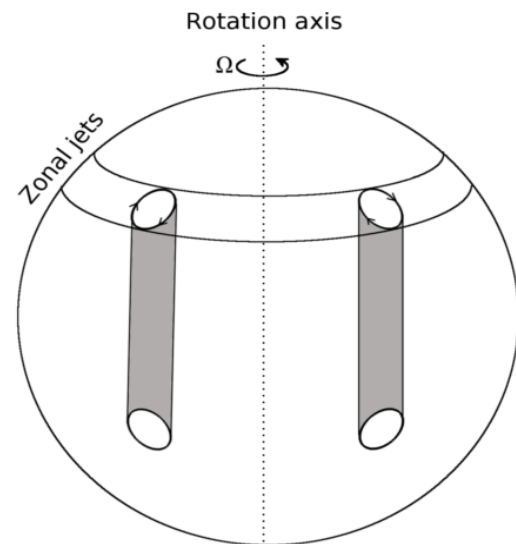


Figure 1.3: Taylor's columns

Weather layer mechanism

The weather layer mechanism assumes that zonal winds take place only in a thin (compared to the large planetary radius) outer layer, and the jets are driven directly in this shallow layer by the latitudinal gradient of solar heating (differential heating) (Gierasch et al. 1986, Gierasch and Conrath 1993, Cho and Polvani 1996, Showman et al. 2006, Vasavada and Showman 2005) or inverse cascade of two dimensional turbulence energy from small scale to large scale based on the Rhines scale (Rhines 1975, Ingersoll, A. P. et al. 2004).

Moist convection hypothesis

Recently it was proposed that the moist convection can drive the jets on Jupiter (Ingersoll et al. 2000, Lian and Showman 2010). Moist convection is a very common process in the Earth atmosphere. When water vapor rises up and condenses, latent heat releases, and can produce heavy clouds and thunderstorms. The released latent heat causes intense upward motions that are transformed into vortices due to the Coriolis force and turbulent effects. Powerful storms can develop from latent heat generated by moist convection. There are

observations of Jupiter's and Saturn's atmospheres showing thunderstorm activities (Banfield et al. 1998, Gierasch et al. 2000, Hueso and Sánchez-Lavega 2004, Dyudina et al. 2004, Porco et al. 2003).

Increase of the wind speed with depth in the vertical profile retrieved by the Galileo probe (Atkinson et al. 1996, Atkinson et al. 1998) supports the hypothesis that the zonal winds originate in the deep interior of Jupiter. The zonal wind generation in the tropospheres of gas giants is a very debatable topic. For instance, although Jupiter receives more sunlight and has more internal heat than Saturn and Neptune, the wind speeds are only 1/3 of that on Saturn and Neptune. Tropospheres of the giant planets are very active regions. Vortex generation and their interactions are very frequently observed phenomena (Sanchez-Lavega et al. 2001, Sánchez-Lavega et al. 2012). Turbulence, wave activity and eddies also play a role in shaping the circulation patterns.

There are GCM studies, which successfully reproduced the banded zonal wind structure of Jupiter (Heimpel et al. 2005). However, our study is mainly focused on the middle atmosphere. Therefore, to circumvent the uncertainties with the generation and maintenance of the zonal wind in the troposphere, we place the lower boundary of our GCM at approximately cloud top layers in the troposphere, and employ the well-known distributions of the zonal wind as a lower boundary condition.

1.3.2 Giant planets middle atmospheres

Stratospheres are convectively stably stratified regions between the tropopause and stratopause. For Jupiter the upper border of the middle atmosphere often is also called mesopause in the literature, although there is not pronounced mesosphere. In case of gas giants, they represent the whole middle atmospheres, because the latter lack mesospheres. Stratospheres extend for ≈ 322 km (from ≈ 280 mbar to ≈ 0.001 mbar) on Jupiter, and for Saturn ≈ 700 km (from ≈ 100 mbar to ≈ 0.001 mbar). There are no visible cloud features in the stratospheres of gas giants, and their observations are not straightforward as is the case with the "weather-layer" near the tropopauses. The middle atmosphere of giant planets are dominated by molecular hydrogen, but the presence of aerosols and heavier radiatively active gas constituents affect temperature variations. There are space and ground based observations, which clearly show latitudinal temperature dependencies in the middle atmospheres. In the stratosphere, thermal forcing associated with absorption of the solar radiation and emission in infrared dominates the convective forcing from below. Thus, the observed temperatures are maintained by radiative forcing tending to bring temperatures to local radiative equilibrium values, and by dynamics that drive temperatures away from the balance.

The middle atmosphere of Jupiter is heated mainly by absorption of solar radiation in mid-infrared wavelengths of methane (CH_4), and is cooled due to emission in vibrational bands of ethane (C_2H_6), acetylene (C_2H_2) and methane (Moreno and Sedano 1997, Yelle et al. 2001). There are other minor gas constituents, which radiation can be used for inferring the information about the stratospheres, but whose contribution to the energy balance is negligible. The radiative processes on Saturn are very similar; a major part of the diabatic heating is due to methane and cooling by ethane, acetylene and methane (Bézard et al. 1984).

Other factors that determine variations of the stratospheric temperatures are attributed

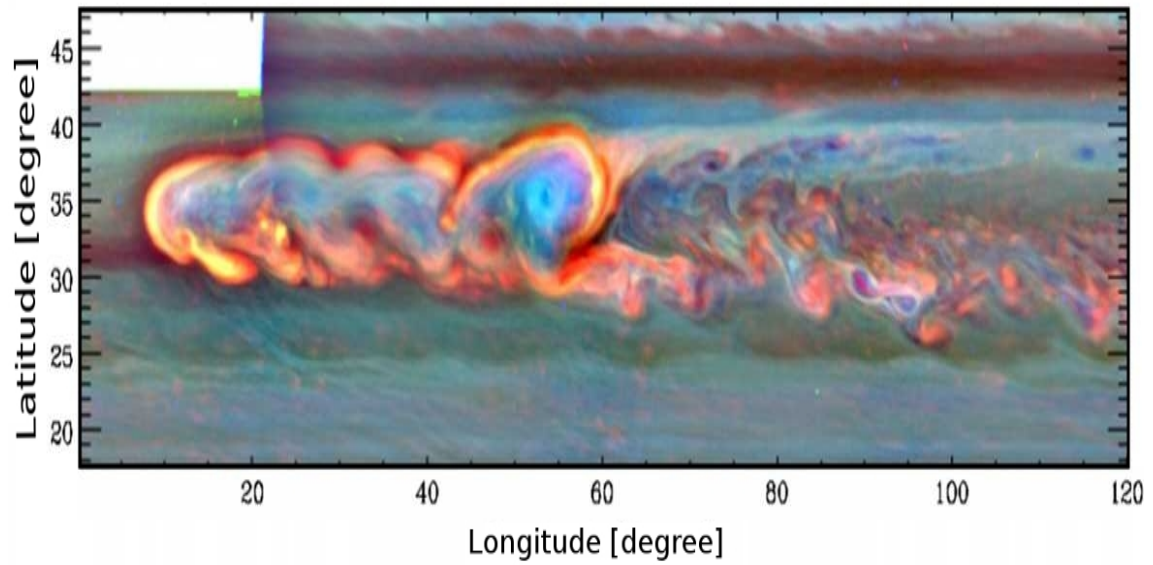


Figure 1.4: The Saturn great storm of 2010-2011: full-longitude mosaic of Saturn's northern mid-latitudes on January 11, 2011. (Image: reproduced from Figure 5 of Sayanagi et al. (2013))

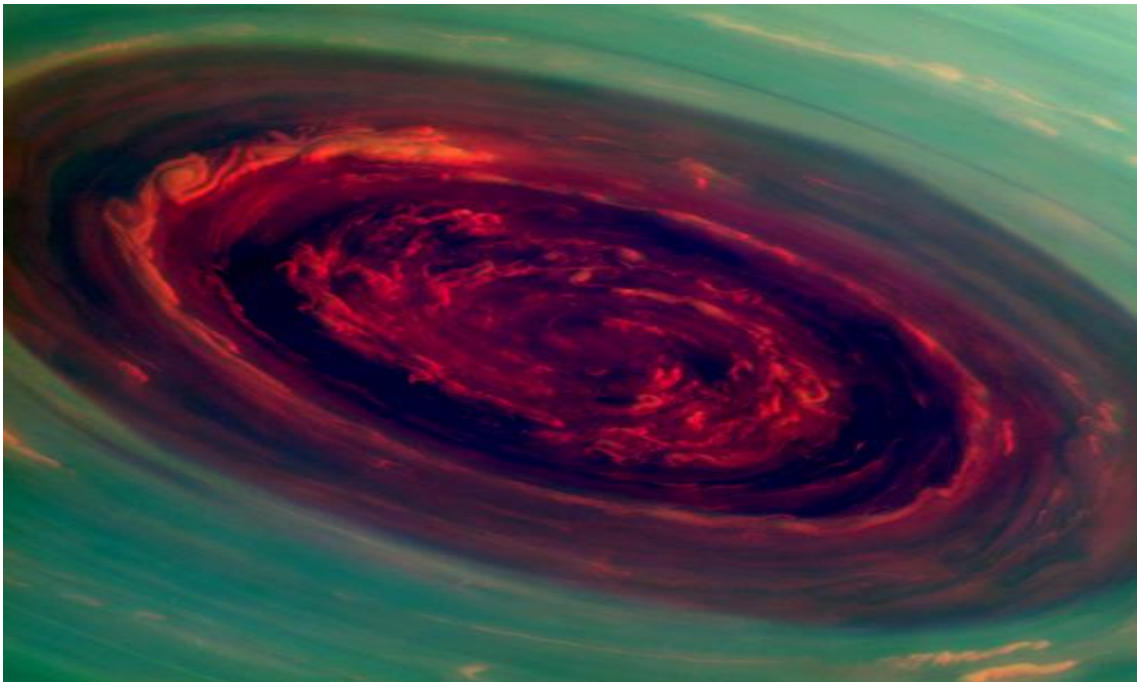


Figure 1.5: False color image of the spinning vortex of the Saturn's north polar storm captured by Cassini. The wind speed can reach $\approx 150 \text{ m s}^{-1}$. (Image credit: NASA/JPL-Caltech/Space Science Institute)

to inhomogeneously reflected sunlight from the cloud top, thermal emission from the interior, inhomogeneous heating and cooling due to absorption and emission by aerosols, adiabatic cooling and heating due to upwelling and subsidence of the air, correspondingly. Additional forcing in the stratosphere is associated with gravitational tides produced by the massive and innermost satellites (Ganymede, Callisto, Io, Europa etc), and with tropospheric storms (Fletcher et al. 2012).

1.4 Atmospheric dynamics of the giant planets

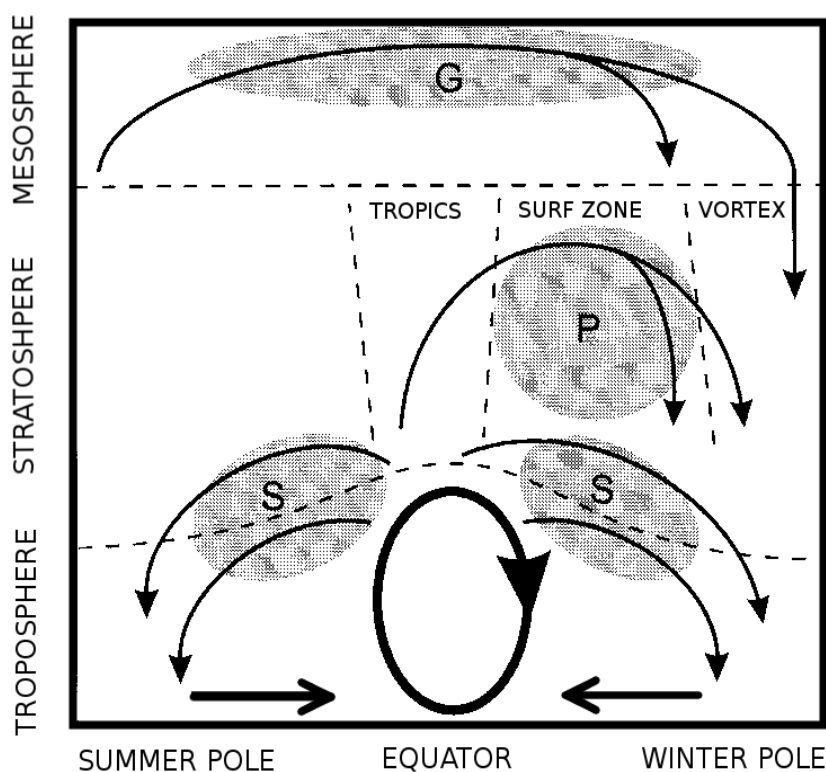


Figure 1.6: Schematic of the residual mean meridional circulation of the Earth atmosphere. The heavy ellipse denotes the thermally-driven Hadley circulation in the troposphere. The shaded regions (labeled S, P, and G) denote regions of breaking waves (synoptic- and planetary-scale waves, and gravity waves, respectively), responsible for driving the branches of the stratospheric and mesospheric circulation. (Adapted from Figure 2: Plumb (2002))

Atmospheric dynamics in the tropospheres and stratospheres of Jupiter and Saturn are rich and complex. There is a variety of dynamical phenomena of different spatial and temporal scales. The prominent observed large-scale features include the observed hemispheric asymmetry of tropical jets, belt-zone temperature differences and decrease of the wind pattern above the cloud level. One of the most important characterizations of the global dynamics of planetary atmospheres is the meridional circulation, which shows

a zonally symmetric (“zonal-mean”) transport of air masses, heat, and tracers. Because the Navier-Stokes equation that describes atmospheric motions is non-linear, its zonally-averaged form includes the forcing by correlations of deviations from the zonal-means (so-called “eddy forcing”) in addition to the forcing by zonally-averaged heating/cooling. Therefore, smaller-scale dynamical phenomena may have a profound effect on the global circulation. This influence in the middle atmosphere of Earth is schematically illustrated in Figure 1.6. The terrestrial stratospheric Brewer-Dobson circulation (Brewer 1949, Dobson 1956), which is, in particular, responsible for transport of ozone and surplus of heat from the tropical upper stratosphere to high latitudes, is forced by waves propagating from the troposphere. Near the tropopause, the circulation is driven by synoptic-scale (few thousand km horizontal scales) disturbances. The transport in the stratosphere is strongly influenced by planetary-scale Rossby waves, while the mesospheric meridional circulation is forced almost entirely by dissipating gravity waves.

On Jupiter and Saturn, the inhomogeneous heating and dynamic instability of atmospheric flows give rise to eddies of various scales. These eddies affect the large scale global circulation, which is largely unknown in the stratospheres of gas giants. Equally, the eddy statistics above the cloud-top level is not yet quantified from observations. This makes GCMs a very powerful tool for investigating wave-mean flow interactions numerically.

1.4.1 Characteristic length scales of the atmospheric flows

The peculiar features of the global circulation on gas giant planets, which differ from large-scale atmospheric dynamics of terrestrial-like planets, based on scaling arguments are illustrated below.

Rossby radius of deformation

The Rossby radius of deformation (Charney and Flierl 1981, Gierasch and Conrath 1993, Yano 1994) is the fundamental length scale, which must be carefully considered in planetary atmospheric simulations. The buoyancy force dominates the inertia for motions with the horizontal extent shorter than the Rossby radius of deformation. The latter is intimately linked with the length scale of unstable waves in stratified sheared flows. Formation and break-ups of vortices occur at scales shorter than the Rossby radius. These disturbances have vertical structures, sometimes propagate vertically, and have a profound effect on the general circulation of planets. To simulate wave-mean flow interactions properly, GCMs must resolve motions shorter than the Rossby radius of deformation. Thus, the latter gives an estimate of the lowest possible resolution of a GCM.

The Rossby radius of deformation is given by

$$L_D = NH/f \propto T/gf, \quad (1.1)$$

where:

$f = 2\Omega \sin \phi$	Coriolis parameter
H	Density scale height
T	Characteristic temperature
$N = \sqrt{\frac{g}{\theta} \frac{d\theta}{dz}}$	Brunt-Väisälä frequency (buoyancy frequency)
g	Acceleration of gravity
θ	Potential temperature

It is seen that L_D is small for cold (small T), fast-rotating (large f), and massive (large g) planets like gas giants. The appropriate resolution of GCMs must be accordingly fine. Using the values from Table 1.4 one can obtain $L_D \approx 3100$ km for Jupiter (Yano 1994), and $L_D \approx 7500$ km for Saturn at latitude $\phi = 30^\circ$. The Rossby radius of deformation on Saturn is ~ 2.4 times larger than that for Jupiter, mainly due to a larger characteristic scale height H . The radius of Saturn is $\sim 15\%$ smaller than for Jupiter, which means that correspondingly lower resolution (in radians) is required to resolve the same horizontal lengths. Small grid size and large planetary radius a mean that the number of grid points in a GCM should be greater for giant planets. The ratio L_D/a is a good characteristic, which illustrates this dependence.

Planet	a (10^3 km)	Ω (rad s $^{-1}$)	gravity (ms $^{-2}$)	T_{eff} (K)	H (km)	U_c (ms $^{-1}$)	L_D/a	L_β/a
Venus	6.05	3×10^{-7}	8.9	232	5	20	70	7
Earth	6.37	7.27×10^{-5}	9.82	255	7	20	0.3	0.5
Mars	3.396	7.1×10^{-5}	3.7	210	11	20	0.6	0.6
Titan	2.575	4.5×10^{-6}	1.4	85	18	20	10	3
Jupiter	71.492	1.7×10^{-4}	24.79	124	27	40	0.03	0.1
Saturn	60.268	1.65×10^{-4}	10.44	95	60	150	0.03	0.3
Uranus	25.56	9.7×10^{-5}	8.7	59	25	100	0.1	0.4
Neptune	24.76	1.09×10^{-4}	11.1	59	20	200	0.1	0.6

Table 1.4: A comparison of basic parameters of planets and satellites (partially adapted from (Showman et al. 2010)). Here U_c is the characteristic horizontal wind speed and T_{eff} is the global average blackbody temperature.

It is seen from Table 1.4 that the required number of grid points in GCMs along one horizontal dimension is by an order of magnitude larger on Jupiter and Saturn ($L_D/a = 0.03$) than on Earth or Mars ($L_D/a = 0.3$ to 0.6). For covering the globe, gas giant GCMs require two order of magnitude more grid points than a comparable terrestrial GCM. This makes the atmospheric general circulation modeling of gas giants the most computationally expensive. For comparison, the least computationally expensive GCMs are for Venus ($L_D/a = 70$) and Titan ($L_D/a = 10$).

Rhines scale

The Rhines scale (Rhines 1975, Gierasch and Conrath 1993) is the characteristic length scale, which determines the size of flow structures in processes like merging of small vortices to form large flow structures - a process known as inverse energy cascade. When

the structures reach a certain size, energy begins to flow into Rossby waves as the inverse cascade becomes arrested, and the size of flow structures is maintained. The wave number of this jet is given as

$$k_\beta = \sqrt{\frac{\beta}{U}}. \quad (1.2)$$

Turbulent dominated small scale dynamics become Rossby waves dominated dynamics after reaching the wavenumber k_β . The Rhines scale characterizes small-scale atmospheric flows, which can influence large-scale circulation as well. Many of the observed flow structures in planetary atmospheres have sizes similar to the Rhines scale length. As the horizontal extent of the flow becomes close to the Rhines scale, the vortices grow more in the east-west direction than in the north-south one. This is because the Rhines length scale is larger in the east-west direction than the north-south direction.

The Rhines length scale is given by

$$L_\beta = \pi/k_\beta = \pi \sqrt{\frac{U}{\beta}}, \quad (1.3)$$

where:

- U Root mean square fluid velocity
- β Latitudinal northward gradient of the Coriolis parameter, $(2\Omega \cos \phi)/a$
- Ω Planetary rotational frequency
- ϕ Latitude
- a Radius of the planet

The Rhines scale length for Jupiter and Saturn is ≈ 10000 km. An important characteristic of the circulation is the ratio of the Rhines scale and the planetary radius. As is seen from Table 1.4 (last column), the number of tropospheric zones and bands (alternating jets) can be estimated pretty good for various planets.

1.4.2 Waves

Eddies are the vortices and waves that superimpose the mean flow. They can be found in atmospheric fields after the zonal means are subtracted. There exist a range of waves on the atmospheres of gas giants. There are observations and measurements of waves from small-scale gravity waves (Smith et al. 1979, Flasar and Gierasch 1986, Simon-Miller et al. 2012) to planetary-scale waves on Jupiter (Flasar and Gierasch 1986, Sanchez-Lavega et al. 1998, Allison 1990, Li et al. 2006b), Jupiter's south polar wave, etc. On the other hand, Saturn shows a "hexagonal" planetary wave with a vortex at the North Pole (Baines et al. 2009) and large-scale thermal waves in the upper troposphere (Achterberg and Flasar 1996). It has been suggested that the Saturn's hexagon is a manifestation of the retrograde Rossby wave. Rossby waves are planetary-scale waves, in which the restoring force acting against the pressure gradient force is the latitudinal gradient of the Coriolis force (β -effect). They are dispersive waves (phase speed depends on wave number, that is harmonics with different frequencies travel at different speeds. Thus, the group and phase velocities are different). Rossby waves propagate westward in the absence of

the mean flow, and their phase speeds increase with increase of the wavelength. Planetary waves must be properly resolved and reproduced in GCMs. A study of Rossby wave propagation using different grids was performed by Gavrilo and Tošić (1998). In particular, they showed that the Arakawa B-grid is better suitable for reproducing Rossby waves compared to other types of finite difference approximations. This result has influenced our decision to employ the B-grid in the current version of the GCM.

Vertically propagating gravity waves also play a very important role in the vertical transport of energy, heat and momentum. Gravity waves are dispersive waves in which the restoring force is gravity. Once they reach low density regions, they break and/or dissipate, and deposit their momentum to the mean flow. Gravity waves also induce cooling or heating upon their dissipation.

1.5 Turbulent flow on giant planets

One of the important dimensionless parameters characterizing the influence of viscosity is the Reynolds number. The expression for it is given by

$$Re = \frac{LV}{\nu}, \quad (1.4)$$

where:

- L Characteristic length scale
- V Characteristic velocity of the flow
- ν Kinematic viscosity of the fluid

In the model, the Reynolds number is merely the ratio of advection and the imposed diffusion in the momentum equation. On gas giants, the characteristic scale length is very large, whereas the diffusion term is small. This implies very large Reynolds numbers, and a possibility for developing turbulent flows. Kinetic energy loss in such flows may occur via turbulence, which slow down the jets.

1.6 Motivation

Despite the wealth of observations is available, and the gas giants are continuously and intensively explored for a long time, the stratospheric circulations on Jupiter and Saturn still remain largely unknown. Modeling studies of the stratospheres of these planets mainly include two-dimensional models (Conrath et al. 1990, West et al. 1992, Williams 2003), although few three-dimensional models have been proposed recently (Dowling et al. 1998, Yamazaki et al. 2004). As follows from the previous sections, the use of two-dimensional models in former studies was dictated to a large degree by the computational limitations. These models included only limited aspects of the stratospheric features of gas giants. Many limitations of stratospheric models are caused by uncertainties with spatial distributions of trace gases, and, thus, with the details of radiative forcing. Even small changes in heating/cooling rates in GCMs can result in large changes in the simulated meridional circulation patterns in the middle atmospheres.

Three-dimensional simulations are usually very computationally demanding, especially for fast rotating large planets. Highly efficient models are required to simulate the atmospheric flows on them. Validating the simulations is also a difficult issue. The tropospheric flows on the giant planets can be inferred by using visible cloud features as a proxy, very few measurements of the vertical structure of the troposphere and the stratospheric features exist. In order to understand the atmospheric phenomena like Semi-Annual Oscillations (SAO) in Saturn's low-latitude stratospheric temperatures (Orton et al. 2008) and Quasi-Quadrennial Oscillation (QJO) on Jupiter (Leovy et al. 1991, Friedson 1999, Simon-Miller et al. 2007), efficient three-dimensional models are required. The large-scale stratospheric circulation was a subject of debates for a long time. Still, even the direction of the stratospheric meridional transport is not firmly established. Tracings of debris from the comet Shoemaker-Levy 9 that plunged into Jupiter indicates a very slow meridional transport in the stratosphere. The current two-dimensional models produce controversial results regarding this transport, and disagree with respect to circulation patterns under slightly different scenarios. Hence, it is important to simulate and analyze the circulation with a three-dimensional GCM. The main objective of this work is to develop an efficient three-dimensional model covering the stratospheres of the giant gas planets, and apply it to simulations of the large-scale dynamics.

2 Model description

The model under consideration is a finite-difference three-dimensional GCM suitable for simulating atmospheric dynamics of the stratospheres of giant gas planets. It is a Eulerian incompressible grid-point model based on the log-pressure vertical coordinates. The (log)-pressure coordinate system assumes a hydrostatic balance, which allows filtering vertically propagating sound waves, and does not affect larger-scale motions, including gravity, Lamb, and Rossby planetary waves. Log-pressure vertical coordinates have an advantage compared to standard sigma or eta coordinates, when applied to gas planets. The latter coordinate systems are based on surface pressure, and imply a rigid surface. Applying sigma or eta coordinate systems for surfaceless atmospheres, like that of Jupiter and Saturn, requires placing the lower boundary significantly deeper than the region of interest in order to avoid distortions caused by the artificial solid surface, which “comes” with the standard coordinate systems. The log-pressure coordinate systems, on contrary, allows to place the floating grid arbitrarily.

There are many advantages of using the grid-point framework in this model. Most notable reasons are that grid-point models can be faster than spectral models of equivalent resolution, especially when the resolution is high (<https://climatedataguide.ucar.edu/configurations/common-spectral-model-grid-resolutions>). The number of arithmetic operations in spectral model grows faster than that in grid-point models, as the horizontal resolution increases due to the Legendre transforms whose cost increases as a cube of equivalent gridpoints. In addition, incorporation of local process parameterizations are straightforward in grid-point models.

2.1 Outline of the model

The model solves the primitive equations of hydrodynamics under the hydrostatic approximation. Under the hydrostatic equilibrium, the vertical pressure gradient balances the gravity force. These equations are suitable for studying the large scale-dynamics under the presumption that the small scale phenomenas are parameterizable. They describe atmospheric flows with horizontal scales that greatly exceed the vertical ones. The model is based on the log-pressure vertical coordinate defined as

$$z = -H \log(p/p_s), \tag{2.1}$$

where:

- p Pressure
- p_s Reference pressure
- z Height above a fiducial surface (e.g. 1 bar pressure level on a gas giants, which does not have a surface)
- H Atmospheric mean scale height

The primitive equations assume incompressibility (Boussinesq approximation), which leads to zero wind divergence $\nabla \cdot \mathbf{u} = 0$. The horizontal momentum equations (in the flux form), the continuity, and thermodynamic equations in spherical coordinates are as follows (Holton 1975, Andrews et al. 1987)

$$\begin{aligned} \frac{\partial u}{\partial t} + \frac{\partial}{\partial x}(u^2) + \frac{1}{\cos \phi} \frac{\partial}{\partial y}(uv \cos \phi) + \frac{1}{\rho} \frac{\partial}{\partial z}(\rho uw) \\ = v \left(f + \frac{u \tan \phi}{a} \right) - \frac{\partial \Phi}{\partial x} + F_X, \end{aligned} \quad (2.2)$$

$$\begin{aligned} \frac{\partial v}{\partial t} + \frac{\partial}{\partial x}(uv) + \frac{1}{\cos \phi} \frac{\partial}{\partial y}(v^2 \cos \phi) + \frac{1}{\rho} \frac{\partial}{\partial z}(\rho vw) \\ = -u \left(f + \frac{u \tan \phi}{a} \right) - \frac{\partial \Phi}{\partial y} + F_Y, \end{aligned} \quad (2.3)$$

$$\frac{\partial u}{\partial x} + \frac{1}{\cos \phi} \frac{\partial}{\partial y}(v \cos \phi) + \frac{1}{\rho} \frac{\partial}{\partial z}(\rho w) = 0, \quad (2.4)$$

$$\begin{aligned} \frac{\partial T}{\partial t} + \frac{\partial}{\partial x}(Tu) + \frac{1}{\cos \phi} \frac{\partial}{\partial y}(Tv \cos \phi) \\ + \frac{1}{\rho} \frac{\partial}{\partial z}(\rho Tw) = -\frac{\kappa T}{H} w + F_T, \end{aligned} \quad (2.5)$$

$$\partial \Phi / \partial z = RT/H. \quad (2.6)$$

where:

$$\frac{\partial}{\partial x} = \frac{1}{a \cos \phi} \frac{\partial}{\partial \lambda}; \quad \frac{\partial}{\partial y} = \frac{1}{a} \frac{\partial}{\partial \phi},$$

$$\kappa = R/c_p; \quad f = 2\Omega \sin \phi.$$

The symbols used are:

λ	Longitude
ϕ	Latitude
Φ	Planetary potential
T	Temperature
u	Wind component along the longitude λ
v	Wind component along the latitude ϕ
w	Wind component along the log-pressure height z
a	Planetary radius
R	Specific gas constant
c_p	Specific heat capacity at constant pressure
f	Coriolis parameter (see above)
κ	R/c_p , ratio of specific gas constant to specific heat capacity at constant pressure
Ω	Planetary rotational frequency
dx	Distance increment along the longitude λ
dy	Distance increment along the latitude ϕ

We have retained the curvature terms in the equations because of the relatively coarse resolution of the model, which is of the order of the planetary scale. These terms ($(uv \tan \phi)/a$ in Equation 2.2 and $-(u^2 \tan \phi)/a$ in Equation 2.3) are usually neglected when the length scale $L \ll a$. The planetary potential is used instead of pressure in the model. The equation 2.6 is solved diagnostically, and allows to close the set of equations for the dependent variables (u, v, w, T, Φ). The frictional and forcing terms F_X, F_Y , and F_T are described below. Log-pressure coordinates have an advantage when applied to gaseous surfaceless giant planets, because no impermeable surface is implied at the lower boundary.

2.2 Model grids

2.2.1 Horizontal discretization

The staggered horizontal grid classification by Arakawa and Lamb (1977) is shown in Figure 2.1. The horizontal B-grid staggering has some advantages among the five Arakawa grid types. In particular, the B-grid helps to reduce the truncation error, and gives a better representation of wave phase velocities (Wickett et al. 2000).

The implemented gridpoint dynamical core solves the primitive equations using finite differences on the staggered horizontal Arakawa B-grid, as depicted in Figure 2.2. The staggered finite difference calculations are more accurate than non-staggered ones, and the B-grid is a perfect choice for coarser resolution models (Batteen and Han 1981). The Arakawa B-grid has another advantage that it has both components of horizontal velocity located at the same grid point, which helps to better representation of Rossby waves. The grid distance between neighboring point in latitude, Δy , is set constant throughout the globe, and the longitudinal distance between two longitudinal points Δx becomes smaller for latitudes approaching the poles. The model is coded in such a way that the horizontal grid indexing increases from South to North, and from west to east. The global grid distances are calculated as

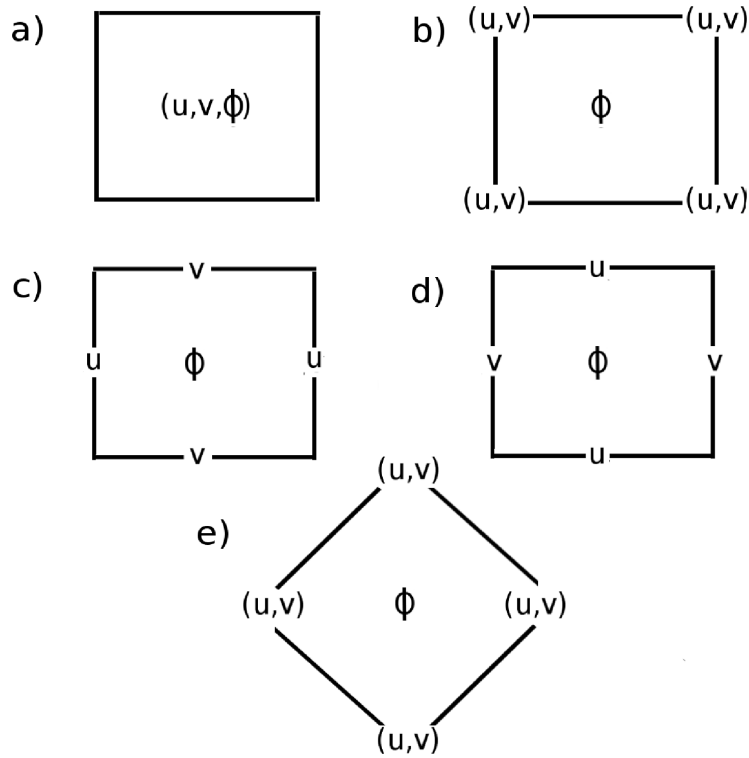


Figure 2.1: The staggered horizontal grids classification by Arakawa and Lamb (1977),
 a) Unstaggered grid A b) Staggered grid B
 c) Staggered grid C d) Staggered grid D
 e) Staggered grid E

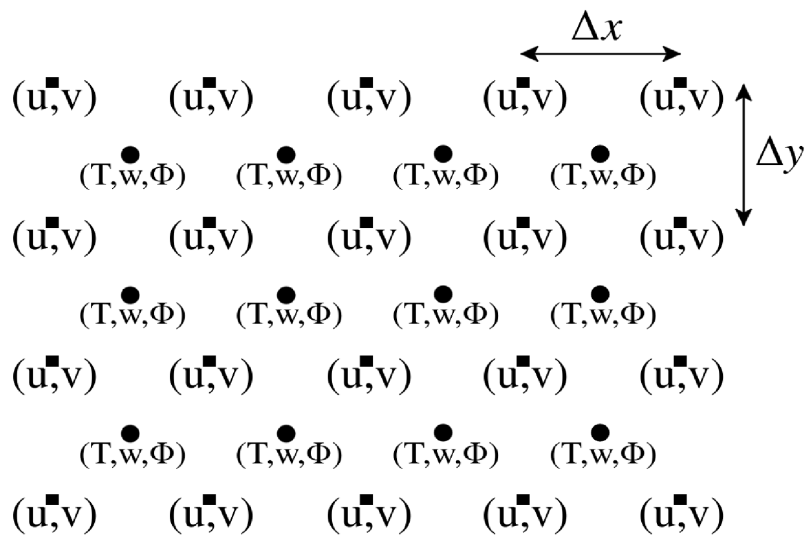


Figure 2.2: The horizontal distribution of model variables $u,v,T,w,$ and Φ in the B-grid configuration

$$\Delta x = a \cos \phi \Delta \lambda, \tag{2.7}$$

$$\Delta y = a \Delta \phi = \frac{a \pi}{N_\phi}, \tag{2.8}$$

where:

- $\Delta \lambda$ Angle between two longitude grid points
- $\Delta \phi$ Angle between two latitude grid points
- N_ϕ Number of grid points in latitude

2.2.2 Vertical discretization

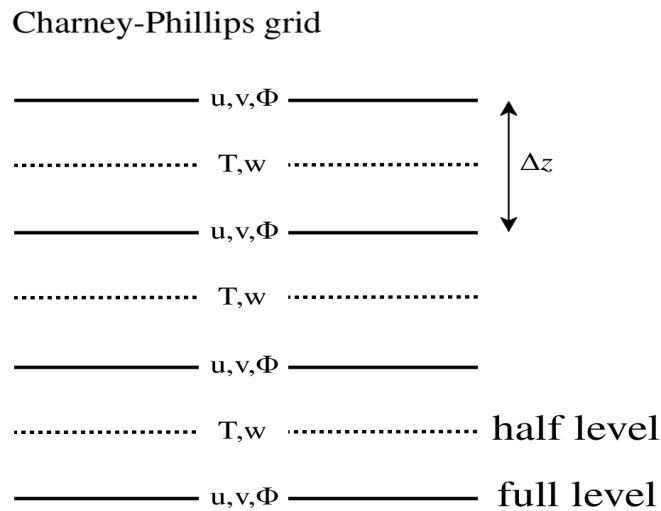


Figure 2.3: Charney-Phillips grid configuration of the model variables in vertical

The vertical discretization used in the model is the Charney-Phillips (Charney and Phillips 1953) grid system, which is shown in Figure 2.3. In this grid system, the temperatures (T) and vertical velocities (w) are prescribed at the same vertical levels (half-levels shown as dashed lines), which lie in between the layers, at which the planetary potential (Φ) and horizontal velocities (u, v) are given (full levels are shown with solid lines). Hence, the temperature and vertical velocity (w) are staggered with respect to the horizontal wind and planetary potential. Other commonly used vertical grid systems are a) unstaggered grid, in which all variables are kept at the same levels, and b) the Lorenz grid, where the vertical velocity is staggered from the temperature. The model dynamical core based on the Charney-Phillips vertical staggering arrangement provides more accurate results for primitive equations compared to the unstaggered or the Lorenz grid systems (Leslie and Purser 1992). The Charney-Phillips scheme grid is more consistent

with the thermal wind balance, and prevents spurious amplification of short waves generated by baroclinic instability (Arakawa and Moorthi 1988). This vertical grid system conserves quasigeostrophic potential vorticity during advection. Another big advantage of the Charney-Phillips grid system is that it does not produce parasite computational modes. The computational modes appear as oscillations in vertical temperature profiles, which do not exist in continuous “physical world”, and arise only due to finite-difference time-stepping algorithms. The three-dimensional grid system and the grid box is illustrated in Figure 2.4.

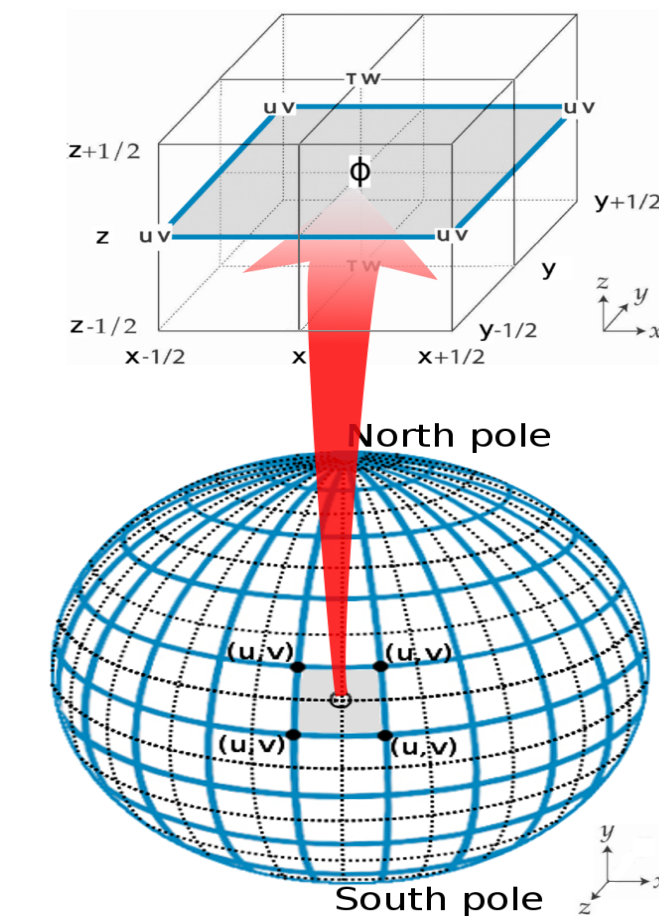


Figure 2.4: Global view of the grid system and the grid box with indexing, employed in the model.

2.3 Time stepping scheme and time filter

Let us assume a continuous function F in the neighborhood of x_i . Using the Taylor expansion, we have for any $\Delta x_i > 0$:

$$F(x_i + \Delta x_i) = F(x_i) + \frac{1}{1!} \left. \frac{dF}{dx} \right|_{x_i} \Delta x_i + \frac{1}{2!} \left. \frac{d^2 F}{dx^2} \right|_{x_i} \Delta x_i^2 + \frac{1}{3!} \left. \frac{d^3 F}{dx^3} \right|_{x_i} \Delta x_i^3 + \dots + \frac{1}{n!} \left. \frac{d^n F}{dx^n} \right|_{x_i} \Delta x_i^n + \dots \quad (2.9)$$

$$F(x_i - \Delta x_i) = F(x_i) - \frac{1}{1!} \left. \frac{dF}{dx} \right|_{x_i} \Delta x_i + \frac{1}{2!} \left. \frac{d^2 F}{dx^2} \right|_{x_i} \Delta x_i^2 - \frac{1}{3!} \left. \frac{d^3 F}{dx^3} \right|_{x_i} \Delta x_i^3 + \dots + (-1)^n \frac{1}{n!} \left. \frac{d^n F}{dx^n} \right|_{x_i} \Delta x_i^n + \dots \quad (2.10)$$

Subtracting 2.10 from 2.9 and solving for the first derivative $\left. \frac{dF}{dx} \right|_{x_i}$, we obtain

$$\left. \frac{dF}{dx} \right|_{x_i} = \frac{(x_i + \Delta x_i) - (x_i - \Delta x_i)}{2\Delta x_i} - \underbrace{\frac{1}{3!} \left. \frac{d^3 F}{dx^3} \right|_{x_i} \Delta x_i^2 - \dots - \frac{1}{n!} \left. \frac{d^n F}{dx^n} \right|_{x_i} \Delta x_i^{n-1} - \dots}_{\text{neglected part}} \quad (2.11)$$

If we limit the accuracy of the above equations by the first term in the right-hand side, we obtain the centered difference approximation for the derivative

$$\left. \frac{dF}{dx} \right|_{x_i} = \frac{(x_i + \Delta x_i) - (x_i - \Delta x_i)}{2\Delta x_i}. \quad (2.12)$$

The error involved in this elimination of higher-order terms is referred to as truncation error. The approximation is then accurate to the second order, because the highest-order term in the neglected part is Δx_i^2 . The truncation error can be reduced by using smaller Δx .

Time integration is performed using the most commonly used centered difference "leapfrog" scheme, which is an explicit time stepping scheme, and is more accurate than the first-order Euler method, as is seen from (2.9). The time advancement of a variable u with the leapfrog time stepping scheme is then given by

$$u_{n+1} = u_{n-1} + 2 \Delta t \left. \frac{dF}{dt} \right|_{t_i}. \quad (2.13)$$

Combination of second-order in time and space approximations can be illustrated with the linear advection equation

$$\frac{u_{m,n+1} - u_{m,n-1}}{2 \Delta t} = -c \left(\frac{u_{m+1,n} - u_{m-1,n}}{2 \Delta x} \right) \quad (2.14)$$

where c is the velocity of an air parcel.

The stability in the time-stepping scheme is controlled by the Courant-Friedrich-Levy (CFL) criterion (Courant et al. 1967 (1928)), which limits the time step duration Δt . The CFL criterion can be represented as

$$\frac{c \Delta t}{\Delta x} \leq 1, \quad (2.15)$$

which means that the grid distance in the model should be greater than the distance covered by the fastest wave in the model carrying information.

The model implements the second-order accurate $O(\Delta x^2)$ centered differencing in space, and the second-order accurate $O(\Delta t^2)$ centered time stepping. The main disadvantage of using a leapfrog time-stepping scheme is that it produces artificial computational modes, in addition to the real physical mode. The odd- and even time steps are decoupled, and the solutions at them tend to diverge from each other: the values at the $(n + 1)^{th}$ time step are calculated from the $(n - 1)^{th}$ step using centered differences, and do not include the n^{th} time moment. This decoupling cannot be removed by increasing the accuracy of the scheme. This time splitting (computational modes) appear as spurious oscillations. One method to handle this artificial oscillations is to use a two-level time stepping scheme periodically instead of three-level leapfrog time-stepping, which resets periodically the computational mode amplitude to zero. Another common method is to apply a time filter which damps the spurious oscillations. The well known Robert-Asselin (Asselin 1972) time filter is the most widely used one. It requires three time levels, and provides a second order diffusion in time.

Let us consider a quantity x at previous and current time-steps $x_{(n-1)}$, x_n respectively. The model then calculates the tendency of the quantity x_{tend} and performs leapfrog time stepping to calculate the future value $x_{(n+1)}$.

$$x_{(n+1)} = x_{(n-1)} + 2 \Delta t x_{tend} \quad (2.16)$$

The spurious oscillations generated by the computational mode is then removed by applying a filter. The Robert-Asselin filter can efficiently suppress the computational mode, but reduces the numerical accuracy, because it weakly but continuously affects the physical mode also. Hence, the model employs the Robert-Asselin time filter modified by Williams (2009, 2011) (Robert-Asselin-Williams (RAW) filter). The leapfrog time stepping scheme with Robert-Asselin filter is of first order accuracy for amplitude errors, but the modified scheme gives third order accuracy for amplitude errors.

The Robert-Asselin filter can be represented as

$$\bar{x}_n = x_n + \alpha_{Asselin}(\bar{x}_{(n-1)} - 2x_n + x_{(n+1)}) \quad (2.17)$$

Where a bar indicates filtered fields and $\alpha_{Asselin}$ is the Robert- Asselin filter coefficient. The strength of the filter is determined by the coefficient, which usually varies from .01 to 0.2. Schlesinger et al. (1983) suggested that values from 0.25 to 0.3 can be used for diffusive and advective simulations. After sensitivity experiments, we chose the value 0.15 for the coefficient $\alpha_{Asselin}$. From the equation 2.17, we can see that the Robert - Asselin filter is displacing x_n by a factor $\alpha_{Asselin}(\bar{x}_{(n-1)} - 2x_n + x_{(n+1)})$. But the modified RAW filter displaces x_n by $\alpha(\alpha_{Asselin}(\bar{x}_{(n-1)} - 2x_n + x_{(n+1)}))$ and $x_{(n+1)}$ by $(\alpha - 1)(\alpha_{Asselin}(\bar{x}_{(n-1)} - 2x_n + x_{(n+1)}))$, where $0 \leq \alpha \leq 1$ (see Figure 2.5).

$$\bar{x}_n = x_n + \alpha(\alpha_{Asselin}(\bar{x}_{(n-1)} - 2x_n + x_{(n+1)})) \quad (2.18)$$

$$x_{n+1}^- = x_{n+1} + (\alpha - 1)(\alpha_{Asselin}(\bar{x}_{(n-1)} - 2x_n + x_{(n+1)})) \quad (2.19)$$

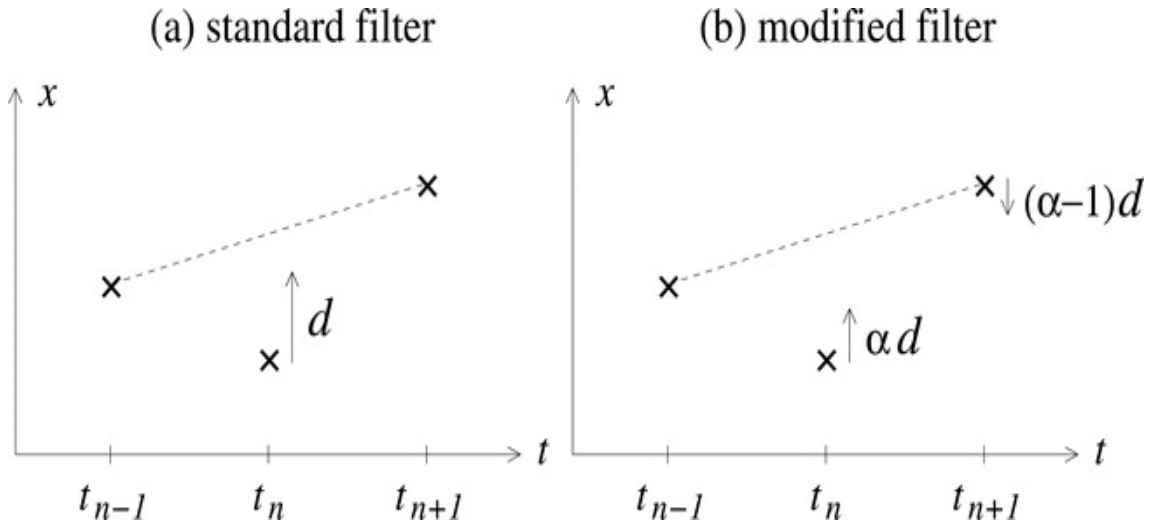


Figure 2.5: Graphical comparison of the operation of (a) the standard Robert-Asselin filter and (b) the modified family of filters. Points at three consecutive time levels are shown (marked with times signs) and a straight line is drawn between the two outer points (dashed). The standard filter moves the inner point through a displacement d , defined by (1). The modified filter moves the inner and right outer points through displacements αd and $(\alpha - 1)d$, respectively, where $0 \leq \alpha \leq 1$. For the configuration of three points shown, $d > 0$. (adapted from (Williams 2009))

The RAW filter allows to use large time steps, which increases the efficiency of the model. The value of $\alpha = 1$ in RAW filter will give the standard Robert-Asselin filter. The coefficient $\alpha=0.53$ is used in the model, which is stable and provides third order amplitude accuracy for the filtered values.

2.4 Boundary conditions

We assume vanishing the mass flux through the top of the model, which is the commonly accepted approximation in general circulation models. Thus, the model upper boundary condition is

$$\frac{dw}{dz} = 0. \quad (2.20)$$

At the lower boundary, the assumption is that the horizontal wind velocity does not vary much with height, i.e.

$$\frac{du}{dz} = \frac{dv}{dz} = 0. \quad (2.21)$$

This lower boundary condition is a good one for gas planets, because there is no surface to provide frictional forces for kinetic energy losses. This frictional kinetic energy loss is a major mechanism to slow down the surface winds. The dynamical biases in the upper troposphere are included in the model by nudging the observed zonal winds at the lower boundary (five levels) of the model.

$$F_X = \frac{\overline{U}_{obs} - U}{\tau_u}, \quad (2.22)$$

where τ_u is the characteristic relaxation time. A similar technique was applied in the GCM simulations of the Saturn's atmosphere by Friedson and Moses (2012). Large τ_u allows for a development of longitudinal disturbances (eddies) in the lower atmosphere, which requires finer spatial and temporal resolution, and significantly longer spin-up times. Therefore, we introduced 5 additional model levels below the domain of interest, in which nudging smoothly varied from $\tau_u = 1/3$ of a Saturn day at the deepest layer to about 0.02 Saturn years at the lower boundary. Such distribution was chosen in a series of numerical experiments, and the latter value is the same as was used by Friedson and Moses (2012)

2.5 Dissipation terms

2.5.1 Subgrid-scale horizontal diffusion

To prevent a build-up of energy at the smallest resolved scales and the instabilities that may result, a horizontal bilinear diffusion (Marchuk et al. 1987) is implemented in the model. Inclusion of dissipation is the basic requirement for all GCMs. In order to suppress nonlinear instabilities, models need to account for subgrid-scale processes in a parameterized form. The model horizontal diffusion parameterization is given by

$$F_u = \frac{K_H}{a^2 \cos^2 \phi} \left(\frac{\partial^2 u}{\partial^2 \lambda} + \frac{\partial}{\partial \phi} \cos^3 \phi \frac{\partial}{\partial \phi} \left(\frac{u}{\cos \phi} \right) - 2 \sin \phi \frac{\partial v}{\partial \lambda} \right), \quad (2.23)$$

$$F_v = \frac{K_H}{a^2 \cos^2 \phi} \left(\frac{\partial^2 v}{\partial^2 \lambda} + \frac{\partial}{\partial \phi} \cos^3 \phi \frac{\partial}{\partial \phi} \left(\frac{v}{\cos \phi} \right) - 2 \sin \phi \frac{\partial u}{\partial \lambda} \right), \quad (2.24)$$

$$F_T = \frac{K_H}{a^2 \cos^2 \phi} \left(\frac{\partial^2 T}{\partial^2 \lambda} + \cos \phi \frac{\partial}{\partial \phi} \left(\cos \phi \frac{\partial T}{\partial \phi} \right) \right). \quad (2.25)$$

These diffusion terms in the simplified form can be converted to the second Fick's law. According to it, the change in magnitude of a quantity U with time can be written as

$$\frac{\partial U}{\partial t} = D \frac{\partial^2 U}{\partial x^2} \quad (2.26)$$

The scale analysis of this equation by using the model values gives the high Reynolds numbers, in which the fluid behavior is turbulent:

$$D \frac{\partial^2 U}{\partial x^2} \approx \frac{D \times U}{L \times L} \approx \frac{10^7 \times 10^2}{10^6 \times 10^6}. \quad (2.27)$$

$K_H = 7 \times 10^6 \exp(0.85 \times 10^{-5} z) \text{ m}^2 \text{ s}^{-1}$ was used in most simulations. This coefficient has been chosen in a series of sensitivity tests as the most "gentle", but still providing numerical stability. The diffusion coefficient is vertically increasing. This increase is required to keep the stability of the model, because the diffusion term in simplified form is $\approx \mu \nabla^2 u$ where, μ is the dynamic viscosity of the fluid in $(\text{kg m}^{-1} \text{ s}^{-1})$. But $\mu = \nu / \rho$, where ν is the kinematic viscosity (in $\text{m}^2 \text{ s}^{-1}$). Therefore, the exponentially growing with height diffusion coefficient reflects the density scaling for the turbulent kinematic viscosity.

2.5.2 Vertical diffusion

In addition to the background horizontal diffusion, the model employs a standard local diffusion parameterization for the free atmosphere based on the Richardson number (Hartogh et al. 2005, Sect. 6.1). The effects of shear instabilities, which cause turbulent kinetic energy losses are parameterized by adding vertical diffusion. The model has a vertical dissipation in the form of the Shapiro (1970) filter to prevent build up of energy (both kinetic and potential) at shortest resolved vertical scales, and associated instabilities.

2.5.3 Molecular diffusion and thermal conduction

Since our GCM extends well into the upper atmosphere, diffusive effects of the air with low density should be taken into account. Therefore, the vertical molecular diffusion and thermal conduction are included in the terms F_X , F_Y , and F_T . We adopted the thermal conduction coefficient for a hydrogen atmosphere from (Matcheva and Strobel 1999) $k = AT^{0.751}$, where $A = 2.52 \cdot 10^{-3} \text{ J m}^{-1} \text{ s}^{-1} \text{ K}^{-0.751}$. The kinematic molecular viscosity ν_{mol} is related to k via $k = 0.25[9c_p - 5(c_p - R)]\nu_{mol}$. Thermal conduction becomes important at pressures less than $\approx 1 \mu \text{ bar}$. Besides the molecular viscosity, no other friction forces are taken into account in the upper atmosphere. Thus, we do not introduce an artificial Rayleigh friction near the top of the model that often is utilized in GCMs for reducing the wind speed and keeping the model stability. On the other hand, we do not account for possible damping effects like gravity wave drag or ion friction, which are difficult to constrain due to the lack of observational data.

2.6 Computational aspects of the model - Polar values

The model requires special treatment of grids at the poles. Poles are singular points, but the model has a number of longitudinal grid points at the poles. These longitudinal points at the poles virtually represent a single point. We have taken average of the nearby latitude points and calculated the polar value from that. The assumption is that the resulting value of the averaging operation must represent the actual singular polar value, and no time stepping is required for them.

2.6.1 Polar filters

The longitudinal grid distance becomes smaller as we approach the poles, and extremely small time steps are required to satisfy the CFL condition in the near-pole regions. Usage of very small time steps makes the simulations computationally expensive, and, thus, reduces the efficiency of the model. Increasing time steps produces computational instabilities at the poles, and application of near-pole filter becomes inevitable. Inclusion of near-pole filters is a standard procedure in grid point GCMs (Kar et al. 1994). A near-pole Fourier filter is applied in our GCM to the prognostic fields at latitudes higher than 83.75° . This low pass filter truncates zonal (along the west-east direction) harmonics higher than 2 to maintain the numerical stability of the model. This high-latitude zonal filter eliminates high wave number noises and fast-moving gravity waves near the poles.

2.7 Parameterization of the thermal forcing

Deep circulation models assume internal heat sources as the basic forcing mechanism. Absorption of solar radiation and radiative redistribution of the thermal energy is the major energy source that drives the circulation. Hence, GCMs require parameterizations to calculate heating and cooling rates due to radiative processes in the atmosphere. In order to compute them, accurate information on distributions of the radiatively active minor atmospheric gas components is required. To date, there are measurements of vertical and meridional distributions of methane, C_2H_2 , C_2H_6 and other minor species on Jupiter and Saturn (Fouchet et al. 2000, Greathouse et al. 2005). Radiative forcing in atmospheres of gas giants is relatively weak compared to Earth and the terrestrial planets, and the strength of meridional circulations is weak as well. The simulated circulation is very sensitive to small errors and variations of hydrocarbons and aerosols. Thus, development of accurate radiative schemes suitable for implementation in GCMs for gas giant planets is a separate and important task. It is beyond the scope of this work. Instead, we employed a simple parameterization of radiative heating/cooling rates in the form of the Newtonian cooling (Wu et al. 2000, Williams 2003, Simon-Miller et al. 2006). Newtonian cooling linearly relaxes the model temperature to the prescribed equilibrium distribution T_{eq} with a characteristic nudging coefficient, or the so-called radiative relaxation time τ_{rad} time:

$$F_T = \frac{T_{eq} - T}{\tau_{rad}} \quad (2.28)$$

The coding was done in such a way that a more advanced radiation scheme can substitute the Newtonian cooling parameterization at a later stage.

2.8 Convective adjustment scheme

The model includes a convective adjustment scheme to prevent vertical temperature gradients from overshooting the convectively stable adiabatic lapse rate. This may happen when amplitudes of waves and/or eddies become large. Most of convective instability events occur in the troposphere, where the vertical gradient of the mean temperature is close to the adiabatic one, i.e. when $d\theta/dz \approx 0$, θ being potential temperature.

$$\theta = T \left(\frac{p_s}{p} \right)^k = T \exp(kz/H), \quad (2.29)$$

where $k = R/c_p$, and c_p is the specific heat capacity at constant pressure. The primitive equations assume that the atmosphere is in hydrostatic equilibrium, so the vertical pressure gradient balances the gravity, which can be represented as

$$g = -\frac{1}{\rho} \frac{dp}{dz} = \frac{RT}{H}. \quad (2.30)$$

In certain cases, convective instability can be generated in the stratosphere. Therefore, we apply the dry convective adjustment scheme at all vertical levels, which has been used in a Martian GCM (Hartogh et al. 2005, Saito 2006). The implemented convective scheme

adjusts the vertical temperature gradient to a dry adiabatic one when the vertical temperature gradient becomes superadiabatic, i.e., it maintains the potential temperature gradient positive, $d\theta/dz \geq 0$. The atmospheric stability to convection depends on the steepness of the lapse rate, Γ (Manabe and Strickler 1964, Ramanathan and Coakley 1978). The dry adiabatic lapse rate can be obtained by differentiating the equation 2.29 and assuming $d\theta/dz=0$.

$$\Gamma_d = -\frac{dT}{dz} = -\frac{kT}{p} \frac{dp}{dz} = -\frac{g}{c_p} = -\frac{kT}{H} \quad (2.31)$$

Where $g = RT/H$ is the gravitational constant and H is the scale height. The atmosphere becomes unstable when the actual lapse rate, Γ is steeper than the dry adiabatic lapse rate, Γ_d (Barnet et al. 1992) and becomes stable when $\Gamma < \Gamma_d$. The static stability parameter, φ_s depends on the values of the actual lapse rate and dry adiabatic lapse rate. By using equation 2.31, the static stability parameter can be written as,

$$\varphi_s = (\Gamma - \Gamma_d)dz = -dT + \frac{kT}{p} dp, \quad (2.32)$$

When the instability occurs, the bottom layer z_0 and the upper layer z_1 is adjusted according to the following equations

$$T_{z_0} = \frac{\rho_{z_0} T_{z_0} + \rho_{z_1} (T_{z_1} + \Gamma_d)}{\rho_{z_0} \rho_{z_1}} \quad (2.33)$$

$$T_{z_1} = T_{z_0} - \Gamma_d \quad (2.34)$$

2.9 Other computational aspects

The model has both the Message Passing Interface (MPI) and the OpenMP parallelizations, which enable the model to run efficiently on both shared memory machines and clusters. The parallelization schemes are switchable. We have investigated the efficiency of these implementations on Non-Uniform Memory Architecture (NUMA) machines and found that the OpenMP Implementation is giving better performance than our MPI implementation. The model is also vectorized and optimized to achieve maximum performance on different architecture machines, including vector processors (e.g. NEC SX-9 machines).

2.10 Simulations

The model is run in two resolution modes “lower resolution” mode which has 90 grid points in the latitude and 120 point in the longitude, and the “higher resolution” mode which has 180 grid points in the latitude and 240 point in the longitude. The number of vertical levels are kept constant in both cases as 41 levels. To understand the circulation patterns and dynamics of the gas giants, simulations with different planetary parameters

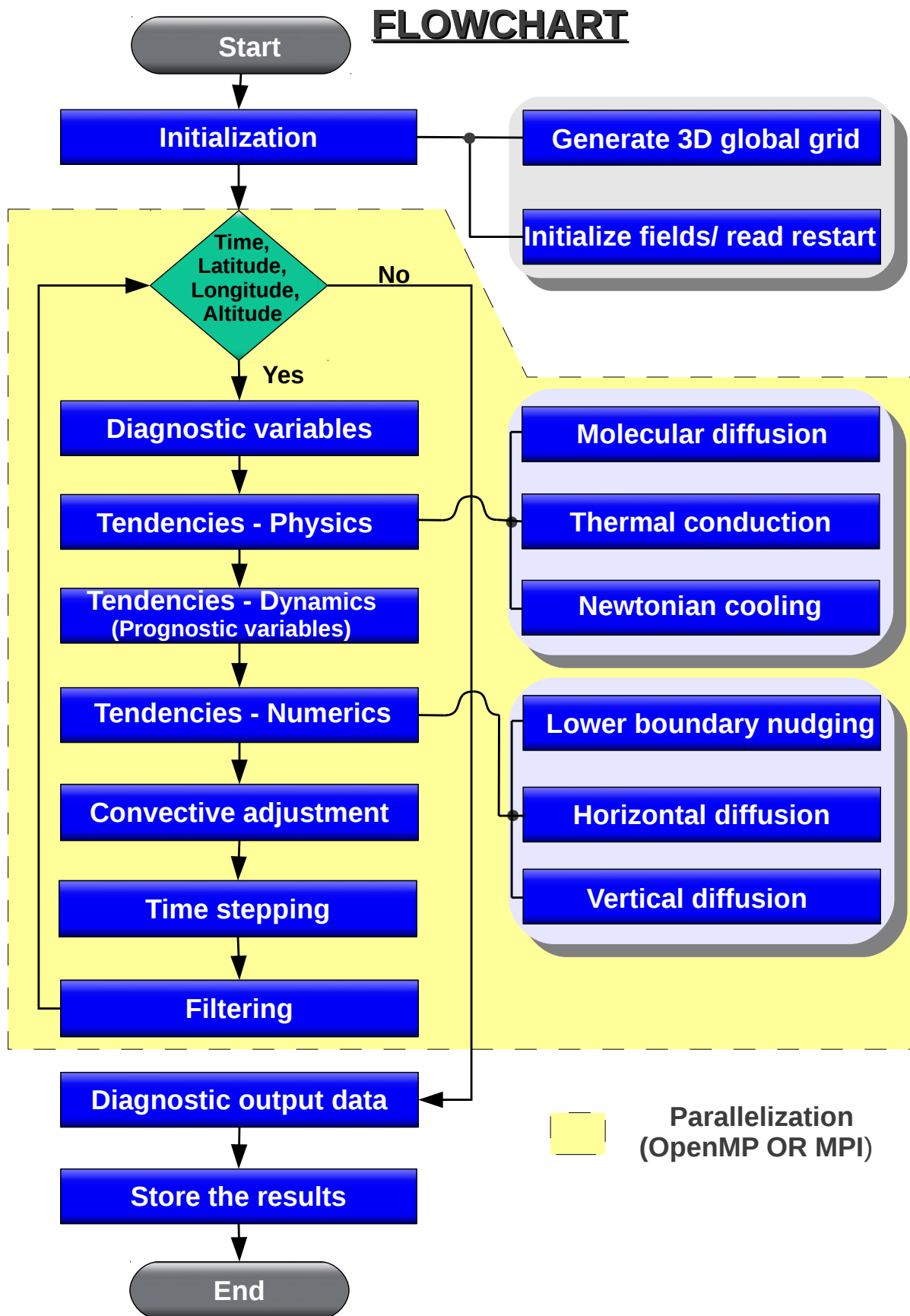


Figure 2.6: A flowchart describing the processes involved in the model

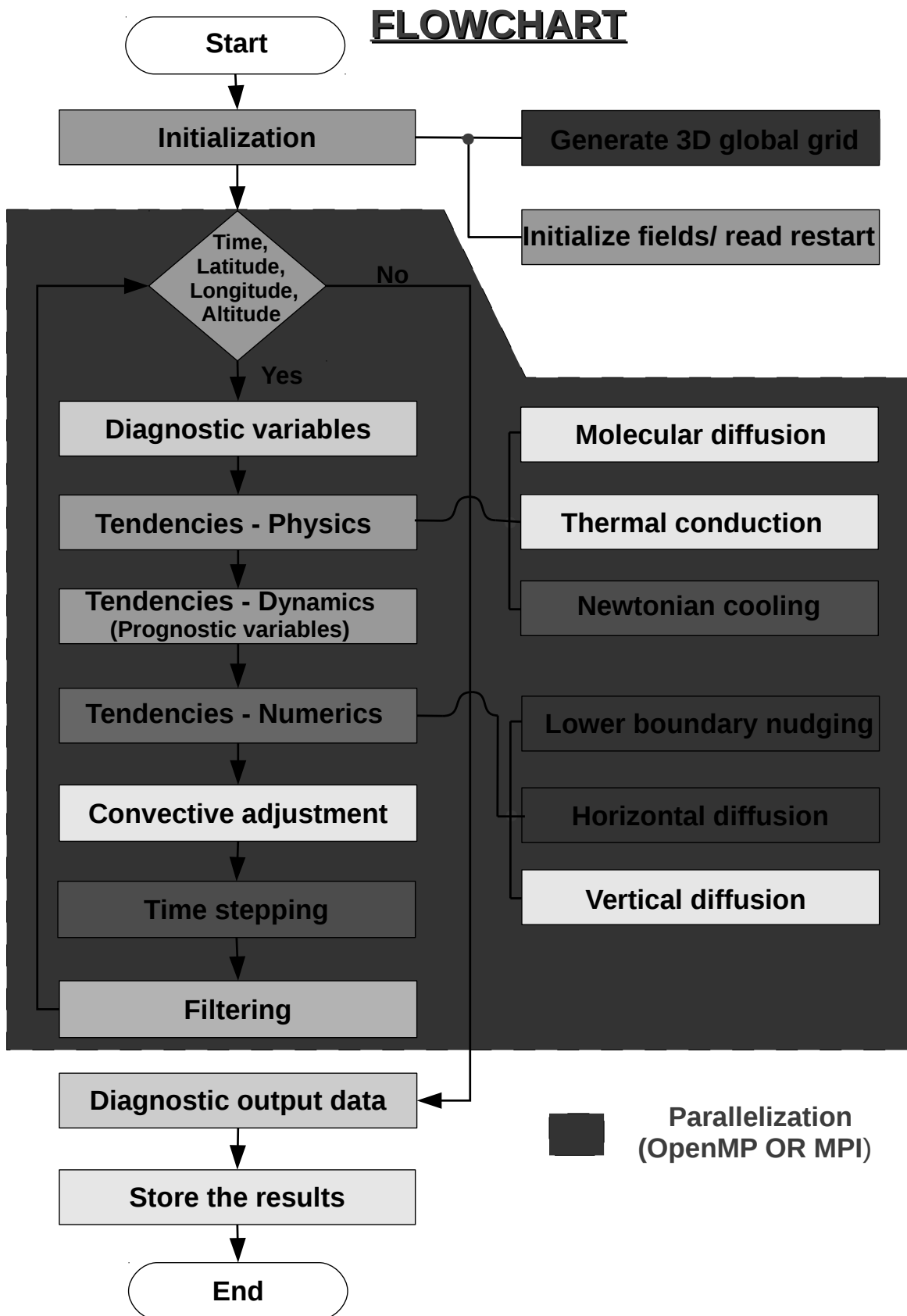


Figure 2.7: Same as Figure 2.6, but illustrates the author's contribution: a darker color indicates author developed and a lighter color indicates the author modified or implemented parts.

are required. To achieve this goal, simulations are done with planetary parameters of Jupiter and Saturn. The experiments are characterized in the following three sections, and the model is applied to simulate and study the atmospheric dynamics of “Warm Jupiters”, Jupiter and Saturn.

3 Three-dimensional modeling of Saturn's middle atmosphere

3.1 Observational constraints on dynamics

Saturn, a low-density planet at a distance of ~ 1.4 billion km from the Sun takes ~ 29.4 years to orbit it. Even though Saturn's massive rings often limit the full disc observations (e.g. Hartogh et al. 2011), many basic features of the Saturnian atmosphere are known (Flasar et al. 2004, Del Genio et al. 2009).

The atmosphere of Saturn has been well studied in the past (Atreya and Wong 2005, West et al. 2009, Del Genio et al. 2009, Flasar et al. 2005). It is known that the internal thermal emission flux on Saturn ($\sim 2.01 \text{ W m}^{-2}$) is smaller than that on Jupiter (the internal energy flux is $\approx 5 \text{ W m}^{-2}$) (Hanel et al. 1983, Ingersoll 1990). Despite the weak solar irradiation, the atmosphere of Saturn apparently demonstrates seasonal variations due to the large axial tilt, 26.73° (Sinclair et al. 2013). The temperature structure of the Saturnian middle atmosphere as well as seasonal changes have been inferred from satellites and the Hubble Space Telescope (HST) observations (Flasar et al. 2004, Fletcher et al. 2007, Sinclair et al. 2013, Fletcher et al. 2010, Fletcher et al. 2010, Guerlet et al. 2011, Fouchet et al. 2008). Long term observations of Saturn by the Cassini spacecraft allowed for the first time to study the seasonal effects on Saturn in detail. The Saturn's vertical and latitudinal cloud structure have been analyzed from long-term HST observations (1991-2004) by Karkoschka and Tomasko (2005). They revealed a substantial variability of the tropospheric and stratospheric aerosol optical depth. In addition, considerable vertical shears in the cloud level jet were observed (García-Melendo et al. 2009). There are many specific large-scale atmospheric dynamical phenomena on Saturn like oval vortices, which resemble the Jupiter's Great Red Spot, and white ovals (Smith et al. 1982). Their origin and dynamical importance still remain unknown.

Observations established that the Saturn's middle atmospheric minor components include methane (CH_4), ethane (C_2H_6), acetylene (C_2H_2), ammonia (NH_3), propane (C_3H_8), hydrogen sulphide (H_2S), methylacetylene ($\text{CH}_3\text{C}_2\text{H}$), diacetylene (C_4H_2), and others in smaller quantities (Atreya et al. 1999, Fletcher et al. 2011, Flasar et al. 2005, Guerlet et al. 2010, Fletcher et al. 2012, Cavalié et al. 2009, 2010, Hartogh et al. 2009). The knowledge of global distributions of such tracers can reveal the general circulation in the atmosphere. The recent studies using Cassini/CIRS and NASA's Infrared Telescope Facility (IRTF) ground-based observations allowed to derive the latitudinal abundance distributions of C_2H_2 and C_2H_6 (Hesman et al. 2009, Greathouse et al. 2005). The vertical and meridional profiles of ethane, acetylene and propane in the Saturn stratosphere

from CIRS/Cassini limb observations were derived by Guerlet et al. (2009). Guerlet et al. (2010) also obtained the meridional distribution and variations of C_4H_2 and CH_3C_2H in the Saturnian stratosphere from CIRS/Cassini limb and nadir measurements. Although much is known about the atmospheric composition, uncertainties in the latitudinal-height distributions of minor components limit the use of radiative heating and cooling parameterizations in GCMs. In addition to the minor gas species, a meridional asymmetry of Saturnian aerosols (Stam et al. 2001, Pérez-Hoyos et al. 2005) have also been found. A recent study of the cloud structure and haze distribution inferred from Cassini-ISS (Roman et al. 2013) provides a good view on the lower atmospheric composition and transport.

One- and two-dimensional models have been used to study the atmospheric composition and latitudinal distributions of minor components. They provided an important insights to the chemistry and transport of these species. For instance, the atmospheric photochemistry on Saturn is described in detail by Moses et al. (2000). Another study by Moses and Greathouse (2005) predicted the latitudinal and seasonal variations of the minor species in the stratosphere, which were compared with the IRTF/TEXES (Texas Echelon Cross Echelle Spectrograph) infrared observations.

The vertical temperature profiles on giant planets can be found in many earlier studies (e.g. Gierasch and Conrath 1993, Ollivier et al. 2000). Although there are no *in situ* measurements on Saturn, its temperature structure was revealed by remote sensing from space-born and ground-based instruments (Conrath and Pirraglia 1983, Hanel et al. 1983, Conrath et al. 1989, Flasar et al. 2005, Fletcher et al. 2007). They found that the Saturn's tropopause is at around 65–90 mb. Fletcher et al. (2007) identified the latitudinal temperature difference of 25–30 K, and found an unexpected small knee in the temperature profile around 80–250 mb, which indicates a change in lapse rate due to an unknown mechanism.

The convectively dominated interior of Saturn and radiatively dominated stratosphere have a radiative-convective boundary at ~ 550 mb (Bézard et al. 1984). The radiative forcing of the atmosphere includes heating due to the absorption of solar radiation, and heating and cooling due to re-radiation (mainly in IR) by atmospheric constituents. An accurate treatment of these processes in GCMs requires a detailed knowledge of absorbers and trace gas distributions. Because of the existing uncertainties, simulations with the Newtonian cooling that nudges the model temperature to the observed mean temperature profile is a suitable method to study the atmospheric dynamics of Saturn at this stage. In the simulations described below, the radiative forcing is parameterized by the Newtonian relaxation to the prescribed equilibrium temperature profile, T_{eq} (see Figure 3.1).

The key parameter in such approach is the radiative relaxation time, τ_{rad} . It represents the e-folding time required for a perturbed temperature to decay to the equilibrium T_{eq} . A horizontally uniform T_{eq} was obtained by averaging Cassini/CIRS measurements (Fouchet et al. 2008, Fletcher et al. 2010). The radiative time τ_{rad} can be found from

$$\left. \frac{\delta Q(T)}{\delta T} \right|_{T=T_{eq}} = \frac{1}{\tau_{rad}}, \quad (3.1)$$

where $Q(T)$ is the heating/cooling rate at a given temperature. The characteristic relaxation time for the Saturn's stratosphere was estimated from radiative calculations by Conrath et al. (1990), and was found to be of the order of 10^8 s. This is much longer than the characteristic dynamical timescale $\tau_{dyn} = L/U$, where L and U are the scales of horizontal length and wind velocity, correspondingly, but shorter than the orbital time of

Saturn.

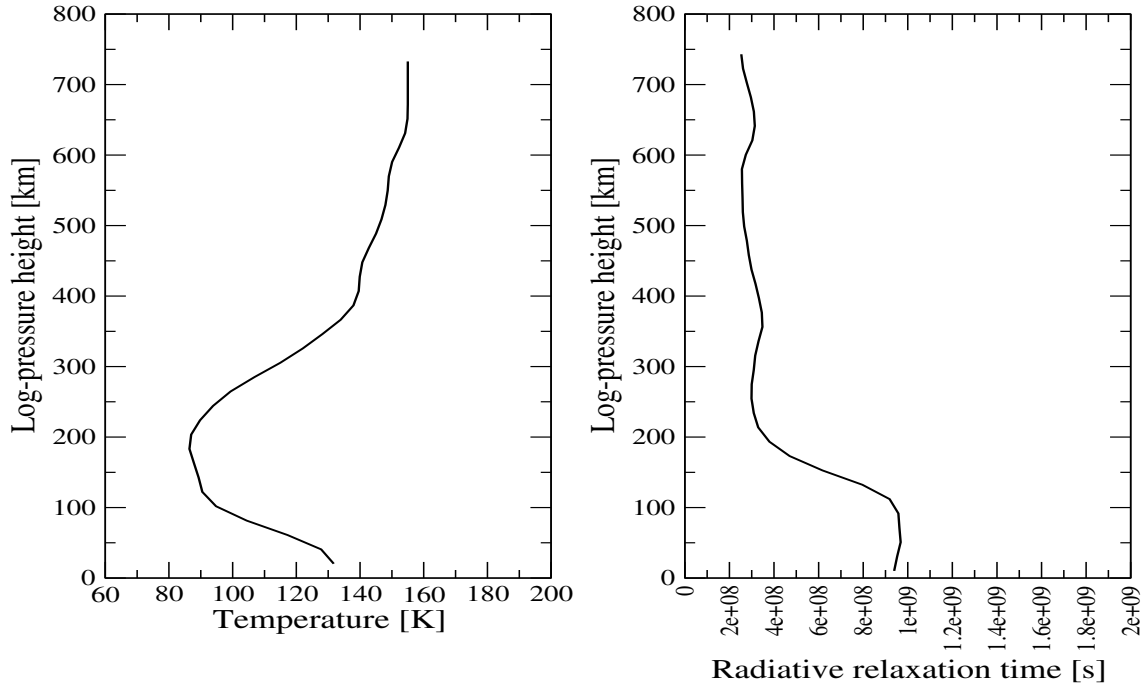


Figure 3.1: Vertical profiles of the equilibrium temperature, T_{eq} , obtained by averaging the Cassini/CIRS measurements (Fouchet et al. 2008, Fletcher et al. 2010) (left), and the radiative relaxation time, τ_{rad} , (Conrath et al. 1990) used in the model.

An overview of observed zonal wind speeds in the atmosphere of Saturn can be found in (Del Genio and Barbara 2012) and Choi et al. (2009). Despite the weaker than on Jupiter solar forcing, the Saturnian atmosphere has stronger winds. The Voyager spacecraft data show that they can reach up to $\approx 500 \text{ m s}^{-1}$ (1800 km hr^{-1}) (Ingersoll 1990). This is larger than on Jupiter, but smaller than on Neptune. Saturn's wind speeds have been described in detail by Sánchez-Lavega et al. (2003). The recent study by Li et al. (2011) found that the Saturnian tropospheric wind velocities increased by $\approx 20 \text{ m s}^{-1}$ between 2005 and 2008, and decreased by 200 m s^{-1} in the equatorial region from 1996 to 2002. The jet of $\sim 600 \text{ m s}^{-1}$ (Liming et al. 2008), and strong vertical shears in the eastward jets at cloud level (García-Melendo et al. 2009) have been reported. The analysis of (Gierasch 2004) suggests that the stability of the jets on Jupiter and Saturn decrease with depth, and that wind speeds can vary with time. Such long-term variability of the Saturn's zonal winds was found from the Cassini ISS images in 2004–2009 by García-Melendo et al. (2009). The measured zonal wind speed adapted from (Choi et al. 2009), which was used at the lower boundary in our simulations, is shown in Figure 3.2.

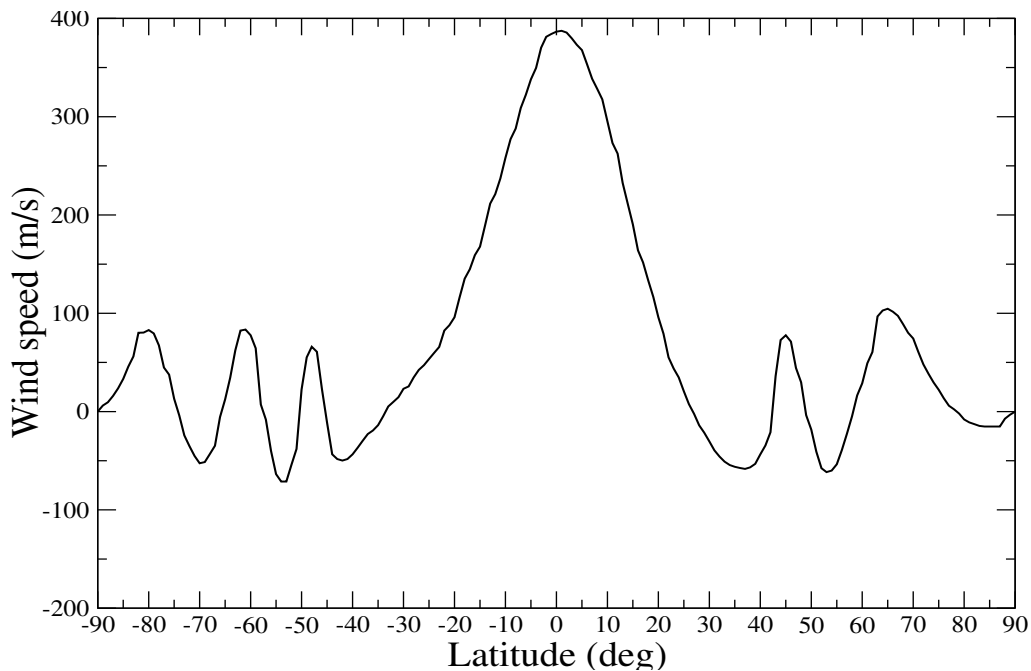


Figure 3.2: Zonal wind applied at the lower boundary (adapted from (Choi et al. 2009)).

Observations show the presence of large scale equatorial oscillations in the atmosphere of Saturn. In particular, they include cold and warm temperature anomalies (Fletcher et al. 2010), and variations of wind speed. They were first attributed to the difference in the measurement altitudes. However, a combined study of cloud tracking and thermal winds derived from atmospheric temperatures by Li et al. (2011) shows that the wind speeds increased from 2004 to 2008 at the particular altitude in the stratosphere corresponding to 60 mb. Interestingly the stratospheric wind at 1 mb has increased by 60 m s^{-1} from 2005 to 2008. These findings suggests that there is strong dynamical activity in the stratosphere. The studies of the temporal variations of the Saturn's equatorial wind in the stratosphere and troposphere suggest that the forcing mechanisms in both regions are apparently different.

The middle atmosphere of Saturn shows also considerable temperature variations. Observations indicate that Saturn's and Jupiter's atmospheres are meteorologically very active. In particular, moist convection exists in the middle atmosphere (Li et al. 2006a, Weidenschilling and Lewis 1973, Sánchez-Lavega et al. 1998, Hueso and Sánchez-Lavega 2004). Saturn's stratospheric equatorial temperature maps show vertically alternating warm and cold patterns (Fouchet et al. 2008, Li et al. 2011). The temporal evolution of the equatorial fields in the stratosphere between 2005 and 2010 (Guerlet et al. 2011) and the computed thermal winds provide further evidence for the variations. In particular, semi-annual oscillations (SAO) (with the period of 14.8 ± 1.2 terrestrial years) have been found by Orton et al. (2008) and Fouchet et al. (2008). Guerlet et al. (2011) studied the downward propagation of these oscillating temperature maxima, and estimated their period to be around 15 years. Although there are less visible cloud features on Saturn than on Jupiter, a unique hexagonal pattern was found at 77° . It rotates with the radio rotation period of Saturn. Also, a strong high altitude narrow jet was detected at the equatorial tropopause (García-Melendo et al. 2010).

The upper tropospheric and lower stratospheric circulation patterns on giant planets can be inferred by studying the ortho-to-para ratio (OPR) of molecular hydrogen. In the interior of gas giants, where temperature is very high, the normal 3:1 OPR is maintained (Conrath and Gierasch 1983) because the transitions do not occur at higher temperatures. The upwelling warm air tends to retain the initial ratio, and this upwelling can be traced by using the OPR as a proxy, because the para-fraction at equilibrium increases as the air becomes cooler. It is known that the molecular hydrogen equilibration time on Saturn is of the order of 10^8 sec. Fletcher et al. (2007) retrieved the para-hydrogen distribution for Saturn, and Fouchet et al. (2003) and Conrath et al. (1998) calculated it for all the giant planets. The energy release from ortho-to-para conversion is assumed to play a role in the generation of localized thermal structures. There are many constraints to study the meridional circulation and wave activity. Ground-based continuous observations of Saturn include ring shadow effects, while continuous space-born Saturnian year-long observations are difficult to achieve. On the other hand, the Saturnian atmosphere experiences more seasonal variations than on Jupiter, because of the high axial tilt and ring shadow-induced cooling effects. However, these seasonal effects are much weaker than on the inner planets, due to the smaller latitudinal gradient of radiative heating (Conrath et al. 1990).

3.2 Simulations

3.2.1 Experiments setup

In our simulations, we adopt the basic planetary parameters for Saturn, which are summarized in Table 1.1. There are several mechanisms proposed to explain the wind distribution in the tropospheres of gas giants (e.g., Liu and Schneider 2010, and references therein). All of them are related to heating and convective mixing in the interior. As the gas planet has no surface, the wind at the lower boundary of the model does not vanish. To circumvent the problem with generating a realistic tropospheric wind in the model, we use the nudging technique to bring the simulated wind closer to the prescribed zonal wind u_{obs} at the lower boundary (Figure 3.2). The latitudinal distribution of the zonal wind \bar{u}_{obs} was taken from the Cassini/VIMS cloud tracking measurements of Choi et al. (2009) (their Figure 5) in the troposphere. Other recent applications of GCMs to the atmosphere of Saturn include (Lian and Showman 2010, Liu and Schneider 2010, Friedson and Moses 2012), and specifically the modeling of Saturn’s long-lived anticyclones (García-Melendo et al. 2007).

In the simulations presented here, 41 equally spaced log-pressure levels cover the domain between 2 bar and $10 \mu\text{bar}$. The “standard” horizontal resolution was 90×120 in longitude and latitude, correspondingly. This resolution coincides with that from the recent Saturn GCM simulations by Friedson and Moses (2012).

3.2.2 Sensitivity to the diffusion coefficient

The diffusion scheme is one of the important design aspects of GCMs. It is a common procedure in modeling studies to introduce damping mechanisms to parameterize fric-

tional effects and physical subgrid-scale processes, which are not included in the model. This is usually done in the form of a subgrid-scale diffusion and/or Rayleigh friction (e.g. Dowling et al. 1998). Numerical models often use Rayleigh friction at the top layers of the model to damp the waves reflected from the lid, and which physically should not present there. To overcome the difficulties associated with the decrease of density with altitude, an increasing with height diffusion coefficient is used in the model. At the same time, no artificial Rayleigh friction is applied. The implemented horizontal diffusion, which parameterizes the subgrid-scale processes helps to remove the computational modes arising from the centered finite differences and other instabilities generated in the model.

The aim of the experiments to be described here was to evaluate the importance and effects of the implemented horizontal diffusion scheme. The strength of diffusion is determined by the diffusion coefficient. In order to study the influence of the diffusion coefficient on the simulated dynamics, GCM runs with the “standard low” resolution (90×120 in latitude and longitude, respectively), have been performed. The horizontal dissipation was applied to the prognostic fields: temperature, meridional, and zonal wind. Sensitivity studies were performed to find a suitable least damping diffusion coefficient. Below we compare the results for the two differing coefficients. The time step for this simulations was set to 10 s, and the radiative relaxation time was of the order of 10^6 s. The diffusion coefficients used in these experiments were $K_H = 7 \times 10^6 \exp(0.85 \times 10^{-5}z)$ $\text{m}^2 \text{s}^{-1}$ (low) and $K_H = 8 \times 10^6 \exp(0.85 \times 10^{-5}z)$ $\text{m}^2 \text{s}^{-1}$ (high), where z is the model height. Their profiles are shown in Figure 3.3. It is known that low order diffusion affects both small (high wavenumber) and large (low wavenumber) spatial scales, whereas higher order diffusion affects mostly small spatial scales. Hence, the implemented second order filter is assumed to parameterize the unresolved subgrid scale processes. The estimated damping time for the diffusion terms in equations (2.23, 2.24, 2.25) is ≈ 5 Saturnian days.

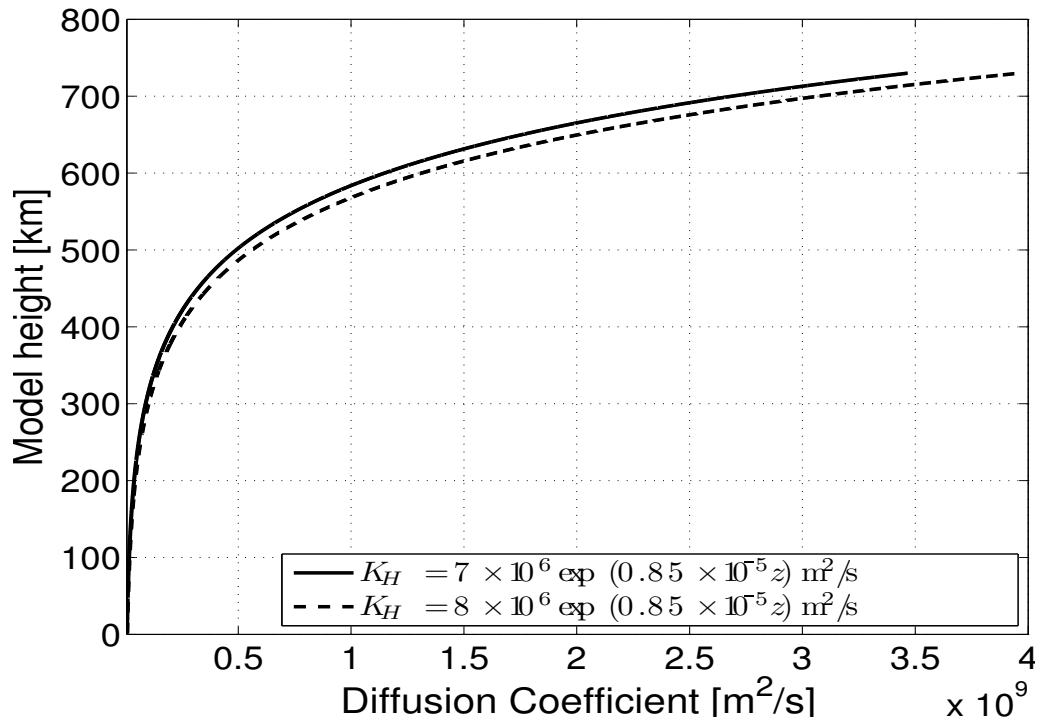


Figure 3.3: The diffusion coefficient profiles used in the sensitivity simulations.

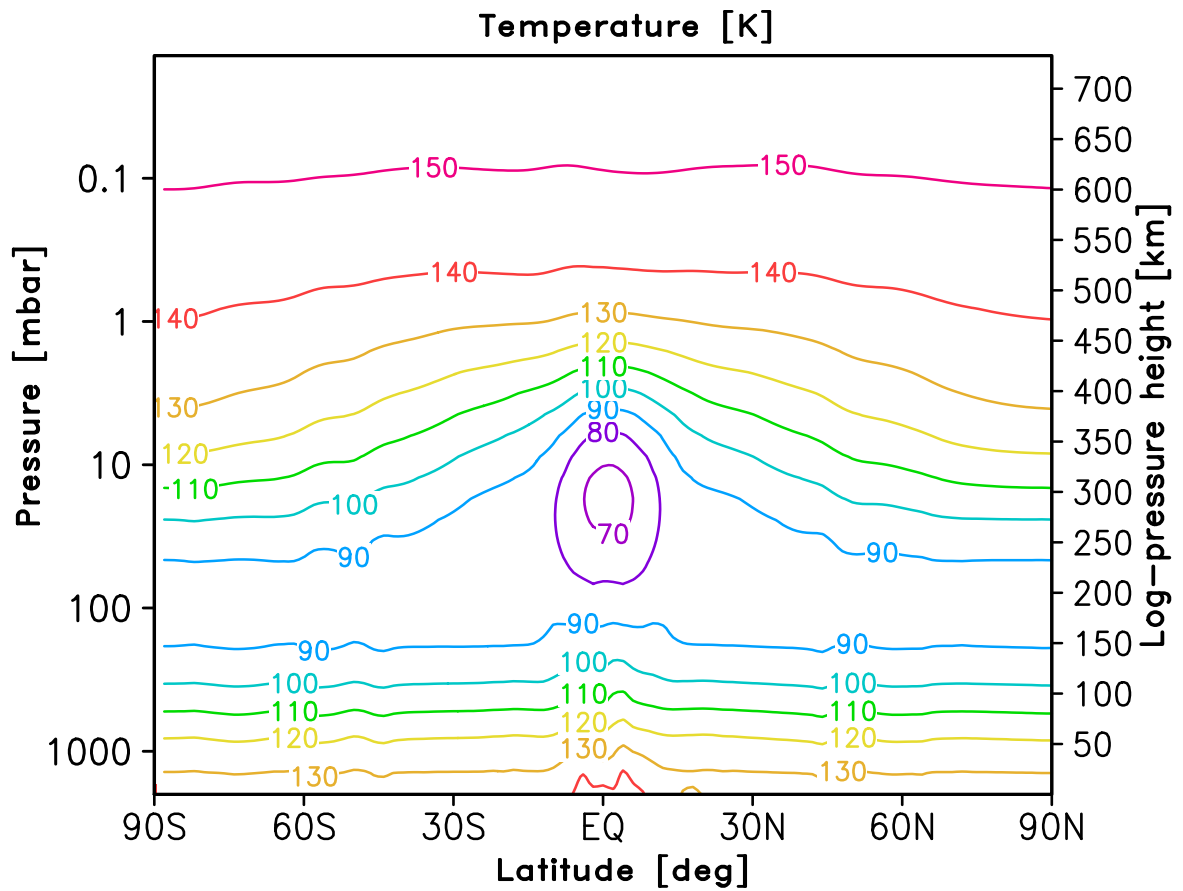


Figure 3.4: Simulated zonal mean temperature.

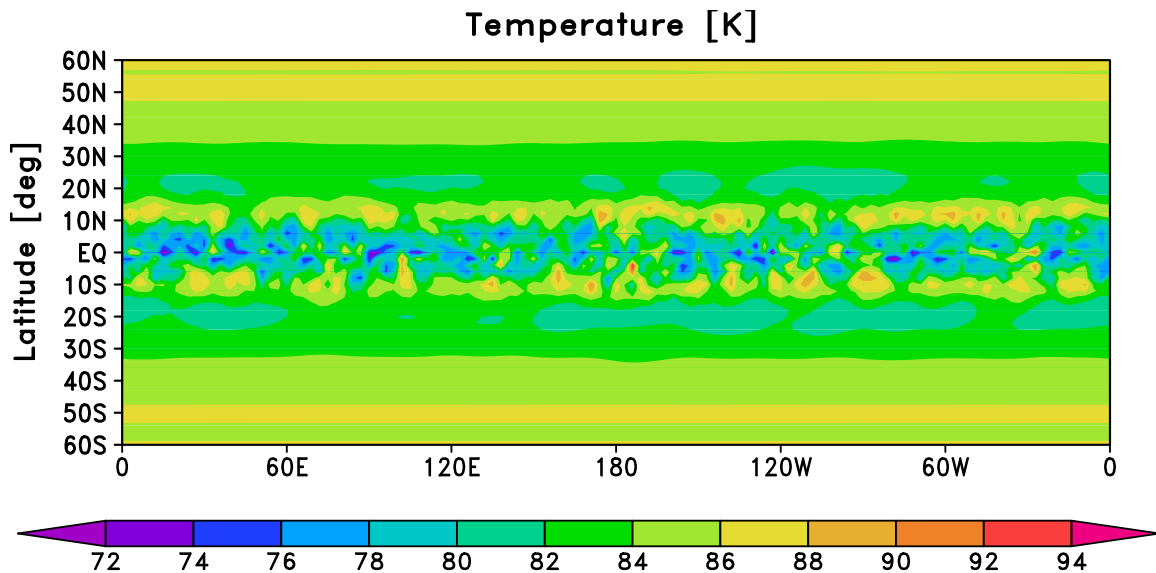


Figure 3.5: Latitude-longitude cross-section of temperature at 60 mb simulated with low diffusion coefficient.

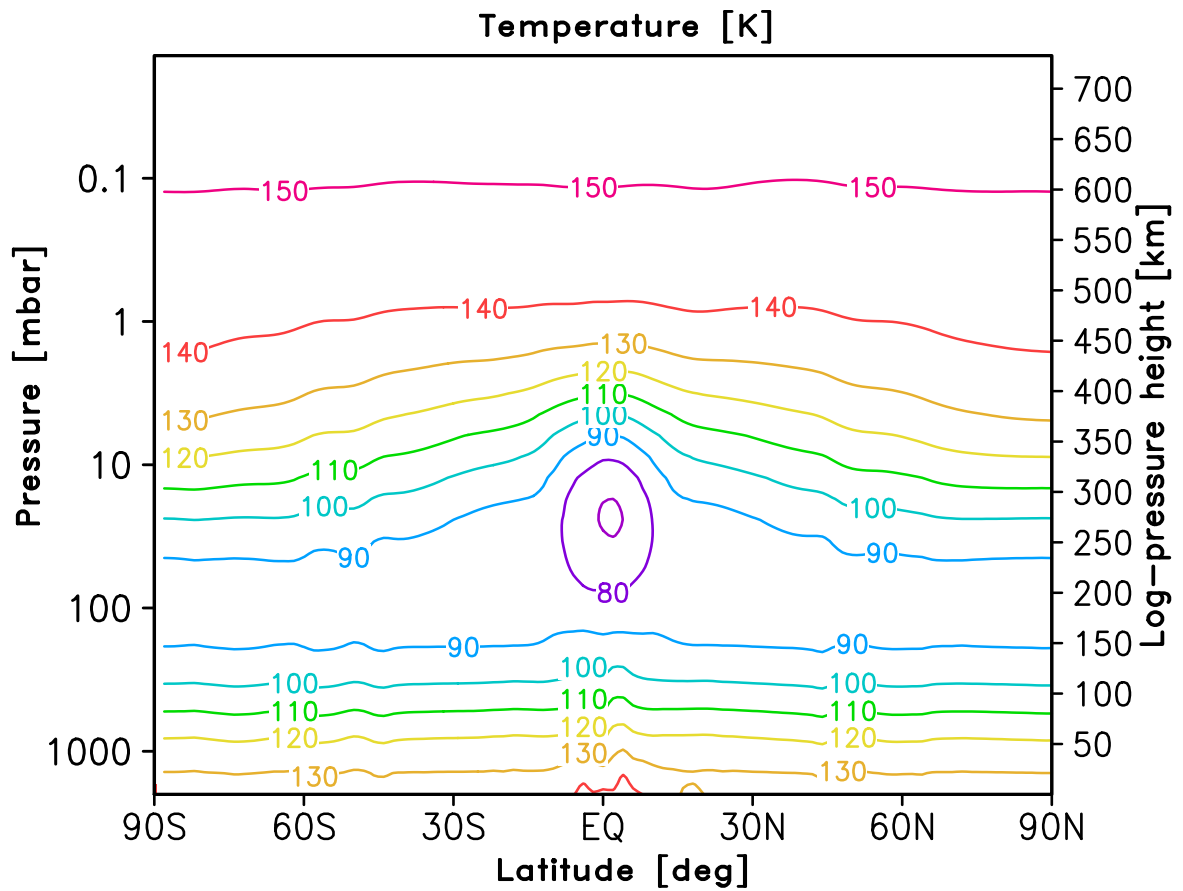


Figure 3.6: Zonal mean temperature simulated with the high diffusion coefficient

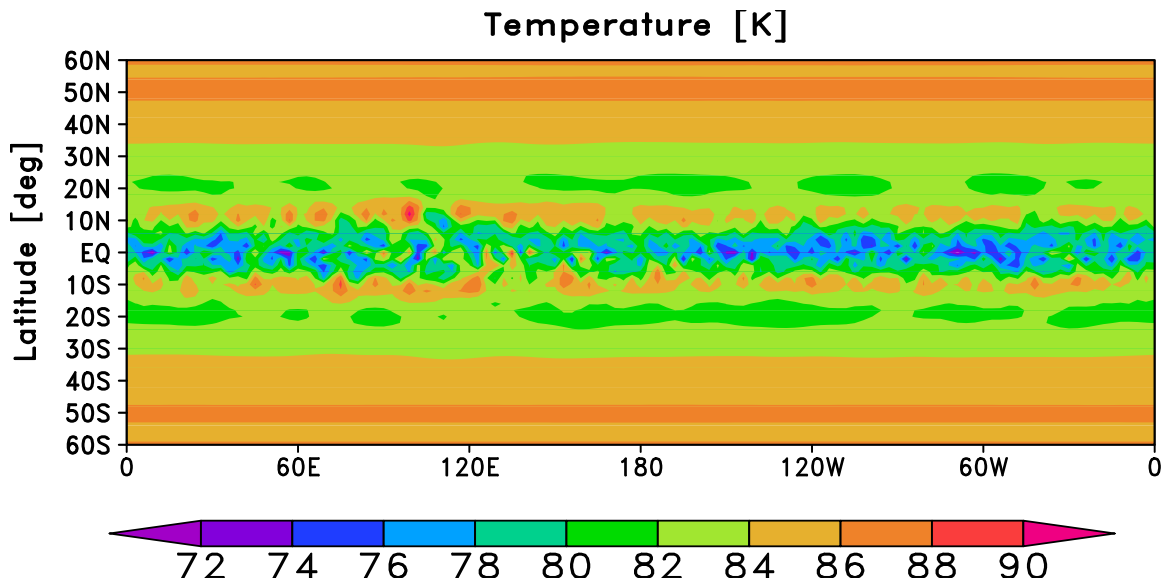


Figure 3.7: Latitude-longitude cross-section of temperature at 60 mb simulated with the high diffusion coefficient.

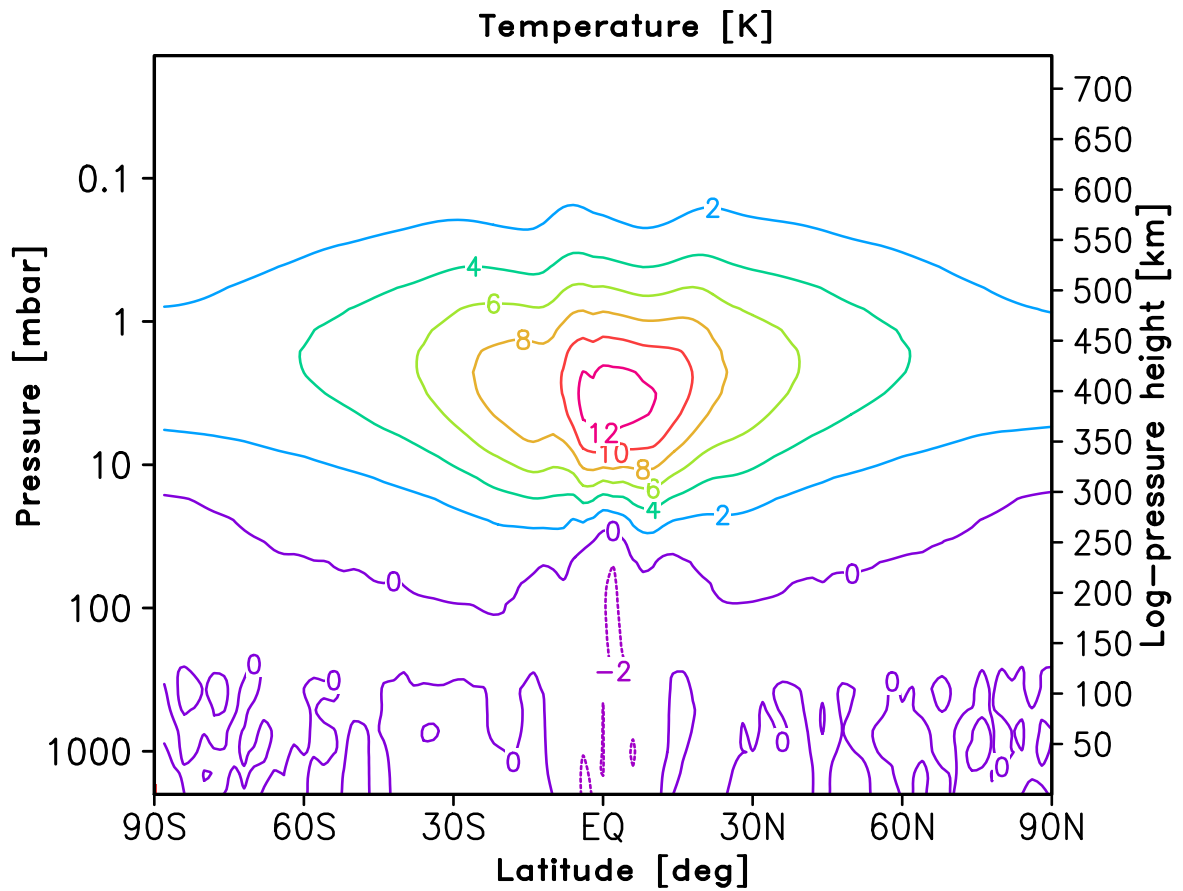


Figure 3.8: Difference between the simulated zonal mean temperature in the runs with high and low diffusion coefficient.

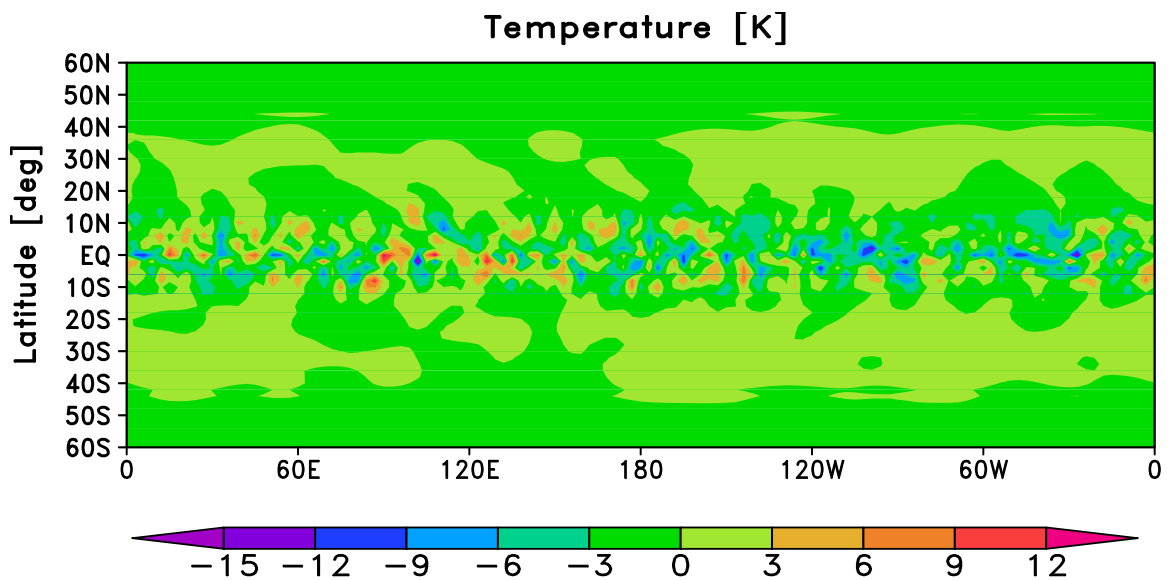


Figure 3.9: Latitude-longitude cross-sections of temperature at 60 mb in simulations with high and low diffusion coefficient.

Figures 3.4 and 3.6 present the zonal mean temperature simulated with low and high diffusion coefficients from Figure 3.3, respectively. The simulated temperature fields have higher values (≈ 12 K) for stronger diffusion. It is seen from the figures that applying the lower diffusion produces the elevated temperature minimum in the equatorial region. The difference between zonal mean temperatures in simulations with higher and lower diffusion is plotted in Figure 3.8. It shows that the maximum of warming occurs in the equatorial region above 100 mb. The difference decreases toward the poles, which is also evident from the plot for latitude-longitude distribution at 60 mb in Figure 3.9.

Figures 3.10a, 3.11a and 3.12a present the simulated planetary potential Φ (see section 2.1). It is a measure of the actual height of a pressure level above the lower boundary pressure level (1 bar), and characterizes the potential energy of the air parcels in the gravity field of the planet. At a certain height h , the planetary potential is defined as

$$\Phi(h) = \int_0^h g(\phi, z) dz, \quad (3.2)$$

where g is the acceleration of gravity, z is the height, and ϕ is the latitude. The simulated zonal mean planetary potentials for low- and high diffusion (Figures 3.10a and 3.11a, correspondingly) are of similar structure, but the difference plot (Figure 3.12a) indicates that Φ increases in the high-diffusion simulation above ~ 10 mb, and decreases below it. Such changes reflect the changes in temperature. Latitudinal variations of the planetary potential below ~ 10 mb associated with circulation cells can be seen in Figure 3.12a. These deviations of Φ maximize in the equatorial region, although the applied diffusion coefficient is latitudinally independent.

Similarly, high- and low-diffusion simulations produced differences in the mean zonal and meridional winds (Figures 3.10b, 3.10c, 3.11b, and 3.11c). As follows from Figure 3.12b, stronger diffusion produces more damping on the zonal winds, and both prograde and retrograde simulated jets are weaker when diffusion increases: the difference becomes negative in the regions of the prograde jets, and positive where the jets are retrograde. Thus, the use of the stronger diffusive damping provides more stability to the model.

The simulated vertical velocity shows very complex patterns, and has steep increases below ~ 500 mb. It also slightly decreases with increase of the diffusion coefficient. Figures 3.10e and 3.10f present latitude-longitude cross-sections of the meridional and zonal wind deviations from their zonal mean values at 60 mb in the "low-diffusion" simulation, respectively. Similarly, Figures 3.10e and 3.10f display similar snapshots for the "high-diffusion" run. The difference between the two simulated fields (Figures 3.12e and 3.12f) is very large (hundreds of m s^{-1}), especially in the equatorial belt. It may be concluded that increase of numerical diffusion in the GCM strongly affects the simulated eddies, while it alters mean fields less significantly. Thus, an adequate representation of wave-mean flow interactions in the model requires a use of lower possible horizontal diffusion.

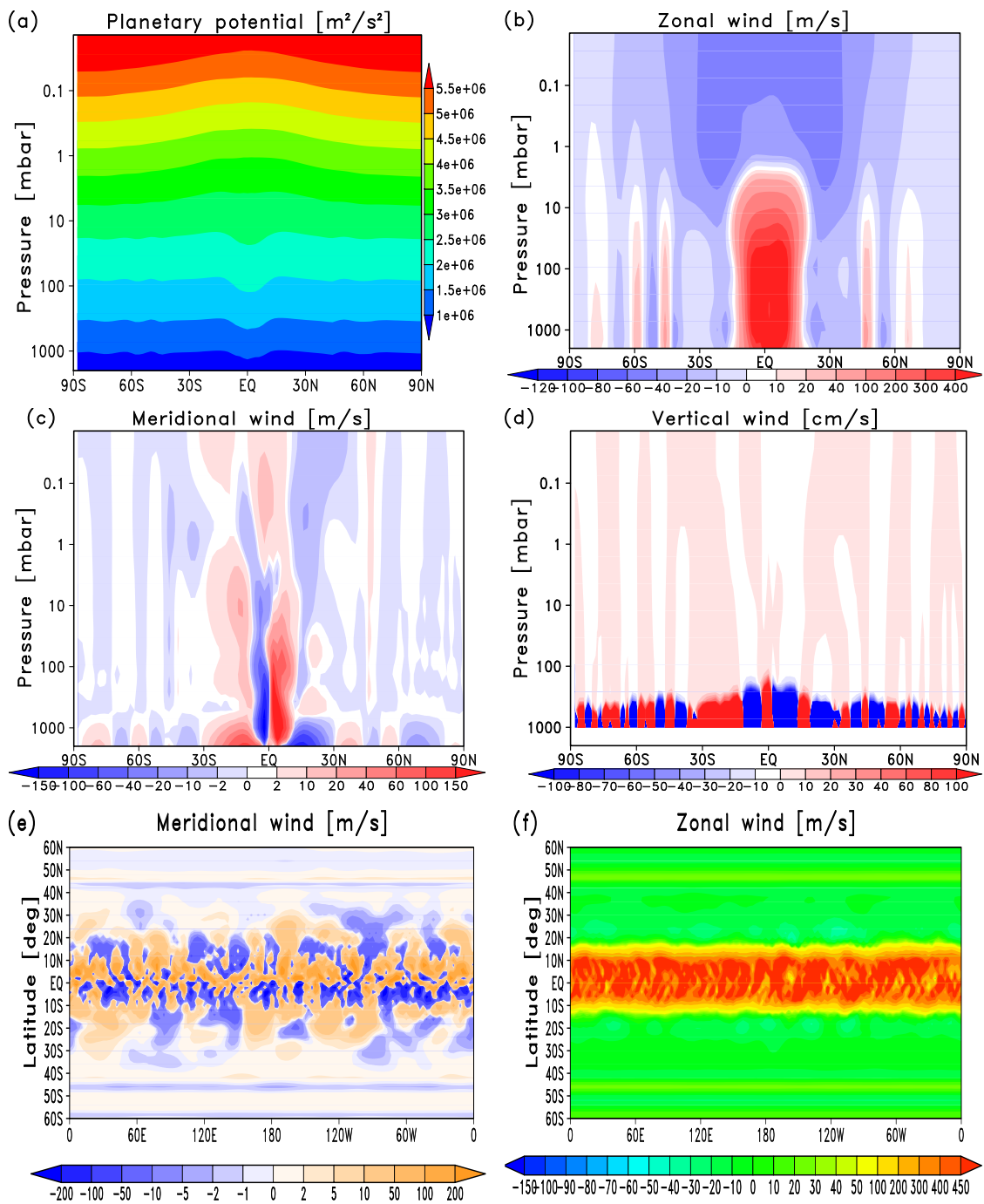


Figure 3.10: Simulation with the low diffusion coefficient, a) zonal mean planetary potential ($\text{m}^2 \text{s}^{-2}$), b) zonal mean zonal wind (m s^{-1}), c) zonal mean meridional wind (m s^{-1}), d) zonal mean vertical velocity (cm s^{-1}), e) latitude-longitude cross section of the deviations of the meridional wind from the zonal mean values at 60 mb, and f) latitude-longitude cross-section of the zonal wind at 60 mb.

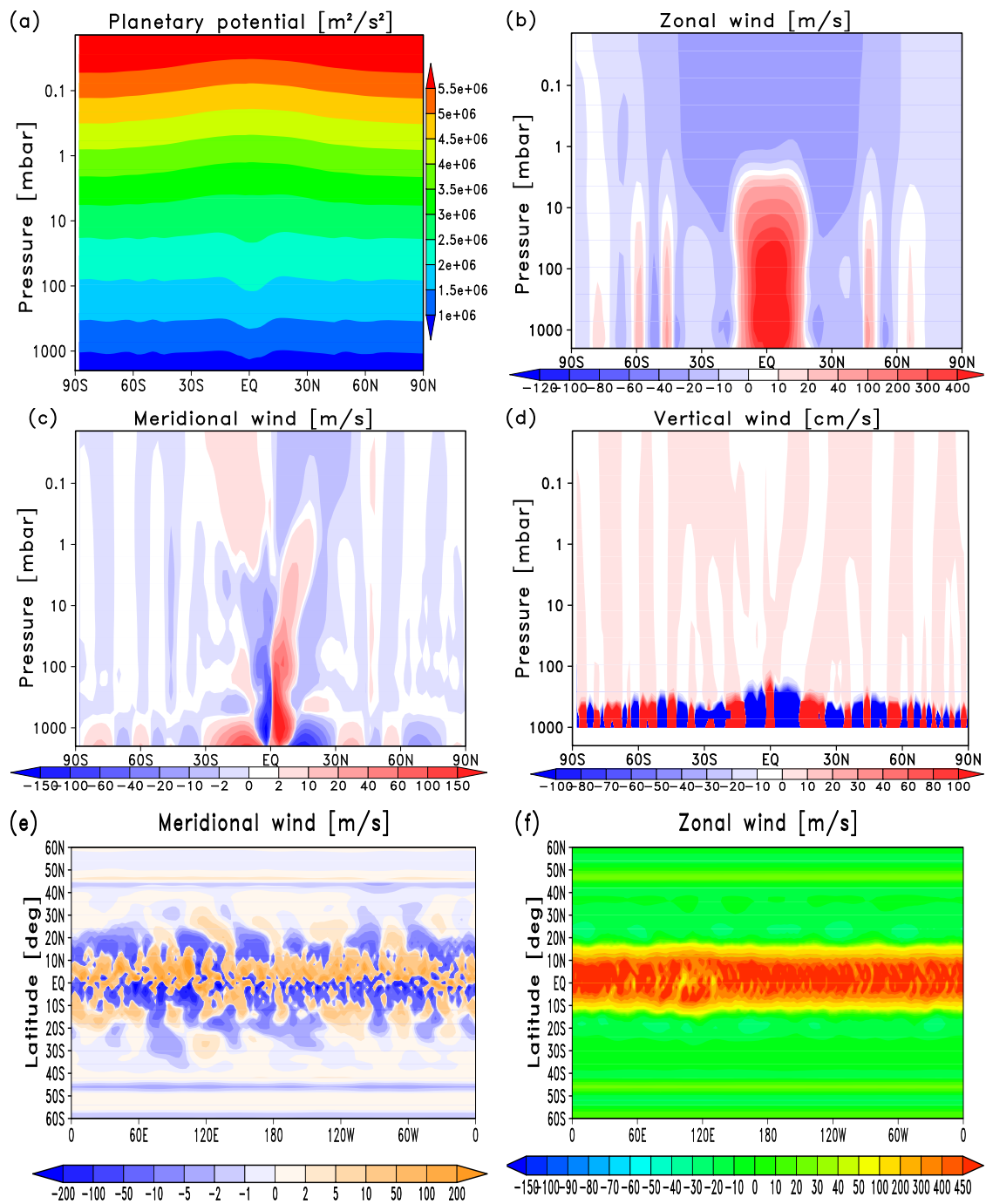


Figure 3.11: Simulation with the high diffusion coefficient, a) zonal mean planetary potential ($\text{m}^2 \text{s}^{-2}$), b) zonal mean zonal wind (m s^{-1}), c) zonal mean meridional wind (m s^{-1}), d) zonal mean vertical velocities (cm s^{-1}), e) latitude-longitude cross-section of the deviations of the meridional wind from the zonal mean values at 60 mb, and f) latitude-longitude cross-section of zonal wind at 60 mb.

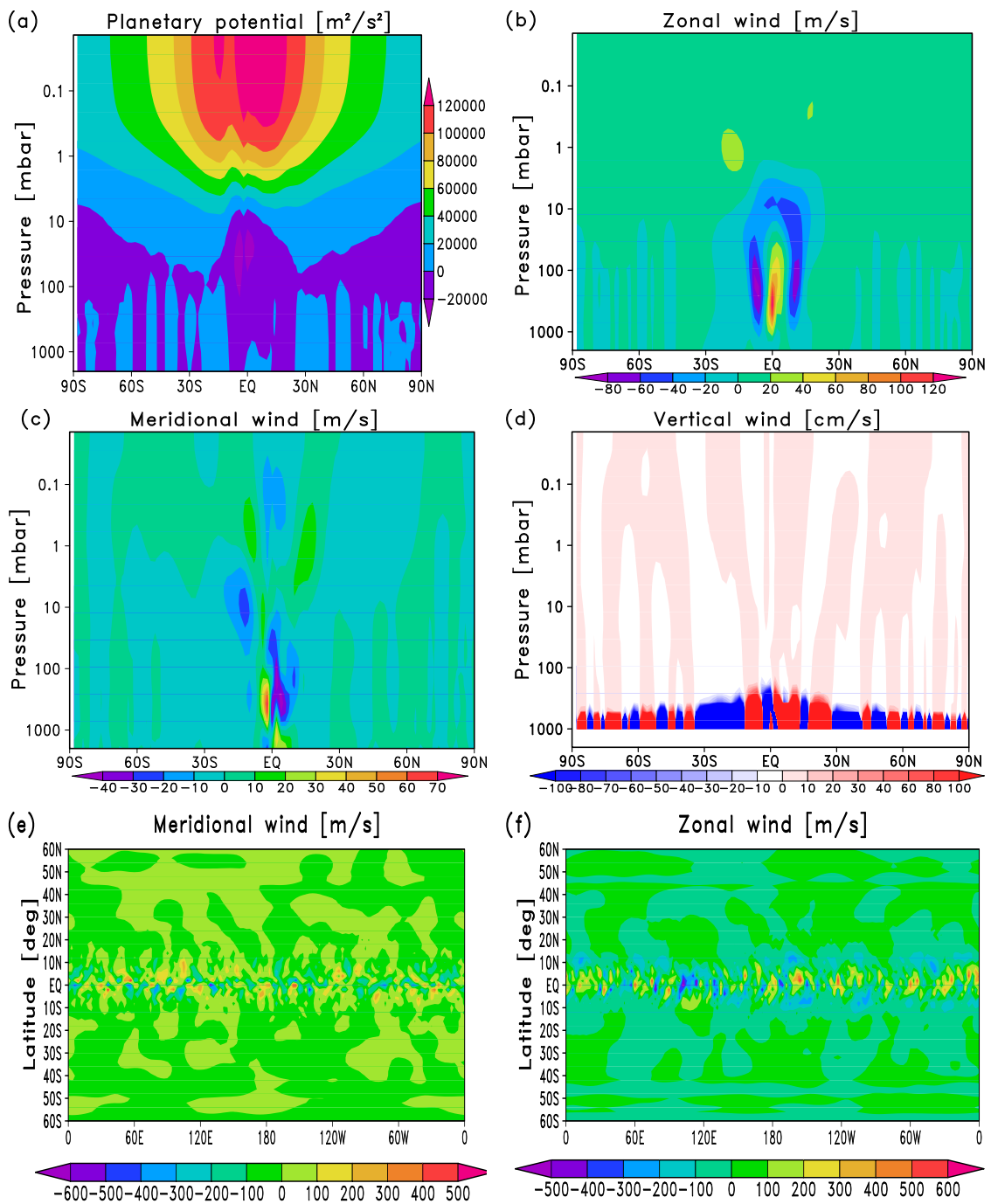


Figure 3.12: Difference between the simulations with high and low diffusion: a) zonal mean planetary potential ($\text{m}^2 \text{s}^{-2}$), b) zonal mean zonal wind (m s^{-1}), c) zonal mean meridional wind (m s^{-1}), d) zonal mean vertical velocities (m s^{-1}), e) latitude-longitude cross-section of the difference of the meridional wind from the zonal mean values at 60 mb, and f) latitude-longitude cross-section of the zonal wind at 60 mb.

3.2.3 Higher resolution simulations

To estimate dynamical effects associated with higher model resolution, we performed simulations with 180×240 grid points in latitude and longitude, correspondingly. This resolution is twice higher than that employed in recent Saturnian GCMs (Friedson and Moses 2012), and in the previous subsection. An extremely small time steps (~ 3 s) had to be used to comply with the CFL stability criterion. The near-pole filter had to be extended to 12 latitudinal grid points to maintain the model stability. The number of vertical levels was kept the same as in the "lower-resolution" version (41), and the horizontal diffusion coefficient was set to $K_H = 7 \times 10^6 \exp(0.85 \times 10^{-5}z)$ $\text{m}^2 \text{s}^{-1}$. The radiative relaxation time τ_{rad} was of the order of 10^7 s. Due to this setup, the seasonal, diurnal, and ring shadow effects were not considered, as in the previous experiments. Similar formulations have been used in simulations of the giant planet atmospheres (Simon-Miller et al. 2006, Zuchowski et al. 2009b). As in the work of Zuchowski et al. (2009b), we applied a shorter radiative relaxation time to take advantage of the shorter computational time for achieving a quasi-balanced state. A partial justification for this step was the finding of Simon-Miller et al. (2006) that τ_{rad} was shorter in the stratosphere than the estimate of Conrath et al. (1990) (≈ 1 Earth year against ~ 2.1). The high resolution simulation was done over 3000 Saturnian days, which is ~ 10 times the e-folding time for the τ_{rad} used in the model to allow the simulated fields to relax well towards the prescribed equilibrium temperature.

Potentially, a higher resolution model can produce better results, but the extent of the improvement and effectiveness of the chosen resolution have to be studied in sensitivity tests. For motions with horizontal scales close to L_D , the pressure gradient force is balanced by the Coriolis force and buoyancy almost equally. At shorter scales, the buoyancy dominates the Coriolis force. Resolving scales smaller than L_D is of much importance for proper capturing the baroclinic development of eddies in models, and, as a result, their influence on mean fields.

The Rossby radius of deformation, $L_D = NH/f$ varies with latitude as $1/\sin \phi$ due to the dependence of the Coriolis force: $f = 2\Omega \sin \phi$. The latitudinal variations of the ratio $L_D/\Delta y$, Δy being the resolution in the meridional direction, is shown in Figure 3.13. The grid length Δx decreases with latitude $\propto \cos \phi$, and the similar ratio for the zonal direction, $L_D/\Delta x$, plotted in Figure 3.14 is somewhat different. The Brunt-Väisälä frequency N is a measure of static stability of the atmosphere. For calculations in Figures 3.13 and 3.14, we estimated it as

$$N = \sqrt{\frac{g}{\theta} \frac{d\theta}{dz}} = \sqrt{g/H} \approx 0.02 \text{ s}^{-2}. \quad (3.3)$$

Figures 3.13 and 3.14 demonstrate a general tendency of resolving motions better in low latitudes. Assuming that the model marginally resolves the Rossby radius at $L_D = 2\Delta x$ (and/or $2\Delta y$), the points in the graphic lying above $L_D/2\Delta x, y = 2$ indicate areas on the globe, where the resolution is marginally adequate. As is seen from the figures, our GCM in the "high-resolution" setup resolves the Rossby radius in both latitudinal and longitudinal directions.

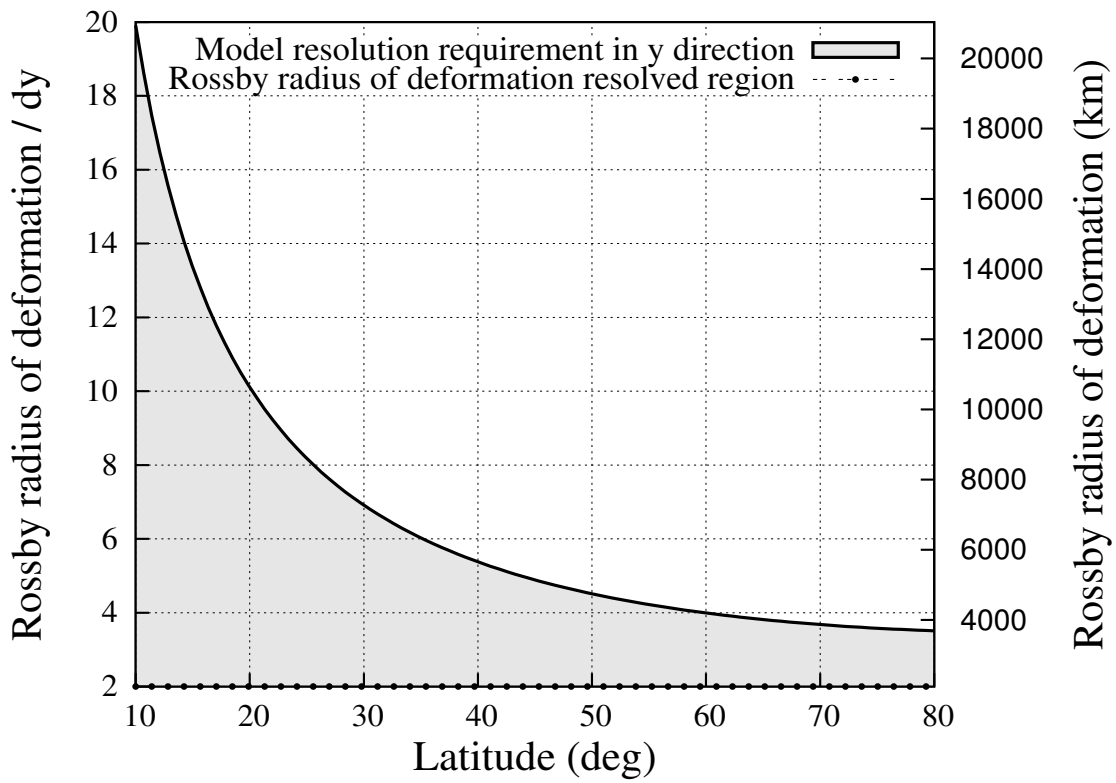


Figure 3.13: Ratio of Rossby radius of deformation and grid length in the latitudinal direction for “high-resolution GCM setup”.

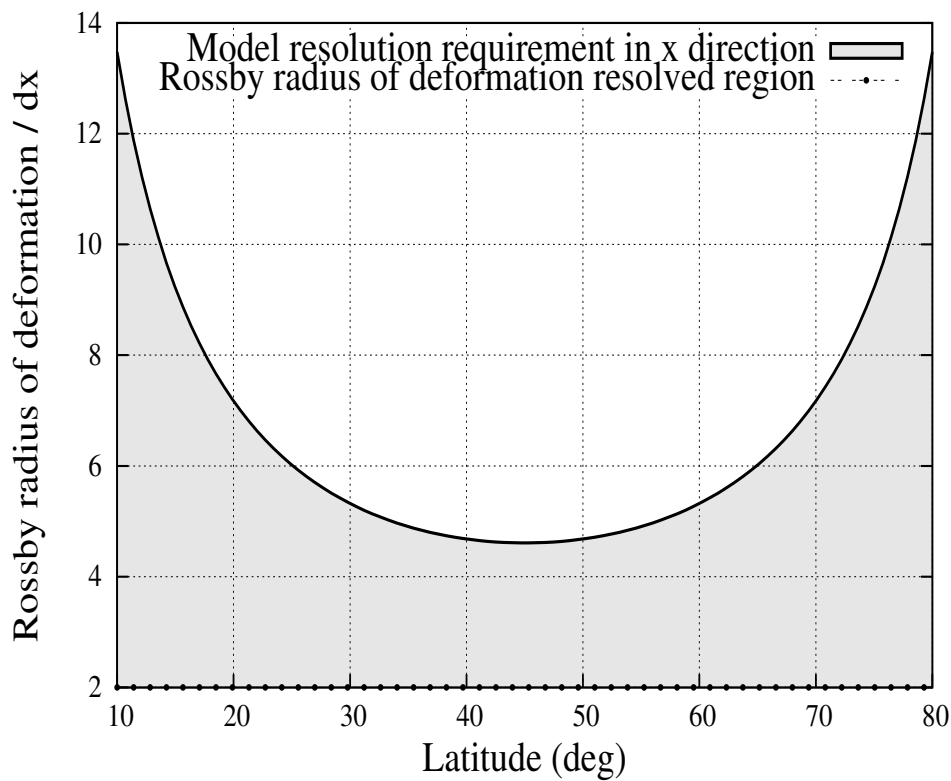


Figure 3.14: The same as in Figure 3.13, but for the meridional direction.

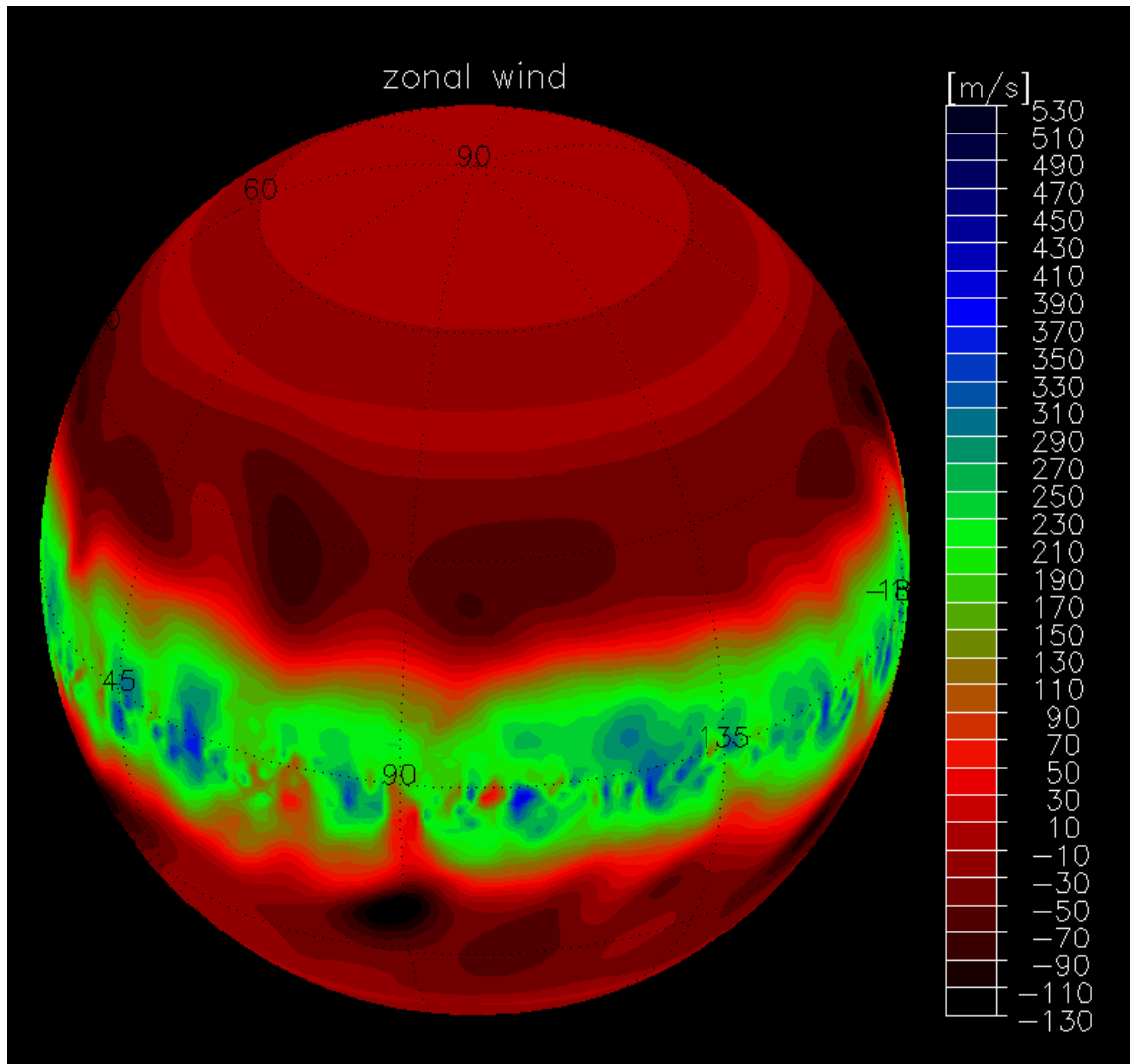


Figure 3.15: A global view on the simulated Saturn atmosphere: zonal wind at 6 mb. Dark blue and red areas denote maxima of prograde and retrograde jets, correspondingly.

Figure 3.15 presents a global view on the Saturnian zonal winds at 10 mb pressure level from the “high-resolution” simulation. A complex pattern of large- and small-scale eddies is seen in the equatorial area, where the resolution is most adequate. In midlatitudes, the planetary-scale eddies with wavenumbers ~ 4 – 5 dominate. The zonal mean temperature given in Figure 4.9 can be directly compared with that from the “low-resolution” simulation (Figure 3.4). It is seen that, besides more smaller-scale latitudinal features, the temperature also shows some larger-scale changes. The most noticeable are a) the warmer equatorial minimum in the “high-res” run (80 vs 70 K), and b) warmings in the polar regions between 10 and 1 mb (150 vs 120–140 K). A longitude-latitude snapshot of temperature at 60 mb (Figure 4.10) demonstrates that eddies extend farther to midlatitudes in accordance with the arguments on the Rossby radius resolution. They have smaller-scale contribution, and their magnitudes are somewhat larger.

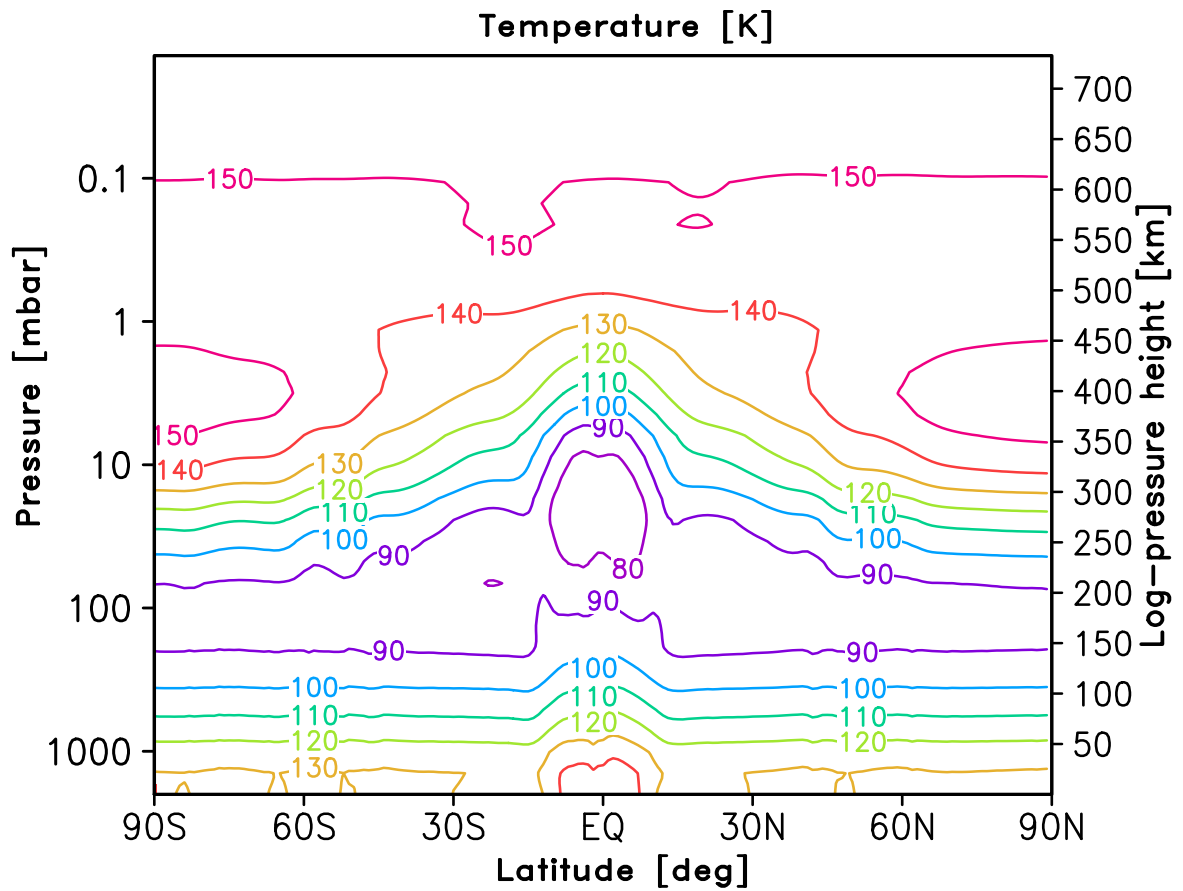


Figure 3.16: Saturnian zonal mean temperature from the “high-resolution” simulation.

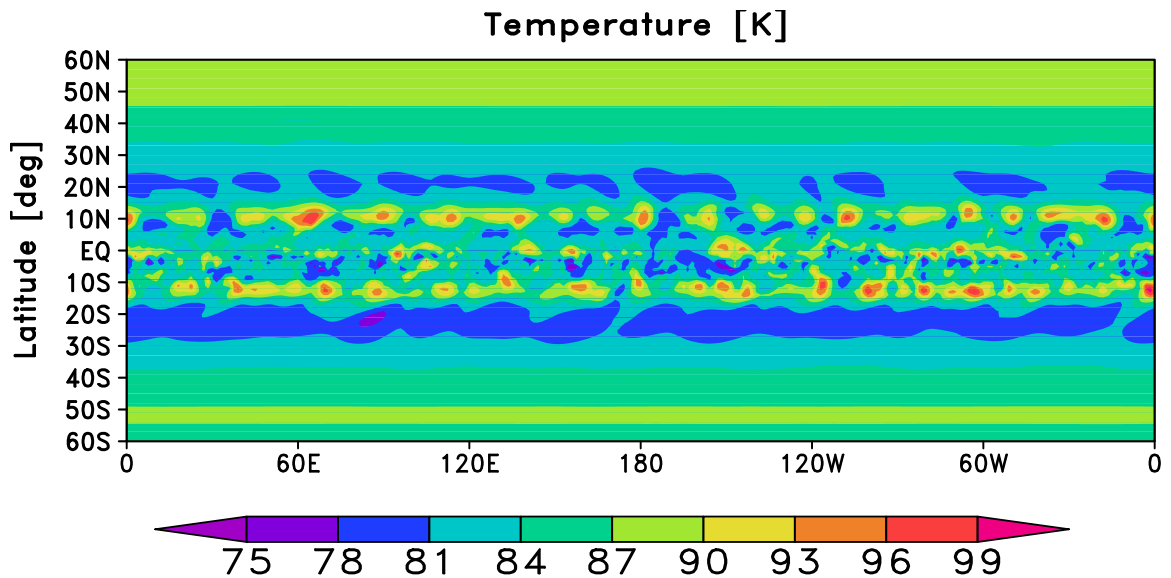


Figure 3.17: Latitude-longitude distribution of the simulated temperature at 60 mb in the “high resolution” run.

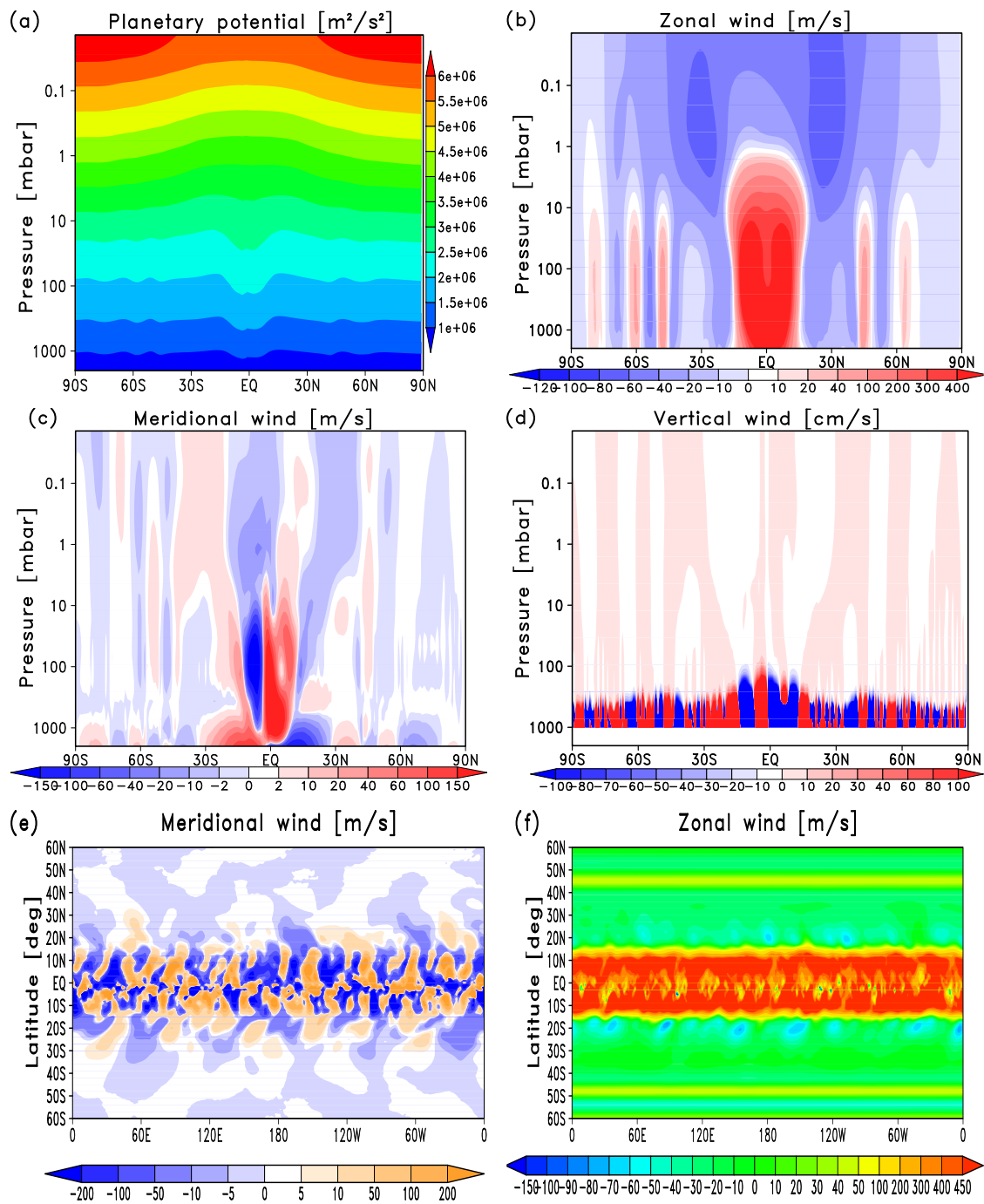


Figure 3.18: Higher resolution simulations of Saturn: a) zonal mean planetary potential ($\text{m}^2 \text{s}^{-2}$), b) zonal mean zonal wind (m s^{-1}), c) zonal mean meridional wind (m s^{-1}), d) zonal mean vertical wind (m s^{-1}), e) latitude-longitude cross-section of the meridional wind deviations from zonal mean at 60 mb, and f) latitude-longitude cross-section of zonal wind at 60 mb.

The simulated zonal mean planetary potential plotted in Figure 3.18a shows more small-scale variations than in the “low-res” run below ~ 10 mb. In the upper layers, the planetary potential is very close to that in Figure 3.10a, indicating that the higher res-

olution introduced more changes in the lower atmosphere. The mean zonal wind (Figure 3.18b) has almost identical patterns, but somewhat stronger. The simulated equatorial prograde wind extends up to ~ 1 mb, then reverses with a dumbbell shape over the prograde jet with maxima on both sides of the equator. Alternating prograde and retrograde jets extend upward from the lower boundary, but the upper middle atmosphere is dominated by the retrograde jet. The wind speed maximum exceeds 400 m s^{-1} with the peak around 100 mb. Higher, the equatorial prograde jet core splits into two parts, but the splitting is not seen for winds slower than 200 m s^{-1} . The meridional wind plotted in Figure 3.18c shows strong poleward circulation cells above 1 bar in the equatorial region. This pattern extends upward almost to the top of the model with smaller magnitudes. Alternating cells in mid- and high latitudes also extend to the upper layers with a net weak transport towards the poles. The vertical velocities depicted in Figure 3.18d are in line with these circulation cells. In the lower atmosphere, the vertical upward and downward velocities are particularly large. Their magnitude rapidly decay with height, and is around $<10 \text{ cm s}^{-1}$ in the upper layers. The latitude-longitude cross-section of the zonal wind at 60 mb plotted in Figure 3.18(f) clearly shows longitudinal variations superimposing the zonal jets in the equatorial area. Planetary waves with wavenumber 9 are seen at the both sides of equator around $\pm 20^\circ$. Two prograde jets with the magnitude $\sim 50 \text{ m s}^{-1}$ are seen around 50°S and 45°N . To highlight the eddy structure of the simulated fields, we plotted the deviations of meridional wind from the zonal-mean values in Figure 3.18e. It illustrates that the eddy activity is very strong between 30°S and 30°N , where the model best resolves the Rossby deformation radius.

3.2.4 Wave activity in the middle atmosphere

Having considered the zonally averaged fields, we turn attention at the simulated non-zonal disturbances. They are not artifacts of our GCM, but are intrinsic features of the Saturnian atmosphere. A detailed description of Saturn's observed waves is given by Achterberg and Flasar (1996). The equatorial region has a very rich wave dynamics with a broad nomenclature of atmospheric waves. Briefly, they can be grouped into Kelvin and mixed Rossby-gravity waves. Rossby-gravity waves propagate westward with respect to the mean flow, and provide a westward momentum upon their breaking or dissipation (Fouchet et al. 2008). Kelvin waves propagate eastward, and produce an eastward stress on the mean jet. Liming et al. (2008) found in the CIRS data a thermal equatorial wave number 9 on Saturn, which apparently belongs to the class of Rossby-gravity waves. These planetary-scale waves can break when propagate to the upper stratosphere, and affect the circulation above the height of their origin in the troposphere. Another well documented disturbance on Saturn is the Northern hemispheric ribbon wave (Sanchez-Lavega 2002). Studies of Saturnian zonal wind speeds (Del Genio and Barbara 2012) confirm the importance of eddies in maintaining the meridional circulation.

It has been found that quasi-biennial oscillations (QBO) with an average period of 28 months on Earth are caused by interactions of vertically propagating gravity waves with a downward propagating alternating easterly and westerly zonal wind (Lindzen, R. S. and Holton, J. R. 1968, Baldwin et al. 2001). In general, zonal-mean oscillations that propagate downward indicate a strong waves activity in the atmosphere. Such activity has been detected on Saturn from Cassini radio occultation data (Schinder et al. 2011). It has

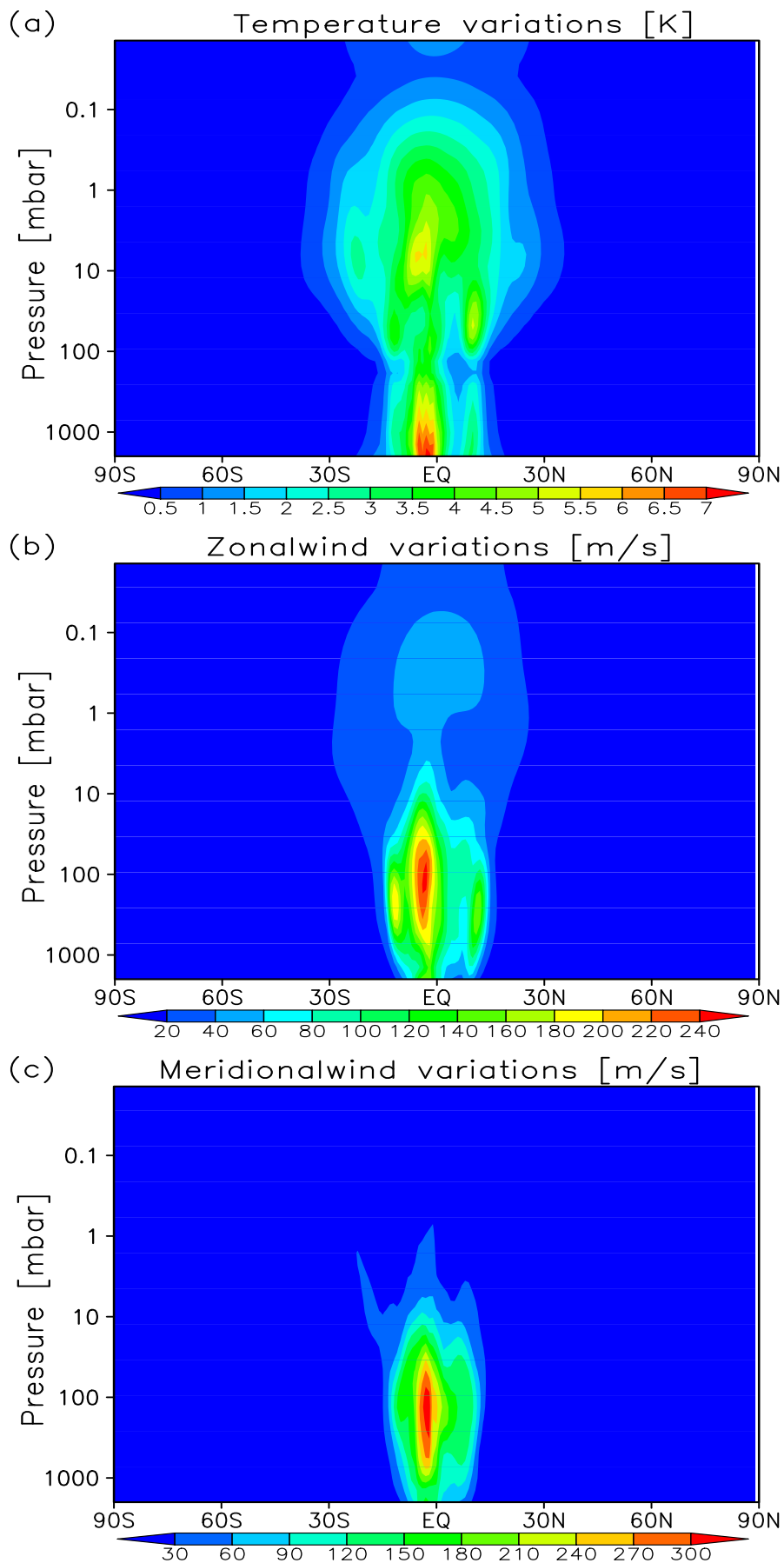


Figure 3.19: Root-mean square variations of the simulated fields: a) temperature, b) zonal wind, and c) meridional wind.

been shown by Sayanagi and Showman (2007) that the waves excited by the storm on Saturn can transport westward momentum from the troposphere to the stratosphere. As a result of the momentum deposition, the equatorial jet can be slowed down by $\approx 40 \text{ m s}^{-1}$. Such slow-down of the equatorial jet was already observed on Saturn (Sánchez-Lavega et al. 2003).

Figure 4.10 shows the simulated thermal waves similar to those observed by Liming et al. (2008). The component with the wavenumber 9 is clearly seen, and coincides with that of the Rossby-gravity wave found by Liming et al. (2008). Non-zonal disturbances with the similar wave number ~ 9 can also be seen in the higher resolution simulations (Figure 3.18f), and in the latitude-longitude cross-section of temperature at 60 mb (Figure 4.10).

The overall simulated wave activity is presented in Figure 3.19 in the form of Root Mean Square (RMS) of the temperature, zonal wind, and meridional wind fluctuations. The plots indicate that the disturbances are strong in the equatorial region, extend to higher levels, and their magnitudes decay with height. The amplitudes of the wind fluctuations are close or exceed the mean zonal wind near the equator, and the entire dynamics is dominated by eddies. The temperature variability (Figure 3.19a) has two equatorial maxima around ~ 2 and ~ 10 mb. On the other hand, the zonal wind (Figure 3.19b) has maxima around ~ 100 and ~ 0.2 mb. These variability plots indicate a presence of vertical oscillating structure reminiscent of semi-annual oscillations (SAO). Long-term simulations of many Saturnian years taking account of the seasonal modulation of radiative forcing are required to study these processes. Variability of the meridional wind (Figure 3.19c) is mainly confined to lower levels below ~ 10 mb. This can be an indication that the meridional circulation cells in the upper stratosphere are weak.

3.3 Summary of results for Saturn stratosphere modeling

This chapter describes applications of the developed GCM to modeling the atmosphere of Saturn. Two lines of numerical experiments are presented here, which explore the sensitivity of simulated fields to 1) the strength of applied horizontal diffusion that represents a major tunable parameter, and 2) to the horizontal resolution of the GCM. The atmosphere of Saturn was chosen for this study because the requirements for model resolution are less demanding compared to Jupiter.

Studies with the varying diffusion coefficients indicate that the simulated temperature tends to increase for stronger diffusion, while zonal winds experience more damping and are weaker, especially in the equatorial region. The major changes induced by enhanced diffusion are confined to low latitudes.

The model successfully reproduced the observed zonal wind patterns, and revealed their vertical structure. There is a general lack of observations to validate these results, however they agree well with the recent GCM study by Friedson and Moses (2012). Simulations indicate that the magnitude of the zonal jets decrease with height, with retrograde winds dominating in the upper layers.

The higher-resolution simulations with a “low” diffusion demonstrated a strong eddy activity in low latitudes, with the magnitudes of wind disturbances exceeding the local

mean zonal flow. The simulated strong wave activity agrees well with observations. The study shows that the equatorial lower stratosphere is the most dynamically active region. Simulations with even higher resolution are required to find out whether the concentration of eddy activity in low latitudes is the dynamical phenomenon, or simply a result of insufficient resolution.

Seasonal forcing was not incorporated in the current version of the model, and, therefore could not be studied. Nevertheless, the model successfully reproduces many of observed planetary wave features. This may serve as an indication that the GCM will be able to reproduce seasonal variations such as the semi-annual oscillation (SAO) in the future, if (and when) a more realistic radiative scheme is included. A SAO has been observed in the Saturnian middle atmosphere (Orton et al. 2008, Fouchet et al. 2008), and is known to be a result of wave interactions with the seasonally varying mean flow.

4 Three-dimensional modeling of Jupiter's middle atmosphere

4.1 Observational constraints

Jupiter with an orbital radius of ~ 778 million km, is the biggest, fastest rotating, and most dynamically active planet in the Solar System (Helled et al. 2009). Its atmosphere has been a subject of intense observational and theoretical studies (Golitsyn 1979, Flasar 1986, Ingersoll 1990, Yano 1994, Gierasch and Conrath 1993, Gierasch 1996b,a, Seiff 2000, Ingersoll, A. P. et al. 2004, Dowling 1995, Magalhães et al. 1990, Schneider and Liu 2009, Yano et al. 2003, Showman 2002, Vasavada and Showman 2005, Cavalié et al. 2012, and references therein). In this chapter, we focus on simulations of large-scale circulation patterns as well as of smaller-scale dynamical features in the Jovian stratosphere.

The major components of the Jovian middle atmosphere are hydrogen (H_2) and helium (He). Their mixing ratios are ~ 0.86 and ~ 0.136 (Niemann et al. 1998), respectively. Other minor components include methane (CH_4), ethane (C_2H_6) and acetylene (C_2H_2) with mixing ratios 0.0018 (Niemann et al. 1998), 4.6×10^{-6} (Yelle et al. 2001), and 2.7×10^{-6} (Yelle et al. 2001), respectively. In addition to this, hydrogen sulfide (H_2S) is also found in the upper troposphere with a mole fraction of 0.86×10^{-6} (Niemann et al. 1998). A significant amount of aerosols has been detected in the Jovian middle atmosphere (Zhang et al. 2013), of which ammonia ice (NH_3) (Moses and Greathouse 2005), water ice and ammonia hydrosulfide (NH_4SH) have mixing ratios 0.0007, 0.0005 and 7.5×10^{-5} , respectively. The latitudinal variations of these aerosols, which are located at the poles primarily (Rages et al. 1999), can alter the radiative balance. The latitudinal distributions of many aerosols are well known, however, great uncertainties exist about their vertical distributions (Flasar 1986, Zhang et al. 2013).

4.1.1 Jovian troposphere

Jupiter's troposphere extends up to 280 mb, and is dominated by convection. As evident from the observed cloud features, it is dynamically very active and complex. From the Voyager data, the equator-to-pole temperature contrast in the troposphere is small (~ 2 K) (Orton et al. 1991, Dowling 1995, Aurnou et al. 2008). This indicates that the solar energy absorbed in the equatorial region is redistributed, and the troposphere is dynamically well mixed. It is assumed that the equilibration of the latitudinal temperature gradient occurs due to transport of heat by eddies and/or by deep circulation in the interior. Thus, the atmospheric dynamics is playing a major role in the transport of energy.

Visible and very active tropospheric cloud disturbances, a characteristic property of Jupiter, have been discussed in detail in previous studies (Matcheva et al. 2005, Conrath et al. 1981). The cloud layer lies approximately between 500 and 1000 mb, that is ≈ 50 km deep. It has a complex vertical structure, and consists of at least two layers dominated by ammonia (NH_3) and ammonia hydrosulphide (NH_4SH), and the third layer built of thin water clouds (Gierasch 1991, Banfield et al. 1998), as is evidenced by flashes of lightning detected in the atmosphere (Gibbard et al. 1995, Dyudina et al. 2004). Thermochemical models provide evidences for such vertical structure (Flasar 1986). For example, the Oxford Planetary Unified model System (OPUS) with an implemented simple cloud parameterization scheme for Jupiter (Zuchowski et al. 2009a) predicts water clouds in addition to the other components. It was suggested that fast moving clouds within hotspots are most likely built of water, and extend deeper than 3 bar (Li et al. 2006c). Recent observational studies found that water vapor deposited by the SL9 comet is still present in the stratosphere of Jupiter (Cavalié et al. 2013). Hence, moist convection is apparently an important energy source for maintaining the circulation in the troposphere (Ingersoll et al. 2000). In order to circumvent problems with modeling the complex processes in Jupiter's troposphere and concentrate on the middle atmosphere, we set the lower boundary of our GCM at 1 bar. Thus, the forcing at the lower boundary can be entirely based on observed tropospheric features.

4.1.2 Middle atmosphere temperature

Jupiter absorbs $\sim 8 \text{ W m}^{-2}$ of solar energy (Hanel et al. 1981, Young 2003), and receives $\sim 6 \text{ W m}^{-2}$ of internal heating energy (Ingersoll, A. P. et al. 2004, Gierasch et al. 2000, Guillot 2005). From Table 1.2, the energy balance on Jupiter (the ratio of absorbed power to emitted power) is 1.67 ± 0.09 . The energy balance as a function of latitude is given by Pirraglia (1984). The temperature structure of Jupiter's stratosphere is well known (Young 2003, Fletcher et al. 2010). Moreover, the *in situ* measurements of stratospheric temperature by the Galileo probe gives an accurate vertical temperature profile in the middle atmosphere and thermosphere (Young et al. 1996, Yelle et al. 2001). Thermal winds calculated from the latitude-height temperature map from 1 bar to 1 mb show alternating equatorial speeds with a prograde maximum above 10 mb (see Figure 4.1b) (Flasar et al. 2004, Simon-Miller et al. 2006).

Tropospheric temperature measurements show fewer fluctuations, but the stratospheric temperature shows more asymmetry. Thus, the temperature is $\sim 7^\circ\text{K}$ higher at 5 mb at the north than on the south (Nixon et al. 2007). Absorption by clouds could be a reason for the observed small temperature fluctuations at the tropopause (Matcheva et al. 2005), although previous studies could not find any correlation between temperature and cloud patterns. This may be an indication that the visible temperature features are driven by dynamics. The equilibrium temperature profile (see Figure 4.2) used in the model is in a good agreement with the radiative equilibrium temperature derived by Conrath et al. (1990) and Moreno and Sedano (1997) (see Figure 4.4a). Similar equilibrium temperature profile has been used in previous simulation studies (e.g. Friedson 1999). There are studies showing that the radiative relaxation time in the stratosphere is shorter than that from the previous estimates. For example, Simon-Miller et al. (2006) cross-correlation studies indicate that the relaxation time in the stratosphere is shorter than that from the

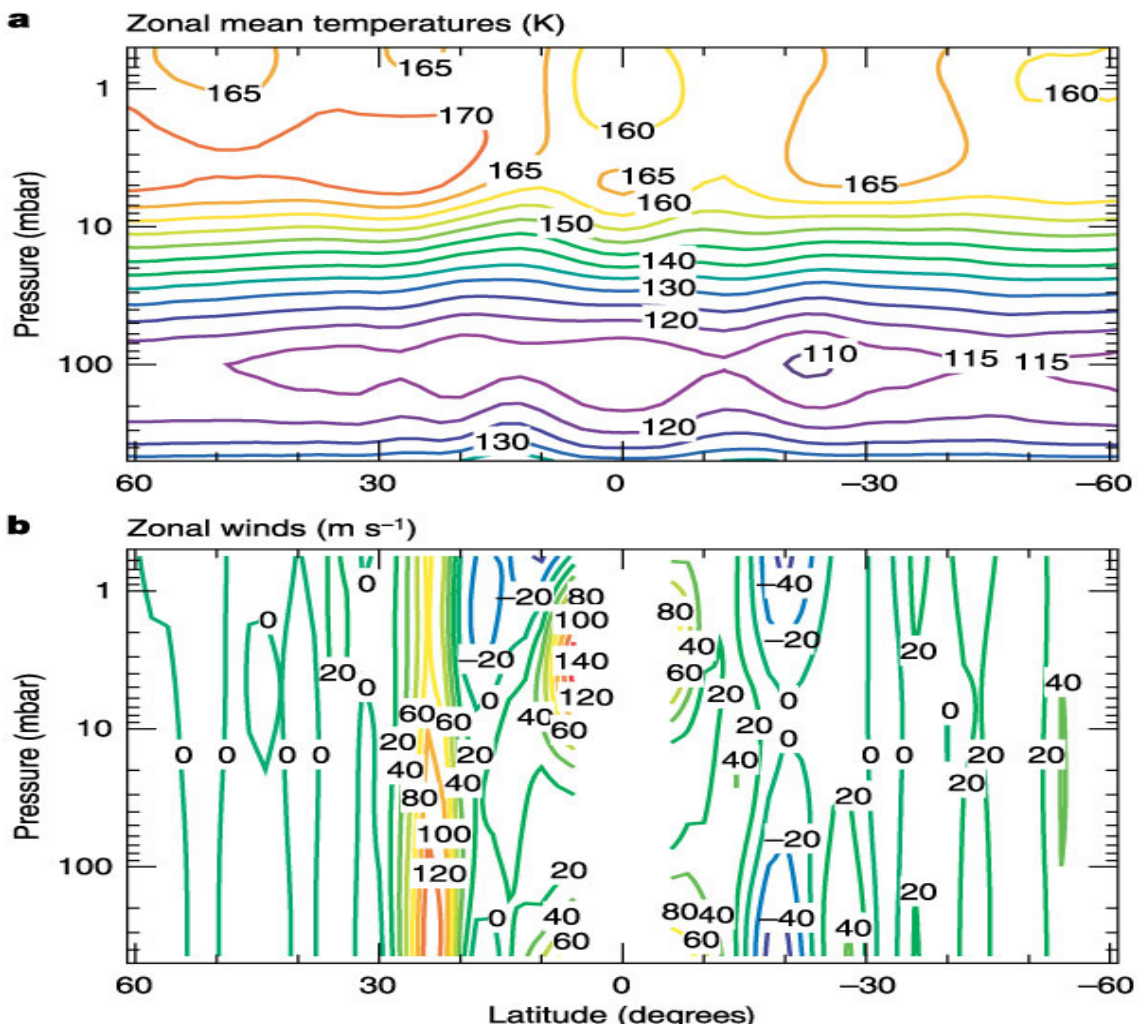


Figure 4.1: Temperatures and the computed thermal wind on Jupiter (reproduced from (Flasar et al. 2004)).

Conrath et al. (1990) calculations. In addition, Fletcher et al. (2010) found that the cooling rate of the Jovian stratosphere is much higher than the typical radiative relaxation time derived from earlier radiative calculations. Considering these uncertainties, utilizing an order of magnitude shorter than that of (Conrath et al. 1990) the radiative time constant in the middle atmosphere appears to be a valid assumption for GCM modeling of the Jupiter stratosphere.

The radiative heating and cooling processes in the stratosphere of Jupiter are summarized in Figure 4.3. It can be seen that heating by absorption of Solar radiation by methane dominates, while the major cooling is produced by ethane. Comparison of the equilibrium temperature with the measurements, and the balance of radiative heating and cooling rates is presented in Figure 4.4.

It is seen that the calculated radiative equilibrium and observed temperatures are very close, and that nudging approach of using the Newtonian cooling represents a valid approximation for radiative forcing in the stratosphere. The current version of our GCM does not incorporate a sophisticated radiative scheme that includes heating and cooling

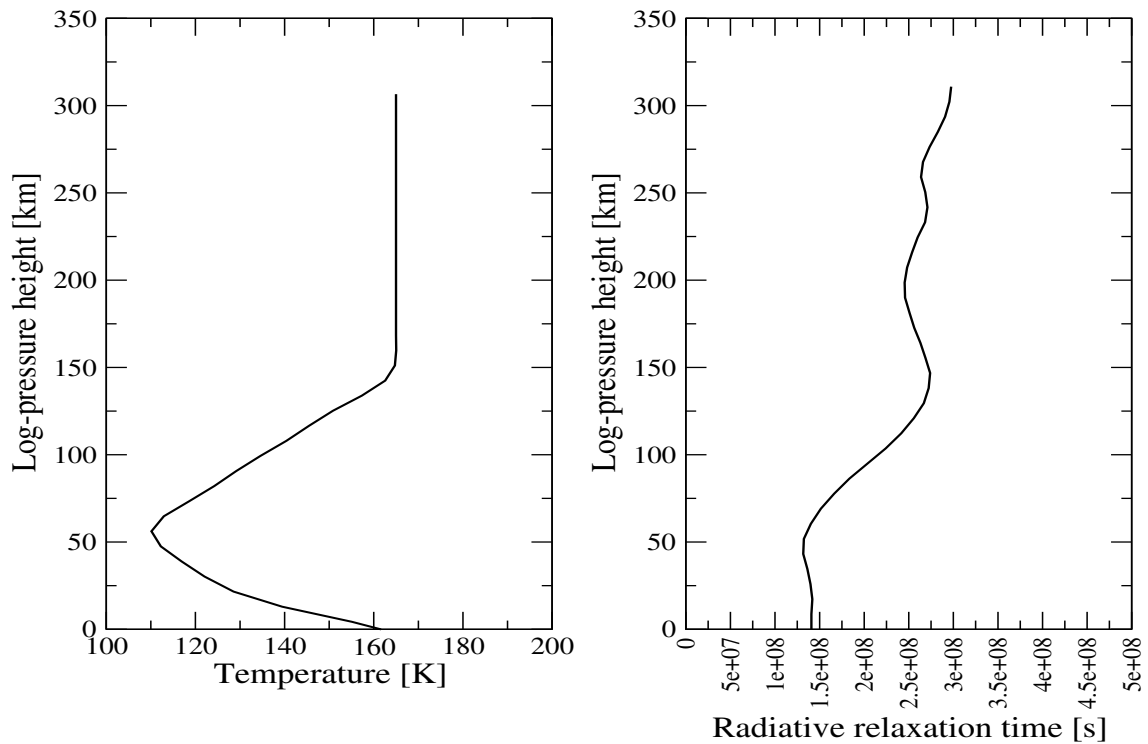


Figure 4.2: Vertical profiles of the equilibrium temperature and radiative relaxation time (an order of magnitude less) used in the simulations.

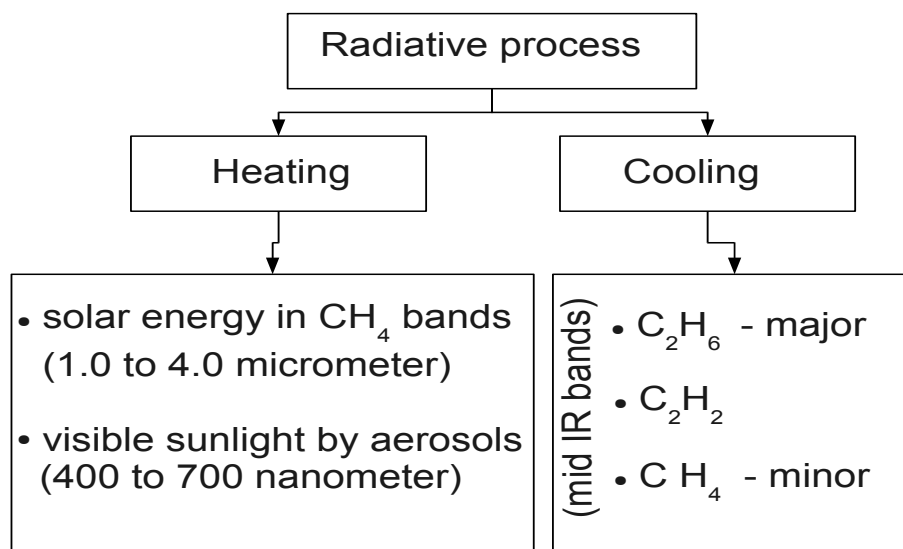


Figure 4.3: Jupiter's radiative heating and cooling due to minor atmospheric components

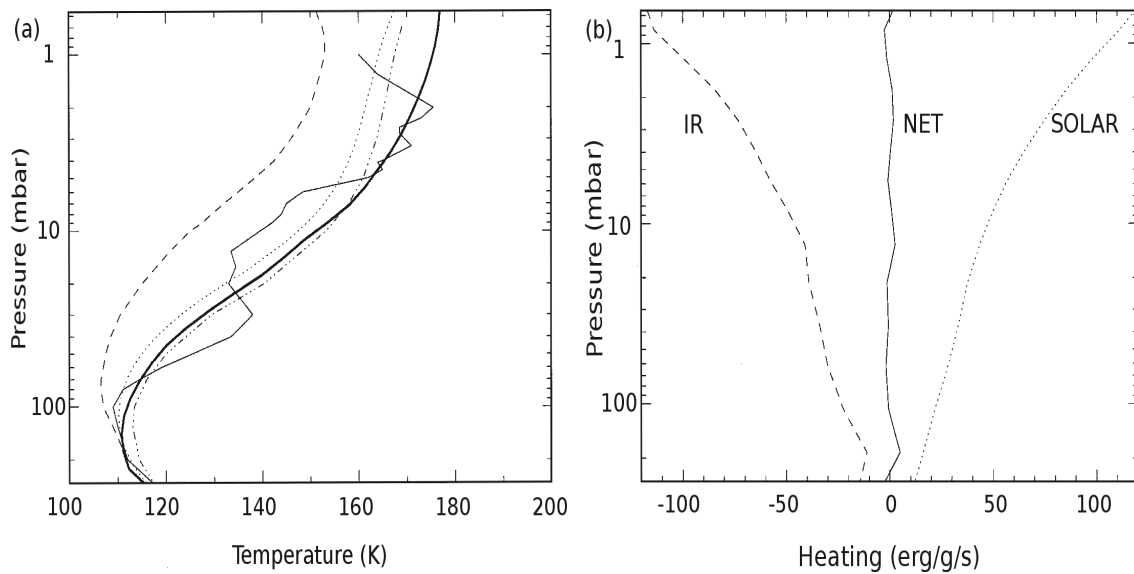


Figure 4.4: a) Horizontally averaged equilibrium temperature profile derived by Moreno and Sedano (1997) (bold solid line) compared with the Voyager 1 ingress profile (solid thin line), the thermal equilibrium profile of Conrath et al. (1990) (dashed line), the dust-free model of Appleby and Hogan (1984) (their model “b,” dotted line), and the uniform aerosol heating model of Appleby and Hogan (1984) (their model “c,” dash-multi dotted line); b) Horizontally averaged infrared cooling (dashed line) and solar heating (dotted line) profiles, and the net contribution (solid line) (adapted from Moreno and Sedano (1997)).

by aerosol and haze, therefore, simulations cannot resolve small-scale temperature features induced by spatial variations of these components. This is also consistent with the model resolution: the latter is much coarser for such small-scale features to be resolved.

4.1.3 Winds and the meridional circulation

Wind speeds in the Jovian atmosphere are usually retrieved with image processing techniques like automated or manual pattern tracking (Porco et al. 2003, Li et al. 2006c). Alternating zone and belt bands in the troposphere are well mapped using visible cloud features as a proxy for winds (Vincent et al. 2000), and show variations over time. Long-term variability of Jupiter’s winds was also studied with Hubble Space Telescope observations (Simon-Miller and Gierasch 2010). Another method is to deduce wind velocities from temperature fields using the thermal wind relation (Flasar et al. 2004) (see Equation. 4.1). This method is particularly useful for the middle atmosphere of gas giants, where the temperature maps are available for a wide latitude range. Currently it is the only method by which the vertical structure of zonal winds can be estimated in the Jovian middle atmosphere. The method, however, fails in low latitudes, because the Coriolis force tends to zero at the equator. A detailed study of the Jupiter’s cloud bands and weather systems can be seen in Simon-Miller et al. (2001) and changes in Jupiter’s observed zonal wind pattern in Pérez-Hoyos et al. (2012).

As described in Subsection 1.3.1, there are different theories of how Jupiter’s zonal

winds are generated. For example, simulation study by Schneider and Liu (2009) found that the off-equatorial jets are driven by differential solar heating, while the equatorial prograde jet is forced by the interior convective forcing. Conversely, zonal wind simulations of Chan and Mayr (2008) with a shallow convection model, which did not take account of solar irradiation, generated zonal winds with a prograde equatorial jet. The Galileo probe and moist convection modeling by Sánchez-Lavega et al. (2008) showed that the jets do not decay with depth, and extend well below the level of solar heating. According to Flasar and Gierasch (1986) and Yamazaki et al. (2004), zonal winds decay with height above the cloud level on giant planets. These results provide an additional argumentation in favor of our approach to use observed zonal winds as the lower boundary condition. The observed zonal wind utilized in our simulations is shown in Figure 4.5. The equatorial wind patterns in the middle atmosphere are less known, but appears to be very complex. Thus, Flasar et al. (2004) found in the stratosphere zonal jets with speeds of up to 140 m s^{-1} . The dynamical behavior of Jovian tropospheric winds is discussed in detail by Seiff (2000).

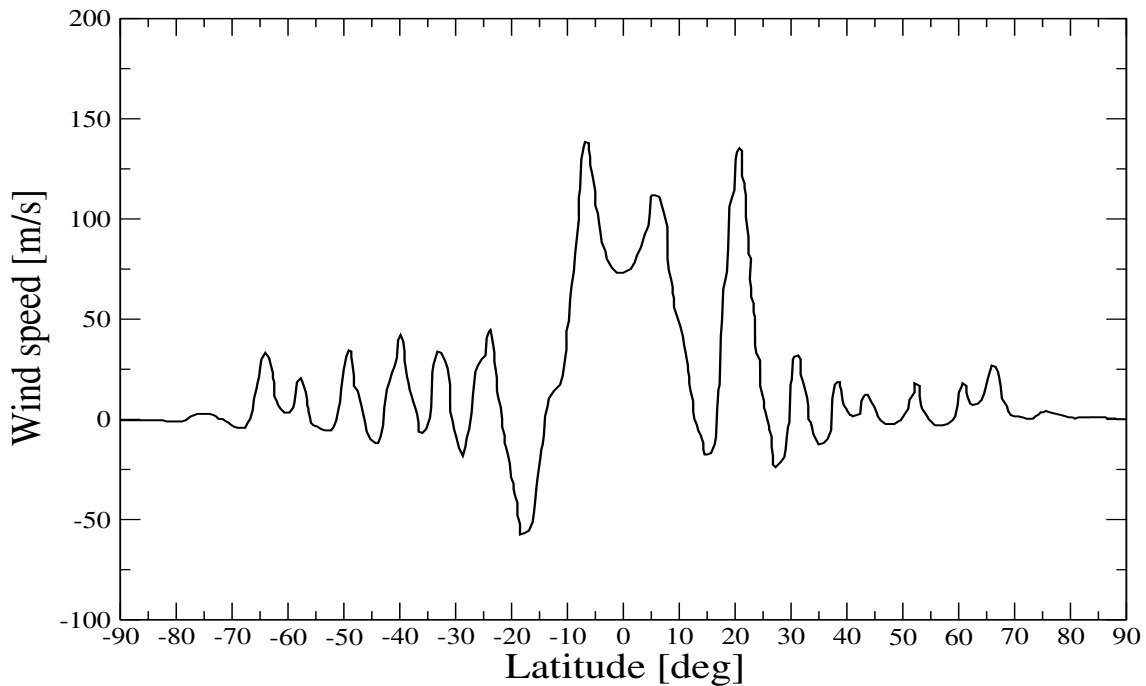


Figure 4.5: Distribution of the zonal mean wind used for nudging the model at the lower boundary of the model.

The meridional circulation is significantly more difficult to measure than zonal winds. Therefore, it is usually derived from other atmospheric fields. The diabatic circulation is a widely used approximation of the meridional transport. In it, rising and sinking motions are associated with heating and cooling by various diabatic forces, correspondingly, while the meridional flow occurs as a result of fluid continuity. If non-zonal eddies are strong, they also contribute to the meridional circulation. The sum of the eddy-induced velocities ("the Stokes drift") and the zonally averaged meridional velocities describe the net transport of tracers, which is also called the "residual circulation". Calculations of the diabatic circulation induced by various radiative heating and cooling mechanisms have been

performed by Gierasch et al. (1986), Conrath et al. (1990), West et al. (1992), Moreno and Sedano (1997). They showed a strong sensitivity of the meridional velocities to the magnitude of heating and cooling associated with various mechanisms. The results of such estimates agree on that the meridional velocity in the middle atmosphere of Jupiter is weak. Besides that, the results remain controversial, and the meridional circulation is not fully understood. Observational data on the meridional transport, which can be used for validating the model estimates, are scarce. Conrath and Gierasch (1984) showed that the low para-hydrogen fraction in the equatorial region, and high values over the polar regions may indicate an upwelling in low latitudes, and a downwelling at the poles. Another method used for inferring the stratospheric circulation was tracing the SL9 debris as a proxy for the flow (West et al. 1995).

Eddies apparently play an important role in the global meridional transport, as the meridional circulation on Jupiter is weak, and eddies are strong (Orton et al. 1991). It was shown that non-zonal disturbances induce a meridional transport of angular momentum from regions with retrograde wind to those of prograde (Schneider and Liu 2009). The eddy-mean flow interactions can significantly alter flow patterns. A pioneering study of the eddy-induced transport was done by Beebe et al. (1980). Later, interactions between eddies and the mean flow on Jupiter were considered by Salyk et al. (2006). Correlation studies revealed that the eddies supply energy to the mean flow (Beebe et al. 1980, Ingersoll et al. 1981) with a rate of ~ 1.5 to 3.0 Wm^{-2} , which is almost 10 % of Jupiter's total emitted energy. A recent automatic feature tracking study by Salyk et al. (2006) using higher number of vectors than before confirmed this result.

The transport effects of non-zonal disturbances are often expressed in terms of diffusivity, attributing the entire effect of eddies to diffusive transport and mixing. The time scale of such diffusive transport of SL9 debris on Jupiter was estimated to be of the order of hundreds years (West et al. 1995). Calculations of Bézard et al. (2002) demonstrated that eddy diffusivity can remove carbon monoxide brought in by SL9 in about 300 years. These numbers also provide some evidences that the mean meridional transport in the stratosphere of Jupiter is weak.

4.1.4 Previous simulation studies

One of the pioneering modeling studies of Jovian winds was done by Gierasch et al. (1986) using linearized balance equations. Other important steps in developing numerical models for the Jupiter atmosphere include the works on 3-dimensional GCMs (Cho and Polvani 1996, Chan and Mayr 2008, Lian and Showman 2010, Liu and Schneider 2010), and on limited area models (Yamazaki et al. 2004). A study of the zonal jets evolution in the lower atmosphere based on the Explicit Planetary Isentropic-Coordinate (EPIC) atmospheric model (Dowling et al. 1998) have been performed by (Sayanagi et al. 2008). In the thermosphere, 3-dimensional terrestrial GCMs have been adapted for Jupiter as well (Achilleos et al. 1998). Simulations of the Jovian stratosphere, however, were limited to two-dimensional models only (e.g. Conrath et al. 1990, West et al. 1992, Moreno and Sedano 1997, Liang et al. 2005). These modeling studies have shown that there exist upwellings over the zones (warm areas) in the lower stratosphere, and subsidences over the belts (cool areas) (Gierasch et al. 1986, West et al. 1992, Moreno and Sedano 1997, Zuchowski et al. 2009b). Numerical models have also been applied to studying the quasi-

quadrennial oscillations (QOO) in the equatorial stratosphere of Jupiter. They identified that the QOO is driven by nonlinear interactions of vertically propagating atmospheric waves with the mean flow, similar to the quasi-biennial oscillations in the atmosphere of Earth (Li and Read 2000, Friedson 1999). In particular, Friedson (1999) argued that gravity waves play an important role in the QOO forcing.

4.2 GCM simulations

4.2.1 Experiments setup

The model domain in our simulations was set to cover the middle atmosphere of Jupiter from 1 bar to 10 μ bar, which corresponds to approximately 310 km vertical span approximated by 41 vertical levels. The same horizontal resolution as in the "high-res" runs for Saturn has been used: 180 \times 240 grid points in longitude and latitude, correspondingly. The time step required for maintaining the stability (≈ 3 s) was found in numerical experiments, and 12 latitudinal grid points were affected by the near-pole filter. The horizontal diffusion coefficient $K_H = 7 \times 10^6 \exp(2 \times 10^{-5}z)$ m² s⁻¹ was adopted in all the simulations to be described in this chapter. Seasonal effects are neglected, because we do not employ a sophisticated radiation scheme in the current version of the model. This approximation is partially justified by the fact that the axial tilt of Jupiter is small. We used the radiative relaxation time profile, $\tau_r(z)$, from (Conrath et al. 1990) (see Figure 4.2) but an order of magnitude smaller (stronger radiative forcing). This allowed us to shorten the modeling time by achieving an equalization of the numerical solutions approximately ten times faster. The model was run for over 3000 Jupiter days before the stabilized solution was achieved. Such approach was also used in earlier studies (Simon-Miller et al. 2006, Zuchowski et al. 2009b). In all other respects, the design of numerical experiments was the same as in the simulations for Saturn described in the previous chapter. Thus, the effects of interior heating and solar irradiation were parameterized by the Newtonian nudging the model instantaneous temperature to the observed equilibrium profile (see Figure 4.2) with the relaxation time τ_r . Such approach still allows thermal anomalies to develop.

Figures 4.6 and 4.7 present the ratios of the Rossby deformation radii and the grid steps in x and y directions, respectively. The values have been derived from (3.3) using $N \approx 0.02$ s⁻¹. Similar to the analysis for Saturn, values smaller than 2 indicate the regions not properly resolving the scales, at which baroclinic eddies develop. A comparison of Figures 4.6 and 4.7 with Figures 3.13 and 3.14 clearly illustrates that the resolution 180 \times 240 allows to appropriately simulate the Jupiter atmosphere only in the low-latitude belt $\pm 30^\circ$, and that the GCM requires higher resolution than for Saturn. The existing computer capacities did not allow us to significantly increase the resolution in the runs to be reported, however, they are planned in the nearest future.

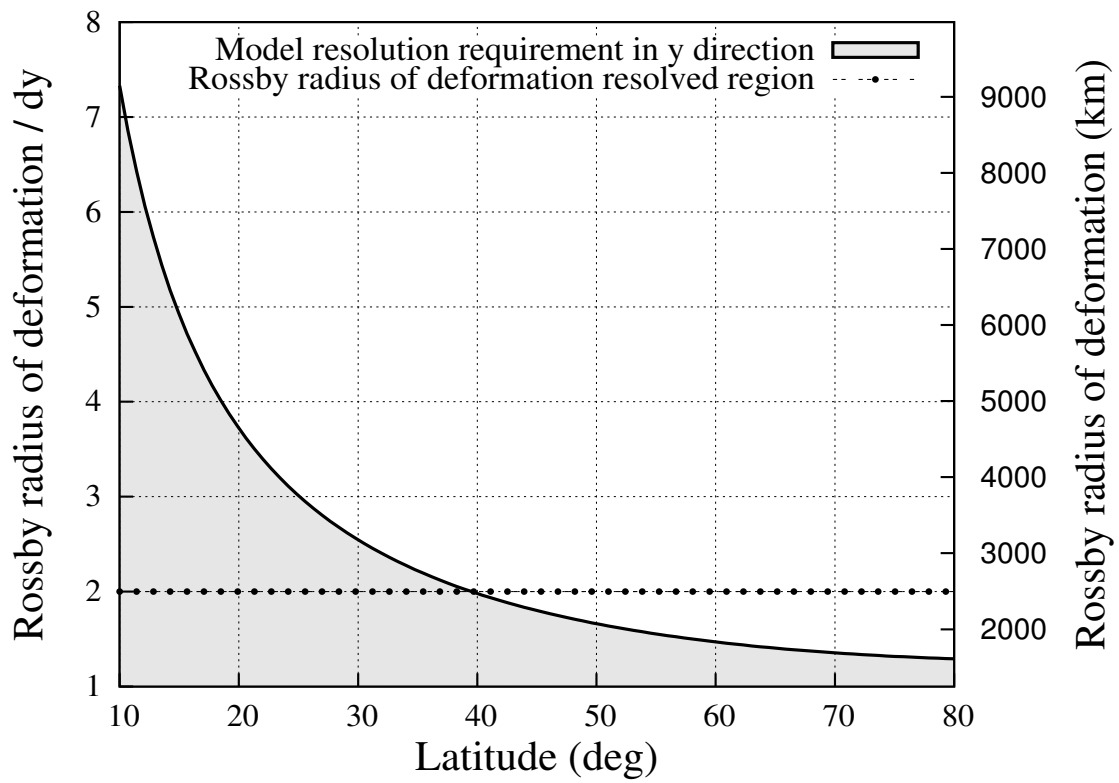


Figure 4.6: Ratio of Rossby radius of deformation and grid length in the latitudinal direction for the “high-resolution GCM setup”.

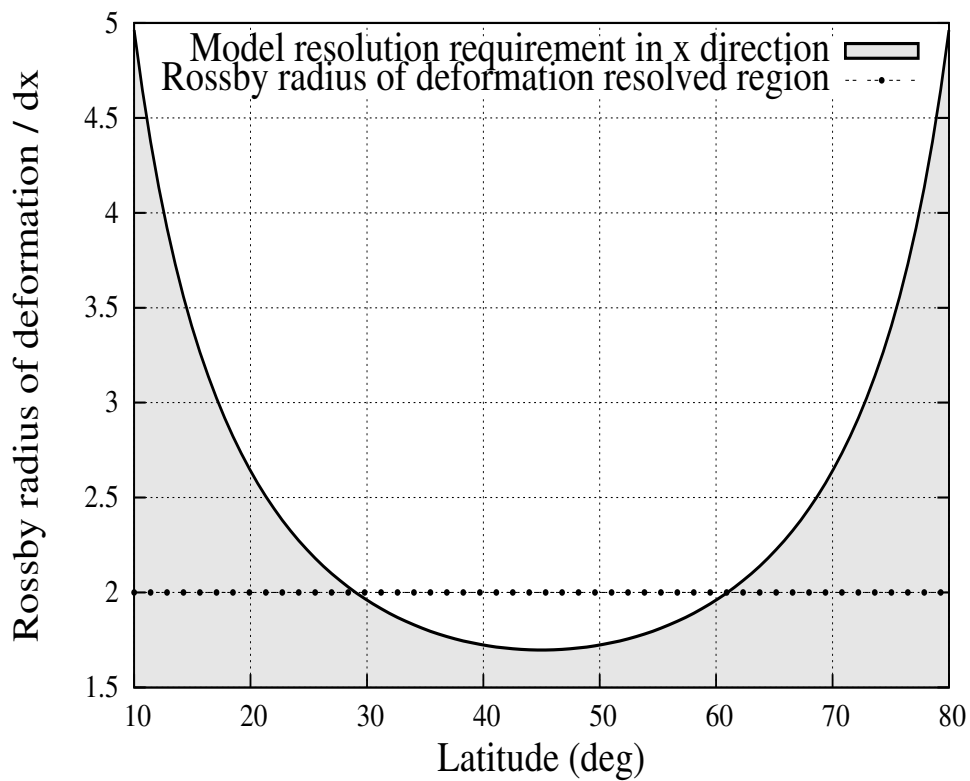


Figure 4.7: The same as in Figure 4.6, but in the meridional direction.

4.2.2 Global circulation

A global view on the simulated fields in the lower stratosphere is given by Figure 4.8, which presents the snapshots of temperature and zonal wind. It is seen that, while the belt and zone extensions are reproduced everywhere, the eddies are resolved only in the tropics. Comparison of Figure 4.8b with the counterpart for Saturn (Figure 3.15) shows that non-zonal disturbances are resolved in a somewhat narrower latitude range for Jupiter under the same resolution.

More clearly the latitudinal variations of temperature at and above the tropopause (≈ 110 K) are seen in Figure 4.9. They are the results of vertical extensions of the meridional circulation cells associated with the imposed zonal wind at the lower boundary. These latitudinal variations have close resemblance with the observed temperature features (Figure 4.1). Another view on the temperature field is given by the latitude-longitude cross-section at 60 mb in Figure 4.10. In particular, it is seen that, among the simulated eddies of various scales in the equatorial region, the disturbances with the wavenumber $s = 6$ dominate. Similar to the Saturn simulations, the planetary potential displays latitudinal variations, which are projections of the zonal wind pattern in the lower portion of the model domain (Figure 4.11a). The mean zonal wind itself is plotted in Figure 4.11b. It demonstrates the prograde jet in the equatorial region with the magnitude decreasing with height. Higher in the stratosphere, the latitudinally alternating jets significantly weaken, and two retrograde jets on the both sides of the prograde equatorial jet form. This is similar to the zonal wind pattern derived by using the thermal wind equation (Figure 4.1b). Similar patterns have been found in the observations of Greathouse et al. (2005). The prograde equatorial zonal jet on Jupiter decreases less rapidly with height than on Saturn. Previous modeling studies also indicated a vertical decay of the zonal wind (Conrath et al. 1990, Yamazaki et al. 2004). The meridional wind plotted in Figure 4.1c shows alternating directions, which reflect the multiple circulation cells in the lower stratosphere. The number of the simulated cells is determined by the number of imposed belts and bands at the lower boundary, and is larger than that on Saturn.

The simulated vertical velocity patterns are similar to those on Saturn, with higher values below ~ 300 mb and very low values above that pressure level (Figure 4.11d). The latitude-longitude cross-section of the deviations of the meridional wind from the zonal mean values (Figure 4.11e), and zonal wind at 60 mb (Figure 4.11f) show that the eddies are resolved in the equatorial region within the band of $\pm 30^\circ$. Another view is given by the polar stereographic projections plots (Figure 4.17). A comparison of the observed north polar wind patterns plotted in Figure 4.16b with the simulations in Figure 4.17 provides some evidences that the model reproduces the observed eddy patterns. Observations of the northern Jovian stratosphere in UV (258 nm) given in Figure 4.16a show that waves and a large dark oval exist at higher latitudes ($> 60^\circ\text{N}$). This points out to a demand of much higher spatial resolution for the Jupiter GCM.

The residual mean circulation is an approximation of the transport circulation, and is defined as the sum of the Eulerian mean meridional transport, $\bar{\psi}$, and the eddy-induced Stokes drift. The stream function of the residual circulation has the form (Andrews et al. 1987):

$$\bar{\Psi} = \bar{\psi} + \overline{v'\theta'}/\bar{\theta}_z, \quad (4.1)$$

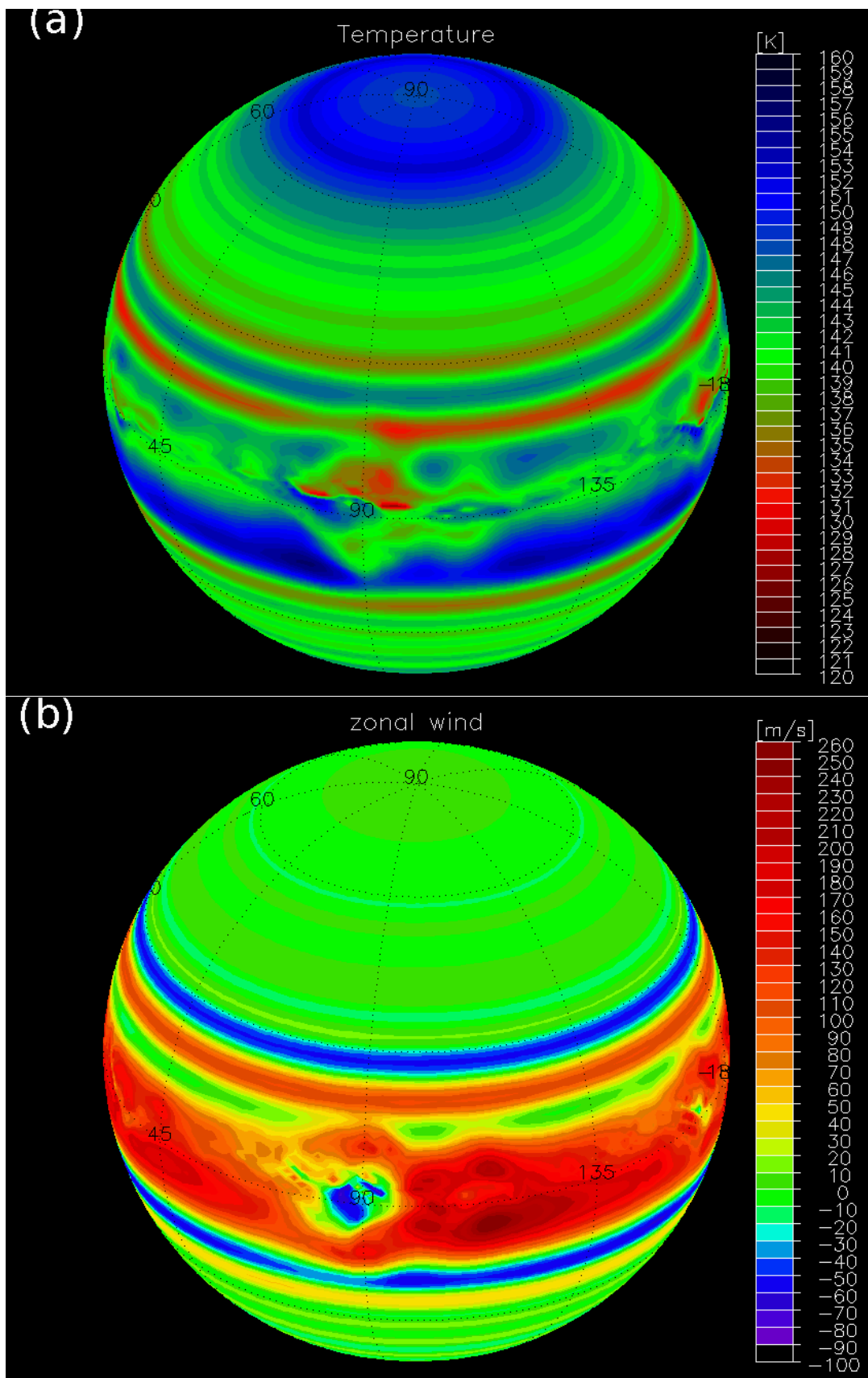


Figure 4.8: A global view on the simulated Jupiter atmosphere: a) temperature at 15 mb, and b) wind at 15 mb.

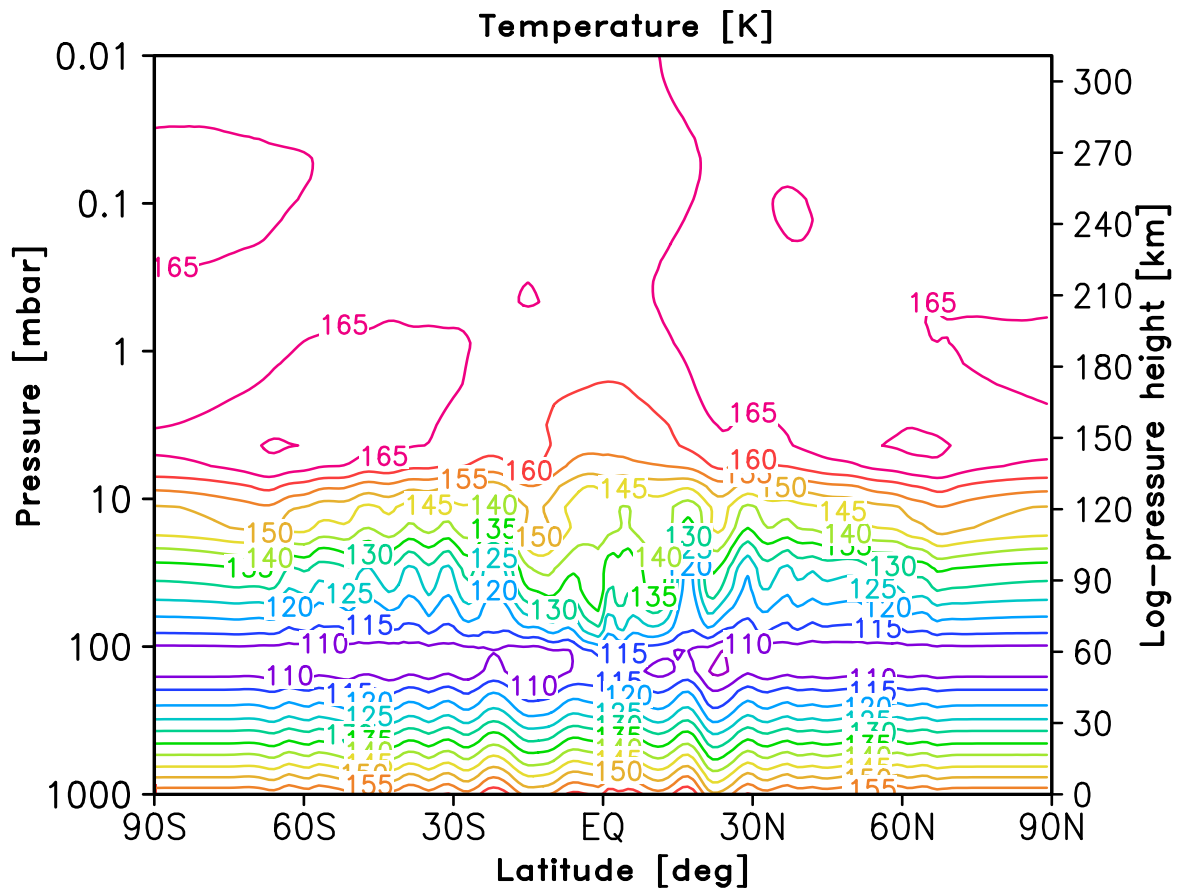


Figure 4.9: Latitude-altitude cross-section of the simulated Jovian zonal mean temperature.

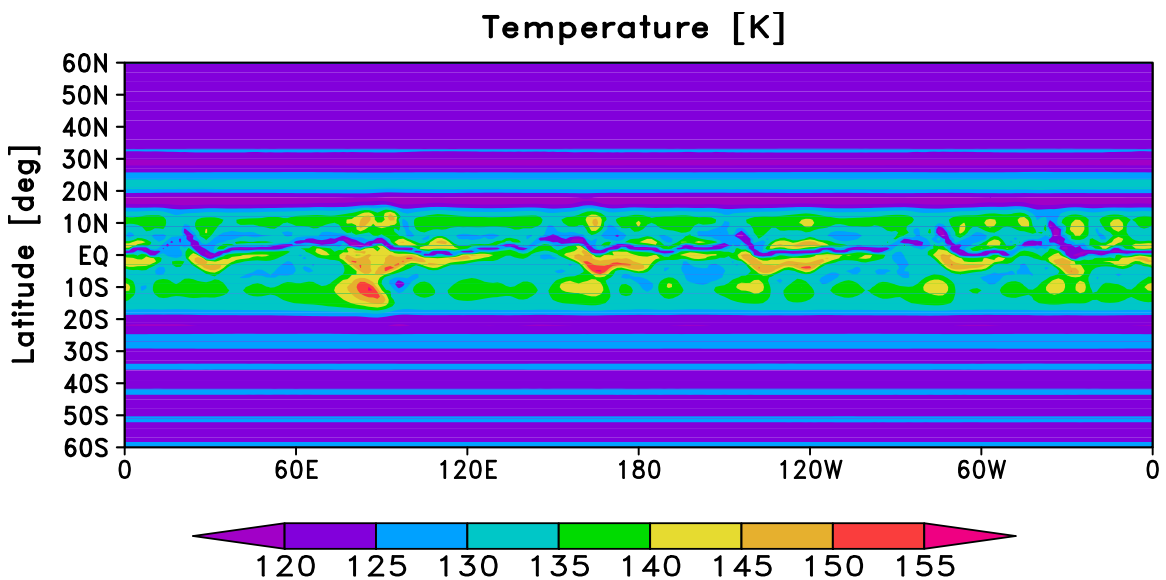


Figure 4.10: Latitude-longitude cross-section of the simulated temperature at 60 mb.

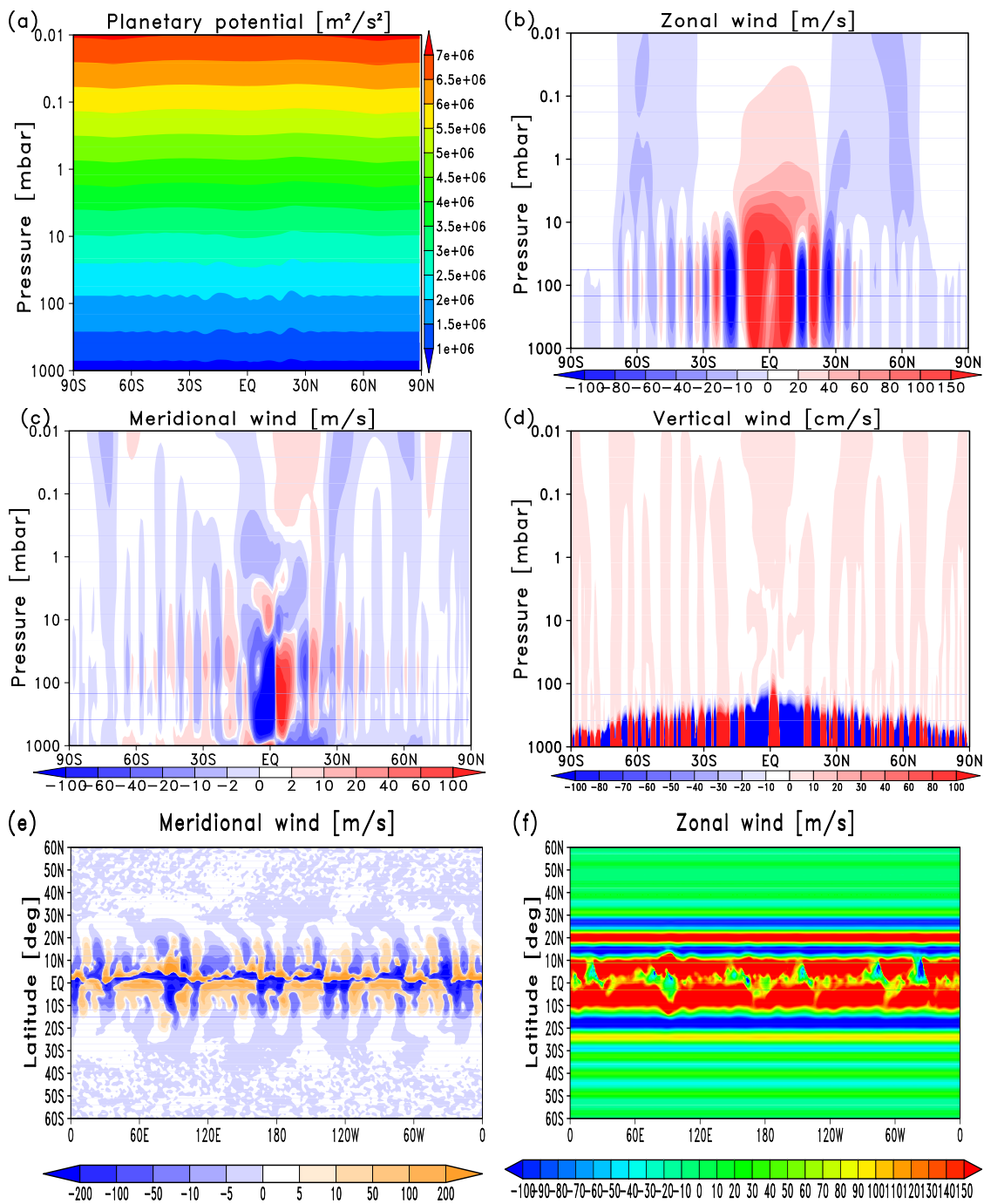


Figure 4.11: Results of simulations for Jupiter: a) zonal mean planetary potential ($\text{m}^2 \text{s}^{-2}$), b) zonal mean zonal wind (m s^{-1}), c) zonal mean meridional wind (m s^{-1}), d) zonal mean vertical wind (cm s^{-1}), e) latitude-longitude cross-section of the deviations of the meridional wind from the zonal mean values at 60 mb, and f) latitude-longitude cross-section of zonal wind at 60 mb.

where θ is the potential temperature, bars and primes denote averaging over all longitudes and deviations from the mean, correspondingly. The air is transported along thus defined $\bar{\Psi}$ such that higher values of the streamfunction are on the right.

The calculated residual circulation is presented in Figure 4.12 with streamlines (contours), and the vertical velocity (color shades). The residual vertical velocity \bar{w}^* was calculated from 4.1 using $\bar{w}^* = (\rho \cos\alpha)^{-1} \partial\bar{\Psi}/\partial y$. It shows a weak poleward transport in the entire domain with upwelling in the equatorial region. The structure of the circulation in low latitudes is very complex. It consists of many alternating cells with very strong vertical velocities (from -0.3 to 0.7 m s⁻¹). Outside the equatorial region, the model predicts circulation resembling that of Conrath et al. (1990) at lower levels, and of West et al. (1992) at higher altitudes. The GCM-produced vertical residual velocity which agrees well with estimates based on observations of comet Shoemaker–Levy 9 (SL9) dust migration between 270 mb and ~ 1 mb (Friedson et al. 1999). The very slow vertical transport in the upper stratosphere (~ 200 mb to 1 mb) was also calculated by Moreno and Sedano (1997).

The atmospheric composition study by the Cassini mission (Kunde et al. 2004) derived stratospheric abundances of hydrocarbons (like C₂H₂ and C₂H₆, etc), which represent a good tracer for the meridional transport. The existing observations show different circulation regimes in the stratosphere. For example, the object's impact in 2009 produced a meridionally localized plume, which extended longitudinally to 180° within few months (Sánchez-Lavega et al. 2011). This clearly is a direct effect of dynamics. Other evidences of the transport on Jupiter include clearing of aerosols about 100 mb, and the presence of tropospheric clouds in the northern equatorial zone at altitudes higher than over the equator (Banfield et al. 1998). There is also a detected asymmetry in polar hazes, which are confined in the polar regions. More observational data is required to validate the model results.

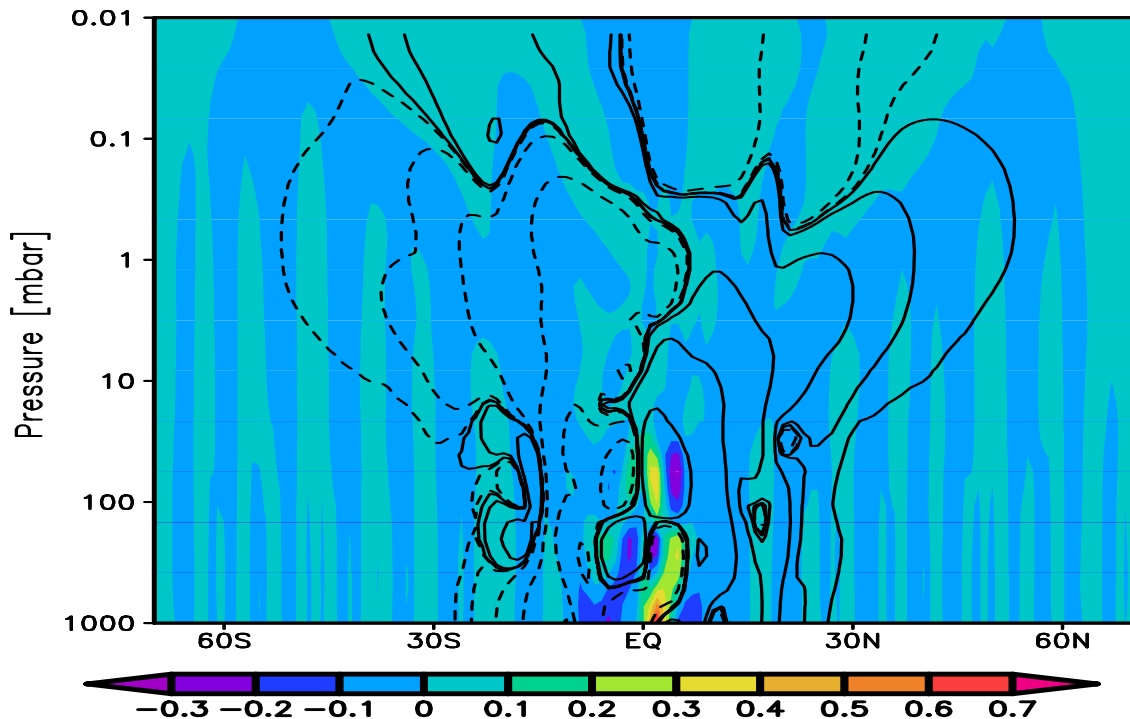


Figure 4.12: The calculated residual meridional circulation (contours), and residual vertical velocity (shaded).

4.2.3 Waves and non-zonal eddies

As was shown in the previous section, the GCM reproduces a broad range of non-zonal disturbances, at least in low latitudes. It was argued that increasing the model resolution will likely produce more eddies at higher latitudes. Here we discuss the simulated waves in more detail. One of the observed features of the flow at the cloud top level on Jupiter is the presence of so-called “chevrons”. These streaks of clouds reflect the underlying wind patterns. The horizontal structure of “chevrons” is well documented, and an example is illustrated in Figure 4.13. The flow can be represented in the form of streamlines, which are the lines made by the tangents to the fluid velocity. They characterize the flow at a given instant. To visualize the simulated fields, we plotted in Figure 4.14 the latitude-longitude distribution of streamlines at 20 mb pressure level. It is seen that the simulated non-zonal disturbances bordering the prograde equatorial jet have a chevron-like shape. Similar to the observed ones, the simulated disturbances move in the zonal direction with speeds differing from that of the jets. To date and to the best of our knowledge, such chevron-like disturbances have been reproduced by GCMs for the first time.

Most of the current observations of non-zonal disturbances on Jupiter are limited to horizontal coverage only, while the vertical structure of waves remains unknown. In order to illustrate the vertical structure of the simulated waves, a series of height-longitude cross-sections for temperature was plotted in Figure 4.15. They cover altitudes from 100 to 10 mb, and are shown for different latitudes. The abrupt disturbances are seen above the tropopause. They coincide with locations of the simulated chevrons in Figure 4.14. It is seen that disturbances/waves have barotropic structure, that is, penetrate upward to significant heights and show almost no vertical phase propagation. The magnitudes of the simulated chevron-type disturbances peak at around 20 mb. Such vertical structure is often indicative of planetary waves generated by the Kelvin-Helmholtz instability in flows with horizontal wind shears. It is also seen from Figure 4.15 that the simulated disturbances occur in low latitudes only. This could be either due to the insufficient model resolution in midlatitudes, or because the wind shear is not sufficiently strong to generate barotropic eddies. Further studies with the GCM at higher resolution will clarify this.

There are observational evidences for the existence of higher-latitude waves on Jupiter, and other unique non-zonal features like the dark oval (Porco et al. 2003), which is illustrated in Figure 4.16. For comparison, the North Polar stereographic plot of the simulated zonal wind at 15 mb is shown in Figure 4.17. It is seen that the simulated eddies resemble the observed wind patterns, at least in the equatorial region. The vertical structure of the simulated waves can be seen in more detail in Figures 4.18 and 4.19. They present the longitude-height cross-sections of the simulated non-zonal disturbances of the meridional velocity, $v' = v - \bar{v}$ (Figure 4.18), and of the zonal wind u (Figure 4.19). Both figures show two types of eddies. In low latitudes (10°S), the waves are barotropic and vertically trapped. They are apparently associated with chevrons, and confined to altitudes below ~ 5 mb. Above, the tilted isolines indicate vertically propagating planetary waves with phase velocities directed upward. Such disturbances are most often generated due to baroclinic instability associated with sharp latitudinal temperature gradients.

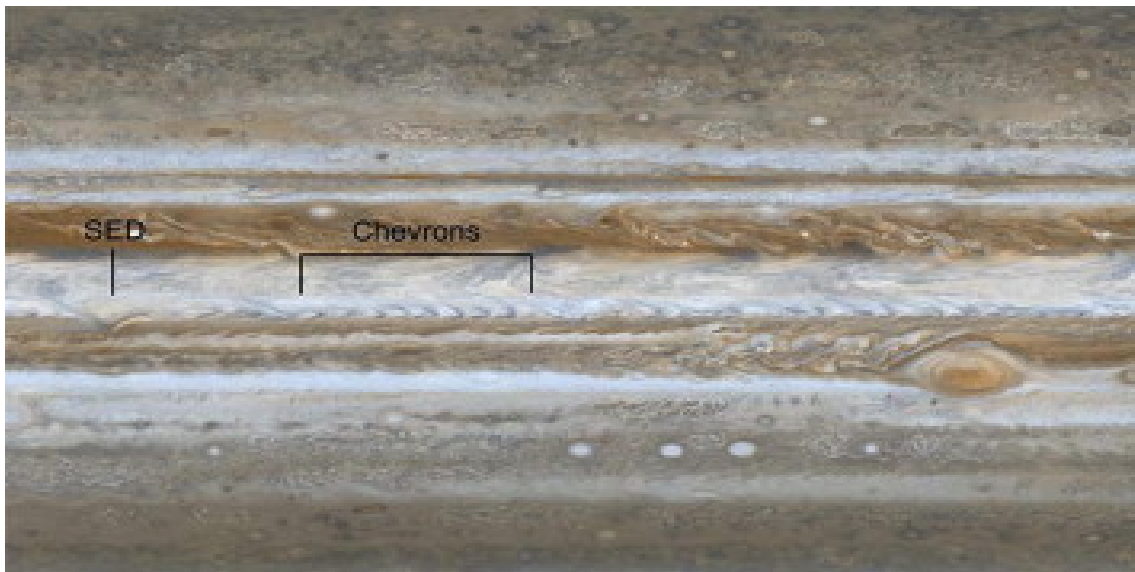


Figure 4.13: Annotated context map of Jupiter. A group of well-defined chevrons can be seen. Credit: NASA/JPL/Space Science Institute (adapted from Simon-Miller et al. (2012)).

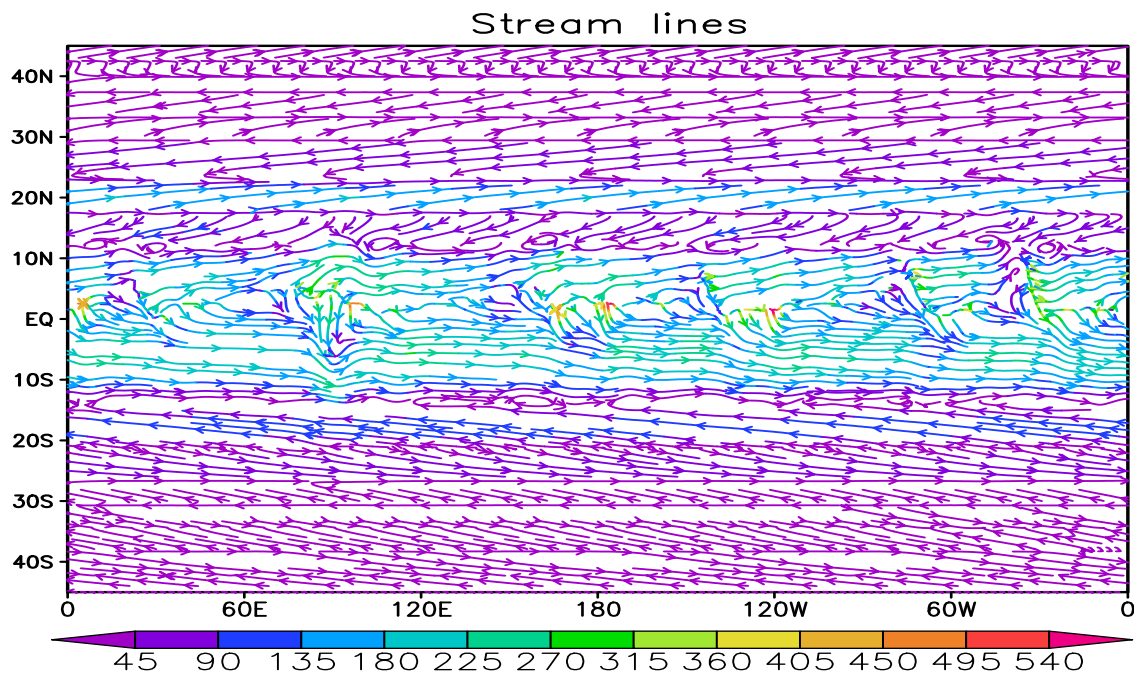


Figure 4.14: Latitude–longitude distribution of the simulated streamlines at 20 mb. Tangents to the lines indicate the instantaneous fluid velocity at that point, and the color scale indicates the magnitude of the flow.

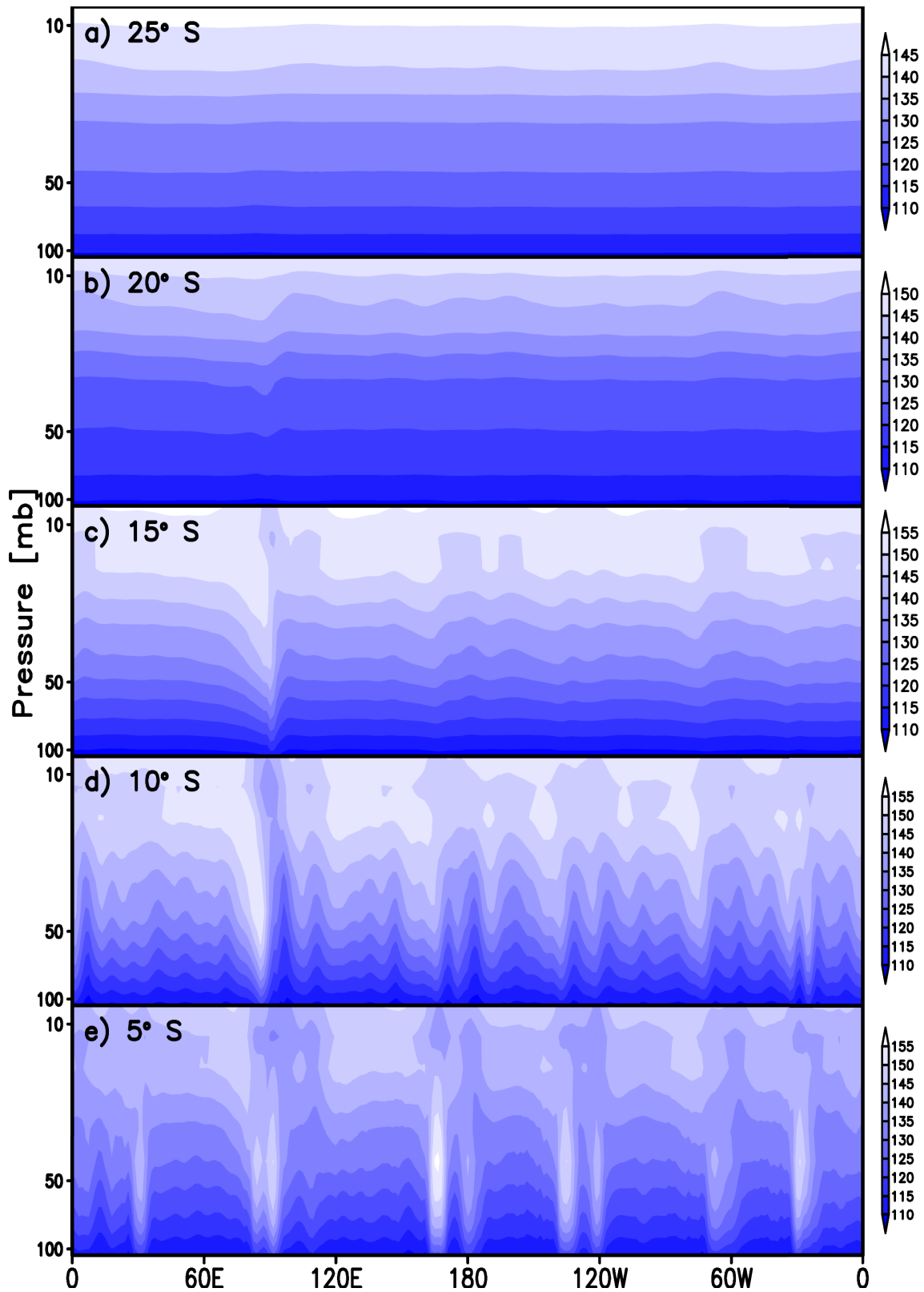


Figure 4.15: Longitude-height cross-sections of the simulated temperature illustrating the vertical structure of the chevron-like disturbances.

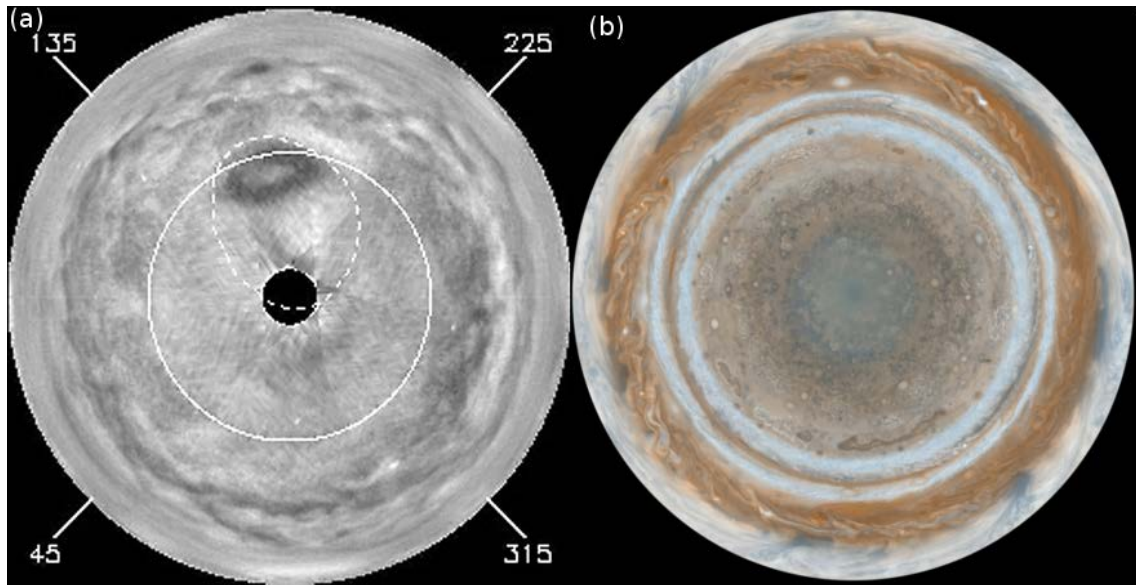


Figure 4.16: a) Waves and a large dark oval observed in the middle of its life cycle in the northern Jovian stratosphere in UV (258 nm). The zero point of System III longitude is at the bottom of the image, and longitude increases in the clockwise direction. The 60°N latitude circle is shown. The location of the main auroral oval is shown as a dashed curve (adapted from Porco et al. (2003)). b) Global color map of the North Pole, Credit: NASA/JPL/Space Science Institute

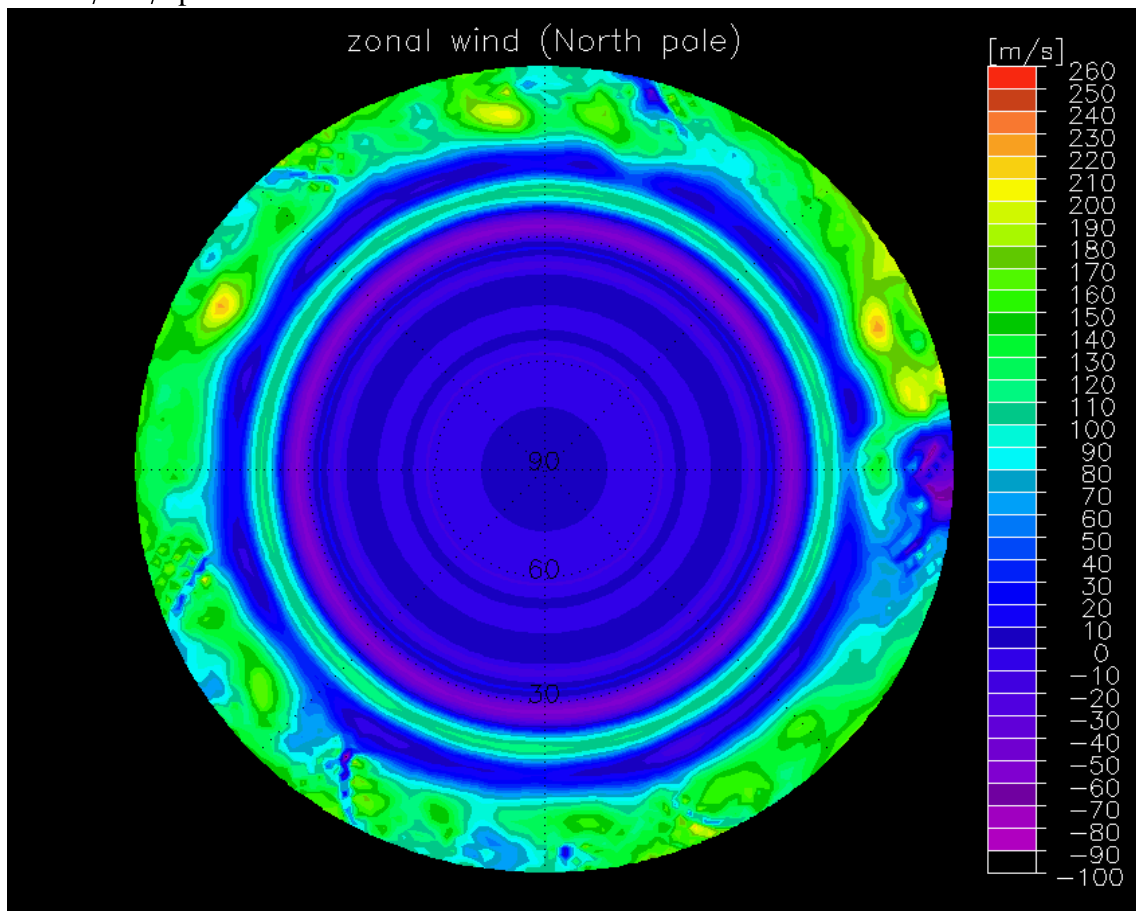


Figure 4.17: North polar stereographic plot of the simulated zonal wind at 15 mb.

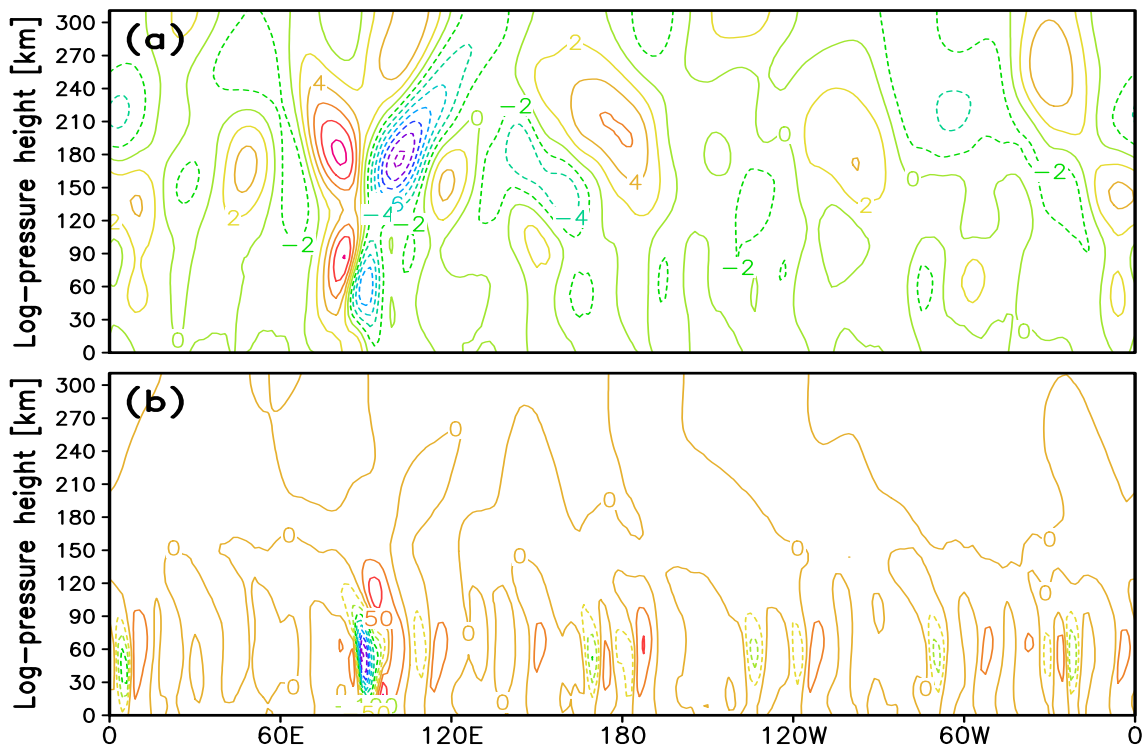


Figure 4.18: Longitude-height cross-sections of the simulated non-zonal disturbances of the meridional velocity, $v' = v - \bar{v}$ (in m s^{-1}), at (a) 20°S , and (b) 10°S .

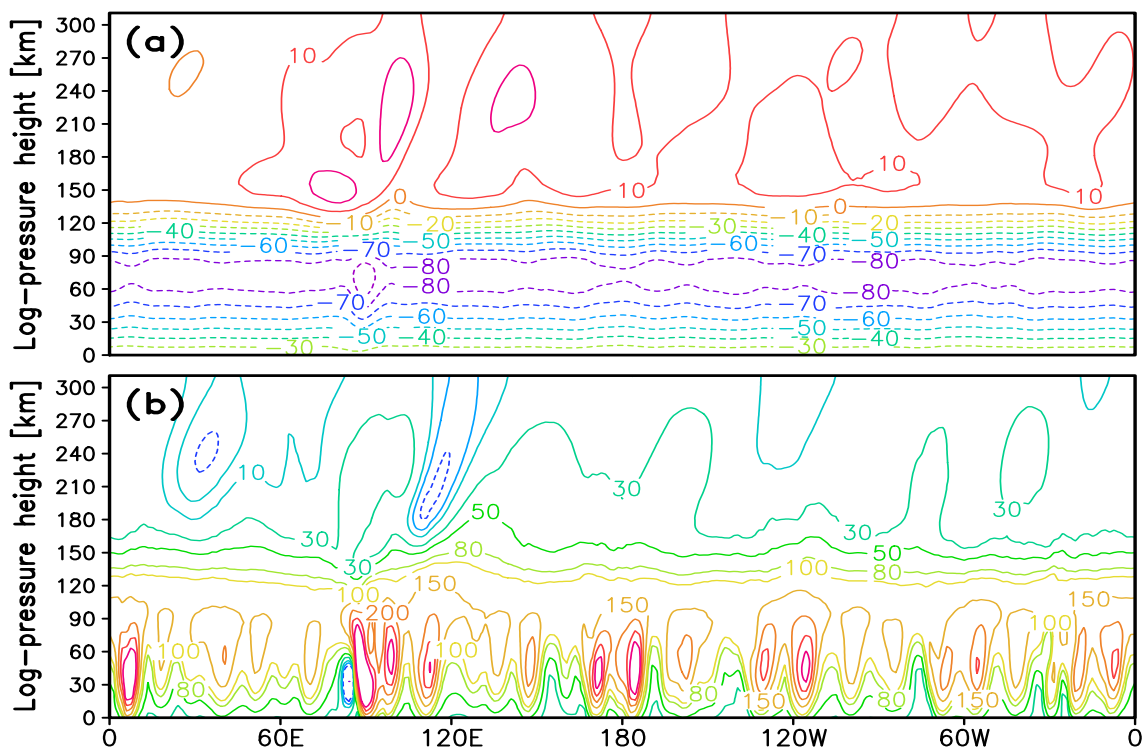


Figure 4.19: Longitude-height cross-sections of the simulated zonal wind (m s^{-1}) showing the vertical structure of waves, at (a) 20°S , and (b) 10°S .

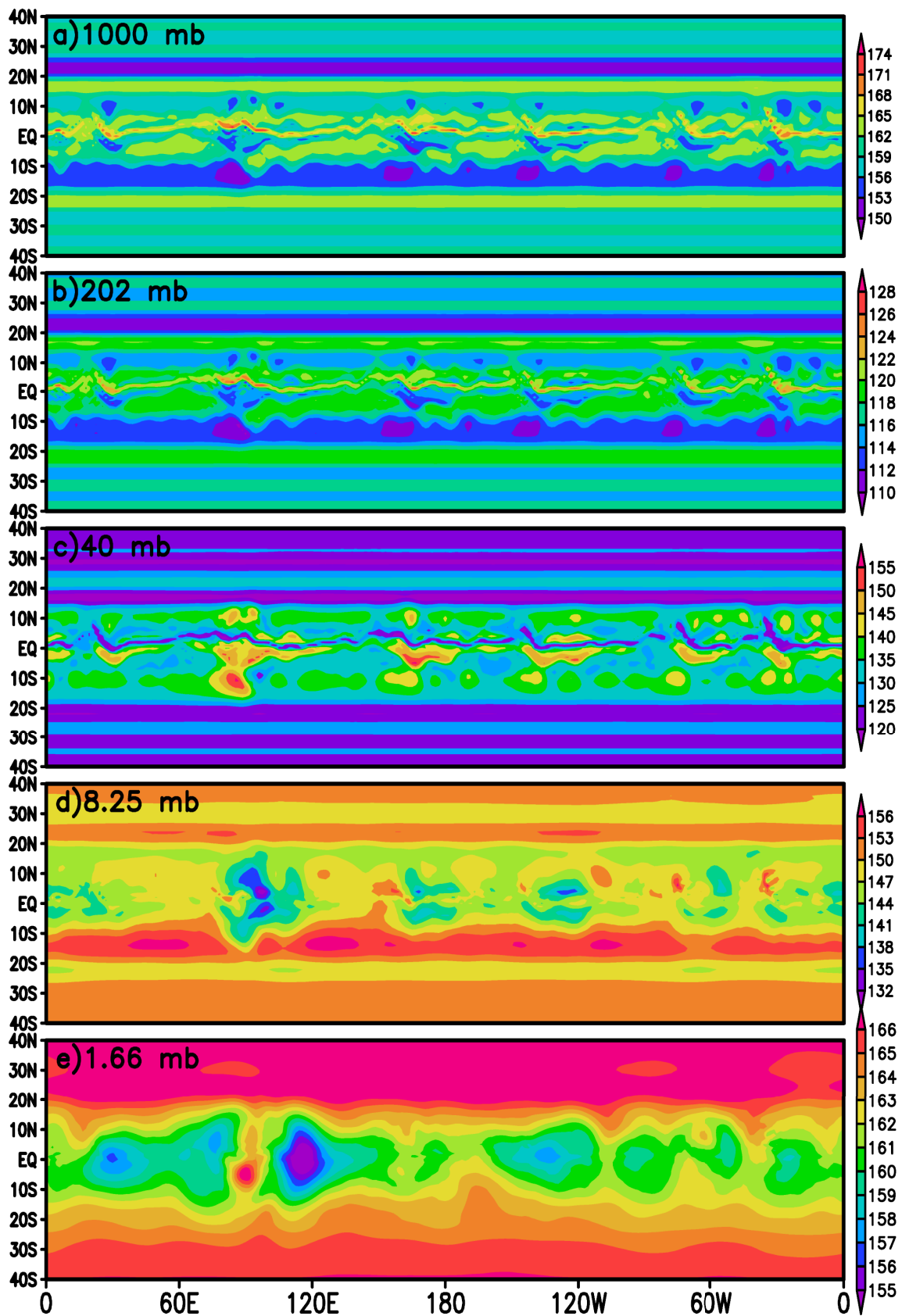


Figure 4.20: Latitude-longitude cross-sections of the simulated temperature at different levels. The hot spot-like features are visible in the upper stratosphere, and is less seen at the lower levels.

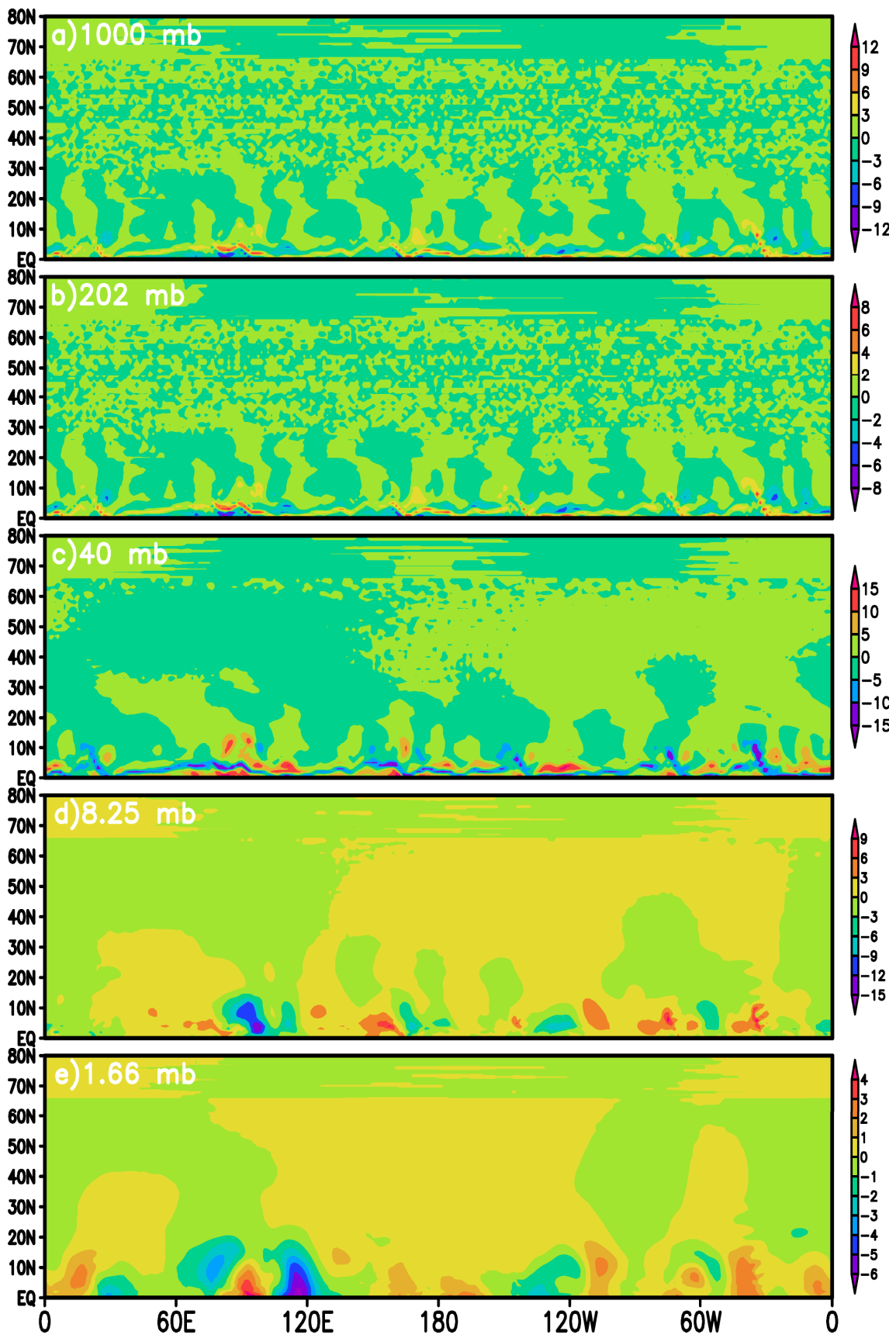


Figure 4.21: Latitude-longitude cross-section of the simulated temperature deviations from the zonal mean.

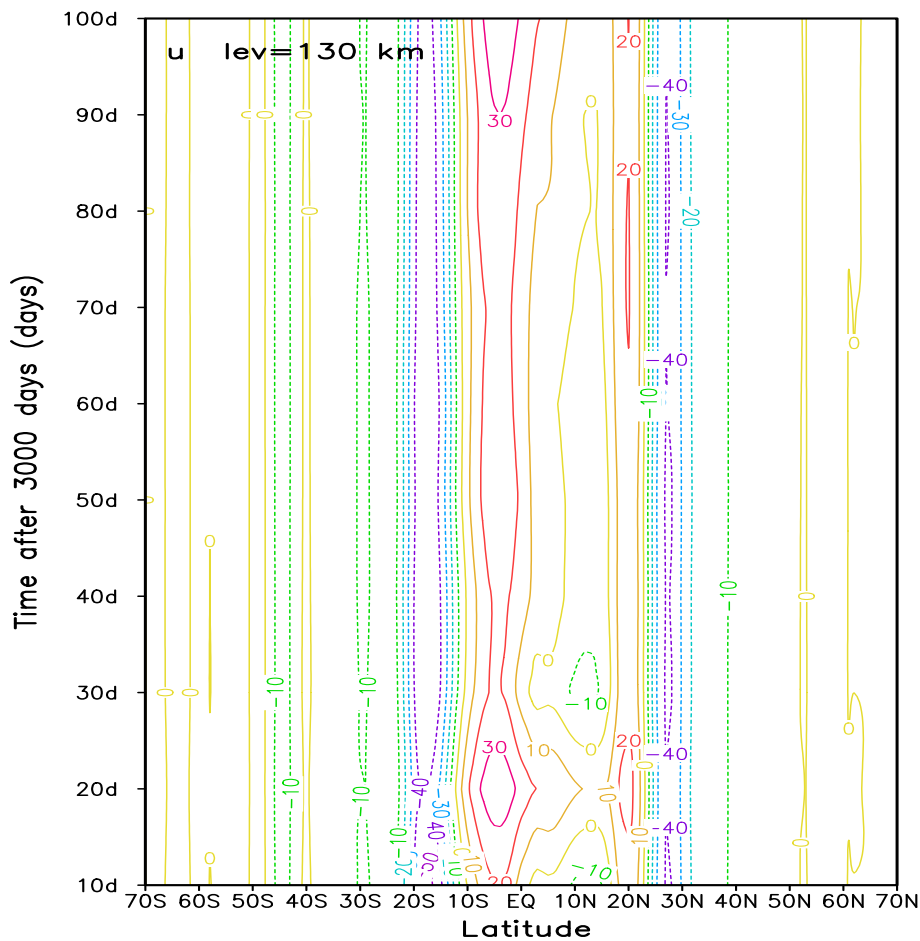


Figure 4.22: Variations of the simulated temperature with time at log-pressure height ≈ 130 km. The time period of the oscillations is close to ~ 80 Jupiter days.

The spatial structure of the equatorial and midlatitude eddies is illustrated by the latitude-longitude cross-sections of the simulated temperature and its deviations from the zonal mean at different vertical levels in Figures 4.20 and 4.21. It is clearly seen that the equatorial eddies, even though having very complex structure at lower levels, are dominated by wavenumber ~ 6 disturbance at all heights. There are observations showing the existence of longitudinal thermal waves (Deming et al. 1997), which can be seen in latitude-longitude cross-sections. It was reported by (Li et al. 2006b) that the North Equatorial Band (NEB) wave moves west with a phase velocity of 3.9 m s^{-1} , while the circumpolar wave moves eastward with a phase speed of 4.2 m s^{-1} . The estimated periods of these waves were ~ 96 and ~ 36 Jovian days, respectively, and the vertical extent is not known. In Figure 4.22, we plotted the time-latitude distribution of the simulated temperature at 130 km. It indicates that the periodicity of the simulated equatorial wave is around 80 Jovian days (33 Earth days), which is close to observations. It is also known from Cassini Image Science System (ISS) data (Li et al. 2004) that the life cycle of observed convective storms is around 9 Jovian (≈ 3.5 Earth) days, and the periodicity of vortices is about 40 Jovian (~ 16.8 Earth) days. The latitude-time diagrams in Figure 4.23 present the simulated temperature and zonal wind at 8 mb. They show the presence of equatorial disturbances with periodicities of 30 and 50 Jovian days. An in depth analysis is required to characterize the waves simulated by the GCM.

Magnitudes of non-zonal variations of simulated temperature, zonal and meridional

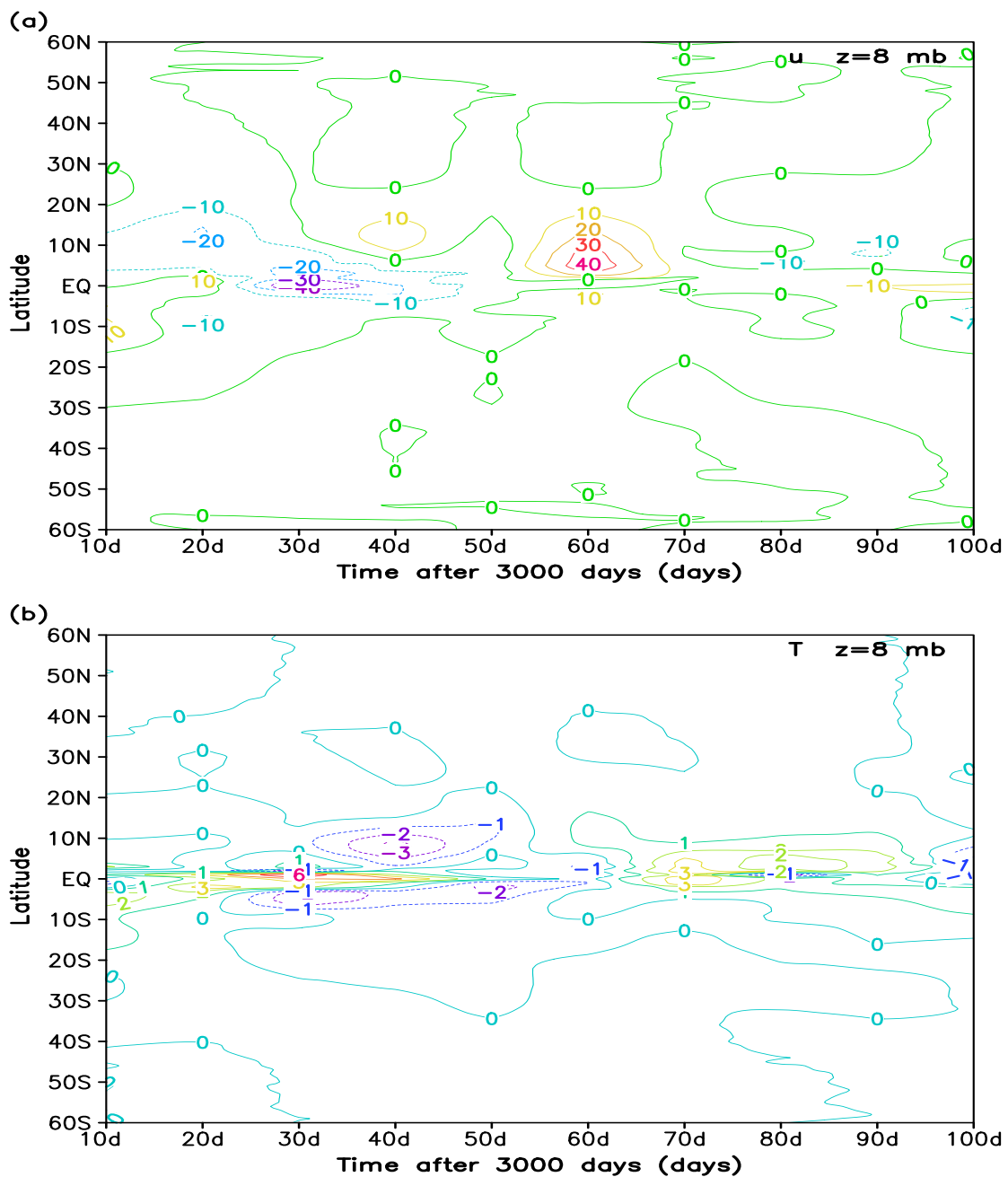


Figure 4.23: a) Equatorial oscillations of the zonal wind at 8 mb pressure level, b) oscillations of temperature at 8 mb.

wind are shown in the form of root mean square quantities in Figure 4.24. Comparison with Figure 3.19 shows a similarity of the distributions for Jupiter and Saturn. The eddies are concentrated mostly in low latitudes. The RMS temperature variations (Figure 3.19a) reach maximum around 50 mb over the equator, and abruptly decay outside the equatorial zone. The RMS fluctuations of zonal wind extend higher, and reach maximum at 100 mb level and at $\sim 5^\circ\text{N}$ (Figure 3.19b). Similar to Saturn, the vertical wind variations are confined to low latitudes and have about the same magnitude (Figure 3.19c).

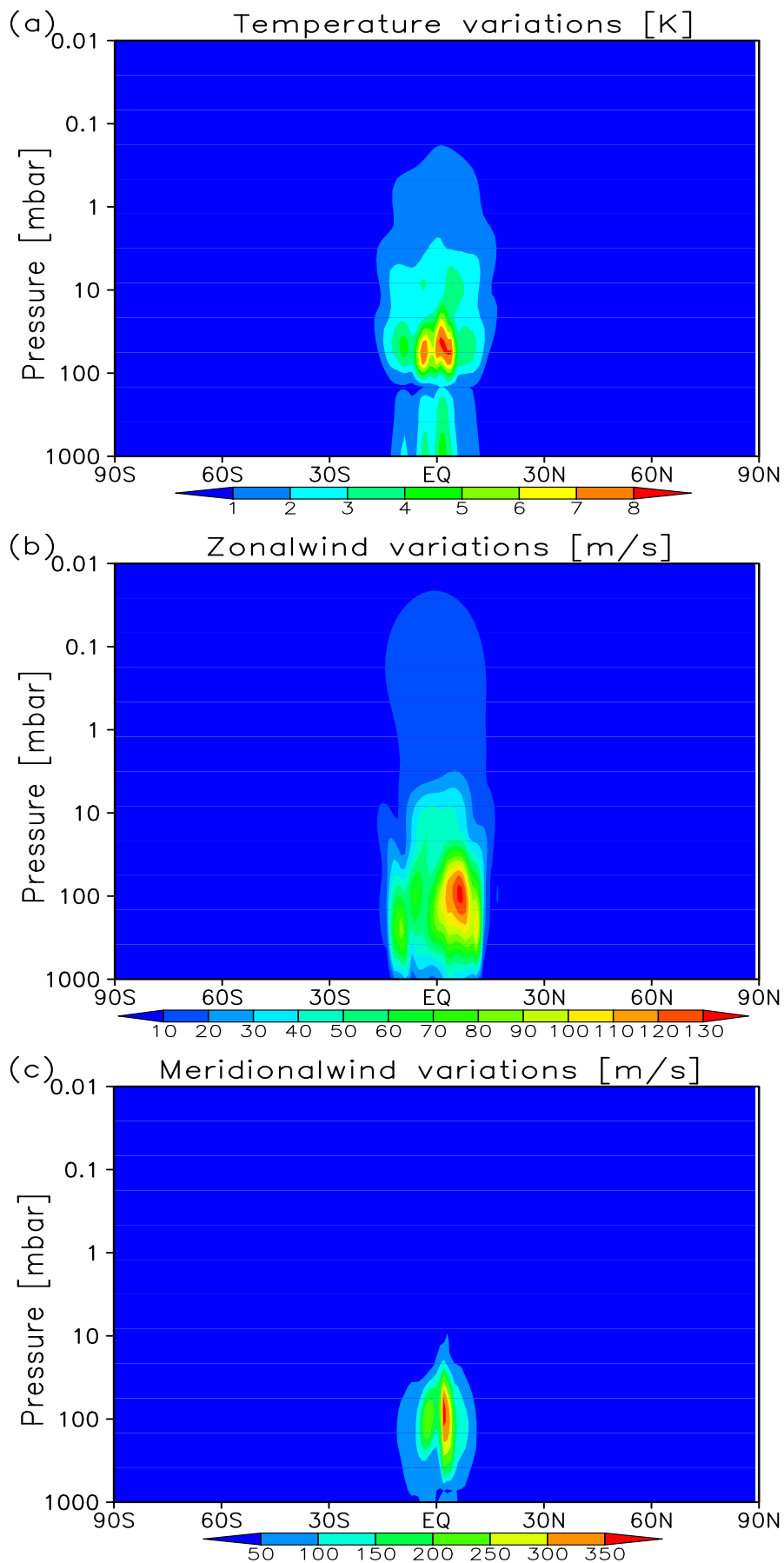


Figure 4.24: Root-mean square variations of the simulated fields: a) temperature, b) zonal wind, and c) meridional wind.

4.3 Summary of results for Jupiter stratosphere modeling

The primary purpose of this chapter was to describe the application of the developed GCM to studying the dynamical behavior of the middle atmosphere of Jupiter.

Although the “high resolution” setup, which was employed for simulations of Saturn, turned out to be less sufficient for Jupiter, the model reproduced main features of the Jovian stratosphere circulation. They include upward extension of the meridional circulation cells imposed by the zones and bands at the lower boundary. These cells decay with height, but less rapidly than on Saturn. The simulated meridional circulation is weak outside the equatorial region. The residual transport, which is the sum of the transports by zonally averaged velocities and by non-zonal eddies, consists of two cells with rising motions over the equator, poleward transport in midlatitudes, and downward flow in the polar regions. Such circulation is very similar to that on Saturn.

The GCM successfully reproduced the variety of non-zonal disturbances in the equatorial region where the resolution was sufficient to resolve the Rossby deformation radius. In particular, it reproduced for the first time the so-called “chevrons” - disturbances observed in low latitudes. Simulations revealed that they extend above the tropopause up to ~ 5 mb, vertically trapped, and have barotropic vertical structure. This provides a clear indication that the source of the “chevrons” is the Kelvin-Helmholtz instability associated with horizontal wind shears.

The GCM reproduced wave disturbances, which are in a reasonably good agreement with observations in terms of periods and phase velocities. Simulations demonstrated that besides the vertically trapped “chevrons”, vertically propagating planetary waves exist outside the equatorial region, and above ≈ 150 km. Such waves are generated due to baroclinic instability associated with sharp vertical wind shears. They are able to transport momentum high and away from their place of origin.

5 Simulation of extrasolar “warm” gas giant planets ¹

5.1 Motivation

There are large quantities of giant extra-solar planets among over 800 confirmed ones, which can qualify as “cold” and “warm” Jupiters. These are the planets with masses close or exceeding the mass of Jupiter, and which orbit their stars at distances large enough to be not gravitationally locked. Unlike the “hot” and slow-rotating Jupiters, these gas planets can maintain fast rotation, while receive more star radiation than Solar System’s Jupiter and Saturn (see figure 5.1).

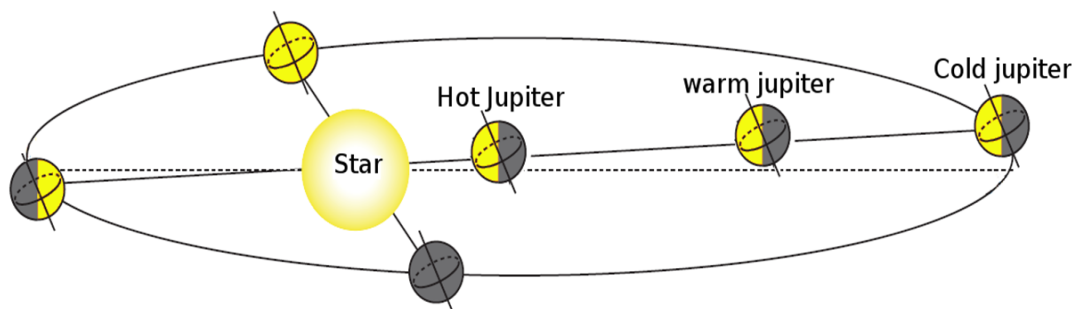


Figure 5.1: An illustration of the warm gas giants orbit

Figure 5.2 presents the known exoplanets whose parameters apparently satisfy these criteria. It is seen that there are dozens of discovered exoplanets with masses from 0.5 to 4 Jupiter’s mass, and at distances from 0.5 to 4 AU from their respective stars.

The newly developed GCM is suitable for simulating the atmospheric dynamics of such “warm” exoplanets. It has been applied to simulations of the atmospheric circulation of a Saturn-like planet under different stellar forcing scenarios. Such a generic planet is similar to the gravitationally unlocked and “warm” extrasolar planets HD 155358b and HD 96063b. The main goal of these simulations, besides testing the GCM at different regimes, was to study the changes induced by increased stellar heating, and to understand how the atmospheric circulation varies in response.

¹Major part of this chapter is a published work of the author (Medvedev et al. 2013)

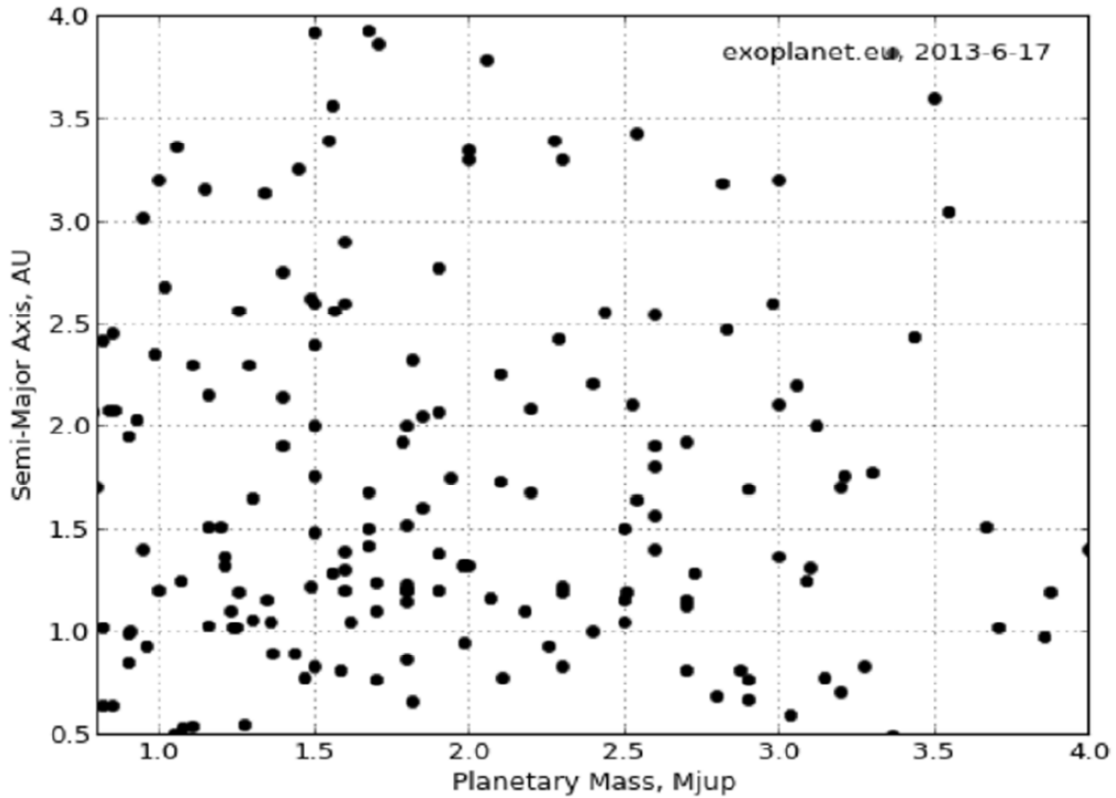


Figure 5.2: A plot showing confirmed exoplanets with less than 4 AU Semi-Major axis and planetary mass ranging from 0.5 to 4 Jupiter mass (From exoplanet.eu)

A horizontally uniform profile T_{eq} was obtained by averaging Cassini/CIRS measurements from (Fouchet et al. 2008, Fletcher et al. 2010) and the characteristic relaxation time τ_{rad} for Saturn’s stratosphere was estimated from radiative calculations of Conrath et al. (1990), as described in section 3. The weak radiative forcing implies that the model must be spun up from a windless and isothermal state for several Saturn years to establish a dynamical equilibrium. Instead, in all the simulations, we applied much stronger radiative forcing. This effectively means that the modeled planet is not a realistic Saturn, and that the simulations can be viewed as sensitivity experiments with a highly idealized Saturn-like planet. A Similar approach was taken by Zuchowski et al. (2009b), who modeled the atmosphere of Jupiter with 100 times stronger radiative forcing.

In this regard, it is important to understand how different this planet dynamically is from Saturn, and what kind of changes, stronger radiative forcing has introduced to the circulation. According to (2.5), the steady state vertical velocity scales directly with the radiative forcing, and, therefore, inversely with the characteristic radiative time. To estimate the difference caused by the imposed radiative strength, we performed simulations with $\tau_{rad} = 10^5$ and 10^6 s, that is, with radiative forcing 1000 and 100 times stronger than in real Saturn. In all simulations, the model was spun up from the windless and isothermal state with small zonal and meridional temperature disturbances introduced to break the initial state of balance. Figure 5.3 shows the one day-averaged vertical velocities after 300 days of integration. As one can see, an order of magnitude difference in τ_{rad} did not cause a proportional change of strength of the circulation (solid black lines in panels a

and b), at least outside of the equatorial zone. From the zonally and temporally averaged equation (2.5),

$$\bar{w}^* \approx -\frac{\bar{T} - T_{eq}}{\tau} \left(\frac{d\bar{T}}{dz} + \frac{\kappa\bar{T}}{H} \right)^{-1} + \text{Eddy terms}, \quad (5.1)$$

where \bar{w}^* is the residual vertical velocity, the first term in the right-hand side represents the adiabatic vertical velocity \bar{w}_a , and the second term is associated with the effects of zonally asymmetric disturbances. The corresponding \bar{w}_a are estimated and plotted with the red dashed lines in Figure 5.3a,b. They are reasonably close to \bar{w}^* , especially in the tightly radiatively controlled run ($\tau = 10^5$ s) and in mid- and high latitudes, that is, when and where eddies are weak. The corresponding ‘‘diabatic heating rates’’ (2.28) differ much less than an order of magnitude between the two cases. The shorter τ_{rad} are offset by simulated temperatures that are closer to the equilibrium (Figure 5.3c), and vice versa. Thus, although the use of stronger radiative forcing is an idealized approximation, our simulations to be presented may still be relevant to solar-system Saturn. We find also, that the above changes are of the same order of magnitude as those produced by variations of the coefficient of horizontal diffusion, the other ‘‘tunable’’ parameter of the model.

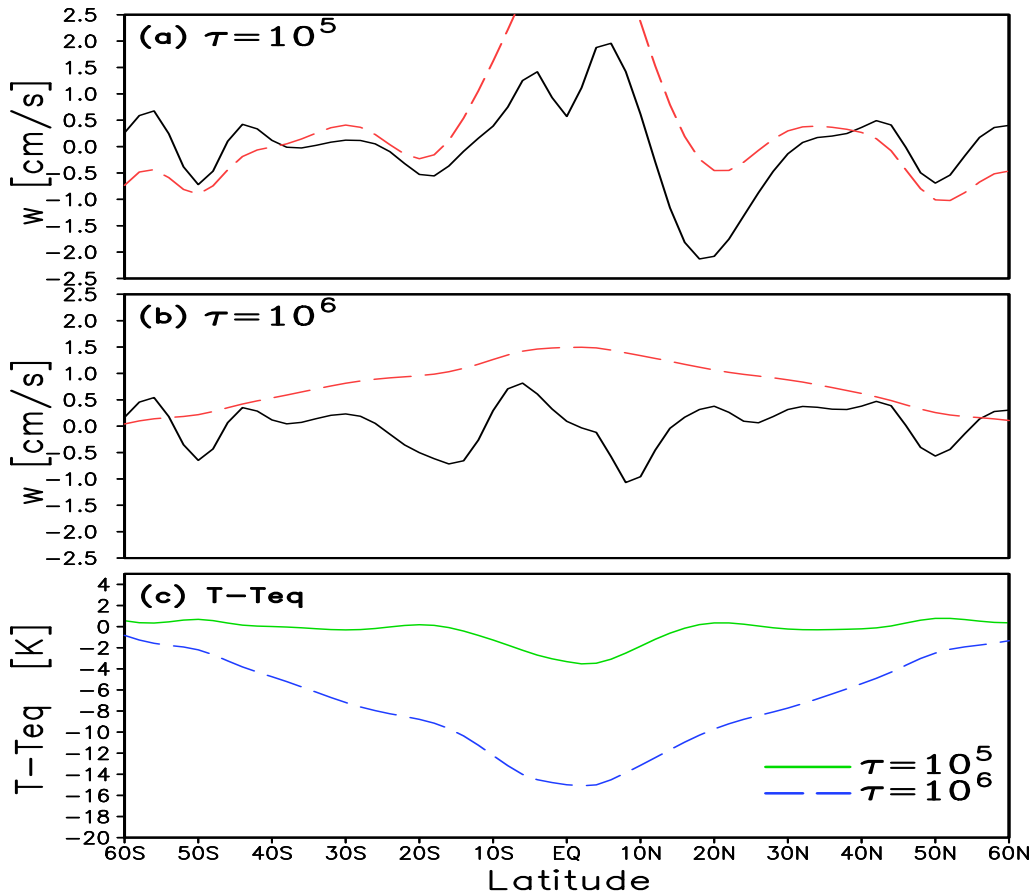


Figure 5.3: (a) and (b): Residual vertical velocities (solid lines) simulated with $\tau_{rad} = 10^5$ (upper panel) and 10^6 s (middle panel) at 430 km. The estimated adiabatic velocities are shown with dashed lines in the corresponding panels. (c): Deviations of the simulated zonal mean temperature from the prescribed equilibrium one for $\tau_{rad} = 10^5$ s (solid) and $\tau_{rad} = 10^6$ s (dashed).

5.2 Formulation of the problem and experiment setup

Atmospheric circulation of giant gas planets is driven primarily by stellar irradiation and interior heat. The latter dominates the atmospheres of outer planets in the Solar System, while the former is associated, in the first hand, with transiting extrasolar hot Jupiters. Understanding the atmospheric dynamics on such planets is still at early stages, because of the lack of observations, and the complexity of interactions between radiation and flows. There are more differences between cold and hot Jupiters that have important dynamical implications. Transiting Jupiters are gravitationally locked to the parent stars, their rotation periods are close to the orbital periods, and are much longer than on Jupiter or Saturn. Orders of magnitude higher amount of starlight received by hot Jupiters results in significantly higher atmospheric temperature, greater density scale heights, and in relative unimportance of convective forcing from the planet interior.

The commonality for both types of planets is the existence of tropospheres and stratospheres. Tropospheres are strongly affected by convection induced in interiors, and have temperatures close to adiabats. Stratospheres are more stably stratified, and therefore capable of maintaining various types of atmospheric waves, which may significantly feedback onto the mean circulation via nonlinear wave-mean flow interactions. Applying GCMs for a wide range of planetary parameters can provide an insight into mechanisms that shape the atmosphere circulation.

Besides hot Jupiter-like exoplanets, there are gas giants at intermediate conditions: when they are close to their stars to be appreciably affected by the incoming radiation, but not close enough to be gravitationally locked. Such conditions can occur, for instance, if the planet migrates closer to the star, and/or the star brightness increases. There are dozens of planets that have been detected at distances from 1 to 5 AU, and which apparently fall into this category, e.g., HD 155358b and HD 96063b, the planets with masses close to 0.9 of the mass of Jupiter.

There is a major computational problem with applying GCMs to fast rotating planets. In order to properly simulate their dynamics, the model must resolve horizontal scales smaller than the Rossby radius of deformation. From 1.1, when rotation is fast, and f is large, the Rossby radius is small. This implies that a very high spatial resolution must be used to model cold (small $H = RT/g$, where T is the characteristic temperature, and g is the acceleration of gravity) and fast rotating planets. Even higher resolution is required when a GCM is to be applied to giant planets. Then the same horizontal grid length in the atmosphere entails a smaller angle resolution for larger planetary radius, which makes the GCM excessively expensive computationally.

For hot (large H) and gravitationally locked (small f) giant exoplanets, the Rossby radius of deformation is relatively large, and, thus, application of GCMs is less demanding. Such models for hot exoplanet giants, although highly idealized compared to their terrestrial prototypes, have been extensively used to study atmospheric dynamics (e.g., Showman et al. 2008a,b, 2009, Menou and Rauscher 2009, Rauscher and Menou 2010, Showman et al. 2010, Showman and Polvani 2011, and references therein). Simulations of the “cold” solar-system Jupiter were long not feasible because of computational resources, and either two-dimensional zonally averaged models (Conrath et al. 1990, West et al. 1992), or three-dimensional semi-geostrophic models (Zuchowski et al. 2009b) were applied for investigations of its atmospheric circulation. To circumvent the computational

problem caused by high resolution, Cho et al. (2008) developed a GCM based on a shallow water formulations, and applied it to a broad range of planets from cold to hot giants. Recently, GCMs based on three-dimensional primitive equations have been introduced for the solar-system Jupiter (Yamazaki et al. 2004, Schneider and Liu 2009).

The model lower boundary is kept at 2 bar and the top of the model at 10 μ bar, with 41 equally spaced log-pressure levels. This setup is same as that of the low resolution (90×120 in latitude and longitude respectively) Saturn simulations described in chapter 3 (see 3.2.1). This horizontal resolution is the same as that of the Saturn GCM simulations done by Friedson and Moses (2012), and was chosen as a compromise between the need to resolve the Rossby radius of deformation and computational viability. The time step in all simulations was set to 5 s.

Three characteristic cases are considered here. The simulations begin from a cold giant planet in many respects similar to the solar-system Saturn, which is driven exclusively from the interior. In Section 5.3.2, the model setup is modified to account for the meridional temperature gradient in the troposphere produced by an enhanced absorption of the stellar radiation. A more realistic setup is considered in Section 5.3.3, where the diurnal variations of temperature are taken into account in addition to the zonal mean latitudinal temperature gradient. Saturn was chosen as a proxy for a cold gas giant planet in this simulations.

5.3 Results of simulations

5.3.1 Cold giant

Results of simulations after 300 model days with $\tau_{rad} = 10^6$ s are shown in Figure 5.4. They represent one day- and zonally averaged fields. The temperature (Figure 5.4a) is generally consistent with observations (Fletcher et al. 2010) and previous GCM modeling (Friedson and Moses 2012) of Saturn. Our model reproduces the pole-to-equator temperature gradient with the elevated minimum of up to 70 K in the low-latitude tropopause. This minimum is maintained adiabatically by the strong upwelling depicted in Figure 5.4b, where contours indicate the streamlines of the residual mean circulation, $\bar{\Psi}$ (see equation 4.1). It is seen that the net transport consists of two equator-to-pole cells. Such circulation was also inferred by Conrath et al. (1990, their Figure 10) in the calculations that ignored solar heating due to absorption by aerosols. The corresponding residual vertical velocity, w^* , plotted with color shades is up to ± 0.9 m s $^{-1}$ strong in low latitudes, and rapidly decreases away from the equator and higher. The Eulerian mean circulation, $\bar{\psi}$, in contrast, represents a series of cells generated by the prescribed \bar{u}_{obs} , which extend upward. This difference between the Eulerian-mean and residual circulations is due to strong eddies, and the correspondingly large Stokes drift. Simulated non-zonal variations of the wind reach hundreds of m s $^{-1}$ over the equator, and rapidly decrease with latitude. The intensity of the Eulerian circulation decreases as well, however the total of the Eulerian and Stokes drift still represents a poleward transport in both hemispheres.

The simulated zonal wind is plotted in Figure 5.4c with contour lines. A strong prograde jet dominates low latitudes with wind velocities up to 600 m s $^{-1}$, and is consistent with observational estimates (Read et al. 2009). Above ~ 2 mb, the wind reverses to east-

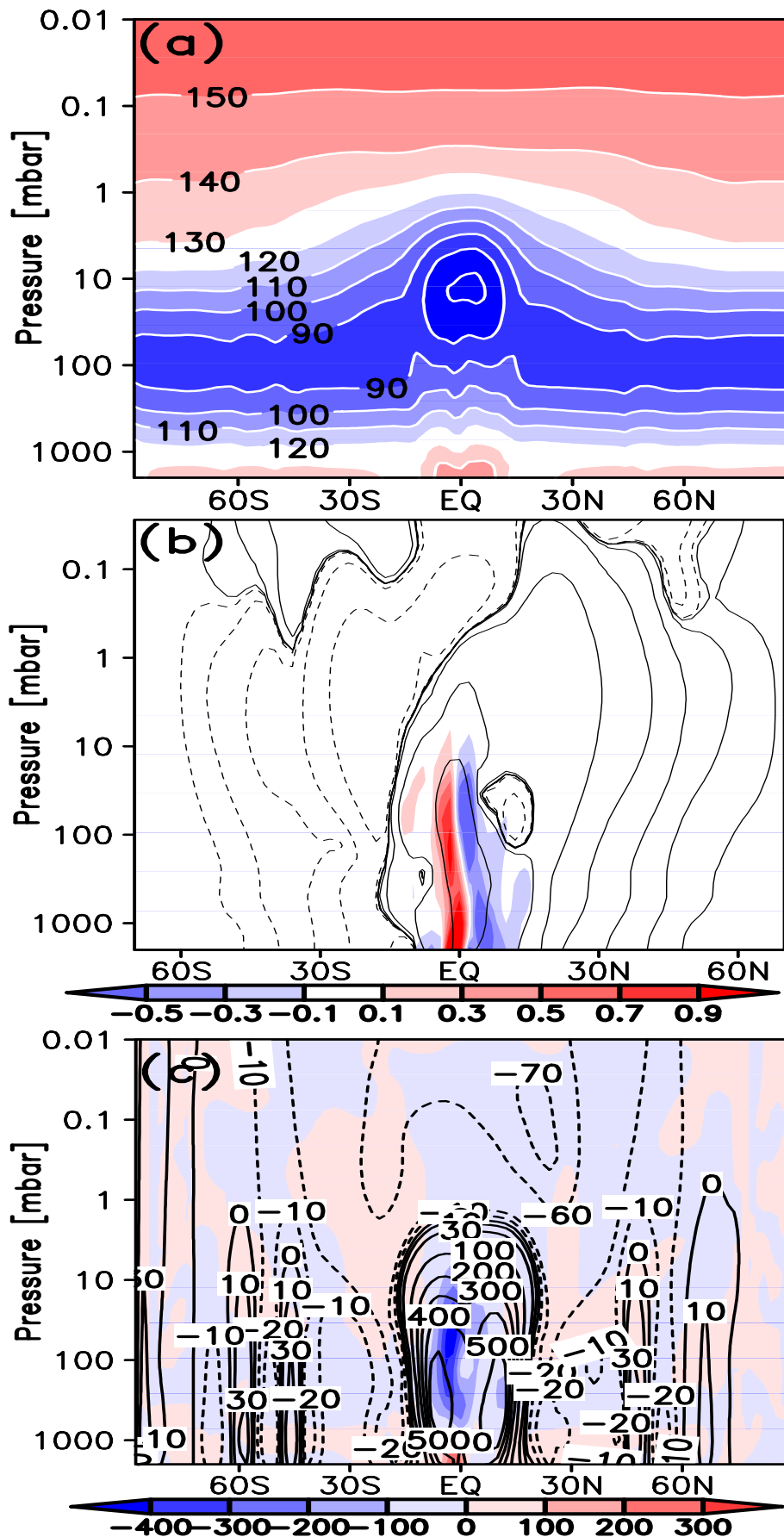


Figure 5.4: One-day averaged fields from the simulation for the cold giant: (a) Zonal mean temperature (in K), (b) residual streamfunction (contour lines) and residual vertical velocity (in m s^{-1} , shaded), (c) mean zonal wind (contours) and EP flux (in $\text{m s}^{-1} \text{ day}^{-1}$, shaded) divergence due to resolved eddies.

erlies, and the two weaker easterly jets flank the equatorial one, and extend from the lower boundary to the top of the model. This pattern with the retrograde wind up to -50 m s^{-1} at 0.01 mbar above 40°S is in agreement with the estimates of the thermal wind by Greathouse et al. (2005). Also seen are the alternating jets at higher latitudes that rapidly decay with height. Similar features of the zonal wind distribution were obtained by Conrath et al. (1981) in their analytical solution on f-plane with the Newtonian cooling, a realistic equilibrium Jovian temperature, and prescribed sinusoidal zonal winds on the lower boundary, who demonstrated that jets decay vertically with a characteristic e-folding length scale of about two pressure scale heights. More recently, such behavior was presented for solstices by Friedson and Moses (2012) in their simulations with a more realistic Saturn GCM.

Shaded areas in Figure 5.4c show the acceleration/deceleration of the mean zonal wind by non-zonal disturbances. This effect is represented by the divergence of Eliassen-Palm (EP) fluxes, which were calculated according to (Andrews et al. 1987):

$$a_x = \rho^{-1} \nabla \cdot \mathbf{F}, \quad (5.2)$$

where ∇ is the gradient in the spherical coordinates, and the EP flux vector $\mathbf{F} = (0, F_y, F_z)$ has the components

$$\begin{aligned} F_y &= \rho a \cos \phi (\bar{u}_z \overline{v'\theta'} / \bar{\theta}_z - \overline{v'u'}), \\ F_z &= \rho a \cos \phi \times \\ &\{ [f - (\cos \phi)^{-1} (\bar{u} \cos \phi)_y] \overline{v'\theta'} / \bar{\theta}_z - \overline{w'u'} \}. \end{aligned} \quad (5.3)$$

Most of the wave-mean flow interactions take place in the troposphere and lower stratosphere, where the main effect of eddies is to decelerate the local zonal wind. Upon dissipation they produce a westward drag of up to $400 \text{ m s}^{-1} \text{ day}^{-1}$ within the core of the equatorial jet. Away and above, the EP flux divergence decreases, as do the eddies. Typical height-longitude distributions of eddies are presented in Figure 5.5, where deviations of the meridional wind from its zonally averaged values, $v' = v - \bar{v}$, are plotted. At 20°S (panel a), the disturbances demonstrate wave-like structure with upward propagating phase. They dissipate above 500–600 km, and deposit their momentum to the flow. At 10°S (panel b), the eddies are vertically trapped in the troposphere, and have smaller horizontal extent. They are excited mainly due to barotropic instabilities within the core of the equatorial jet where horizontal wind shears are most strong. Areas of large amplitudes of waves (up to 500 m s^{-1}) correlate well with those with large imposed drag in the equatorial troposphere.

5.3.2 Cold giant with a latitudinal temperature gradient

Clearly, without local thermal forcing, the circulation in the stratosphere of the cold gas giant reminds of a Brewer-Dobson circulation on Earth, in which the residual transport extends from the equator to poles. The multiple Eulerian mean cells are vertical extensions of those imposed by alternating jets at the lower boundary. In the next experiment, we take into account the influence of the stellar/solar radiation. The latter must result in hotter temperatures as well as in its latitudinal contrasts.

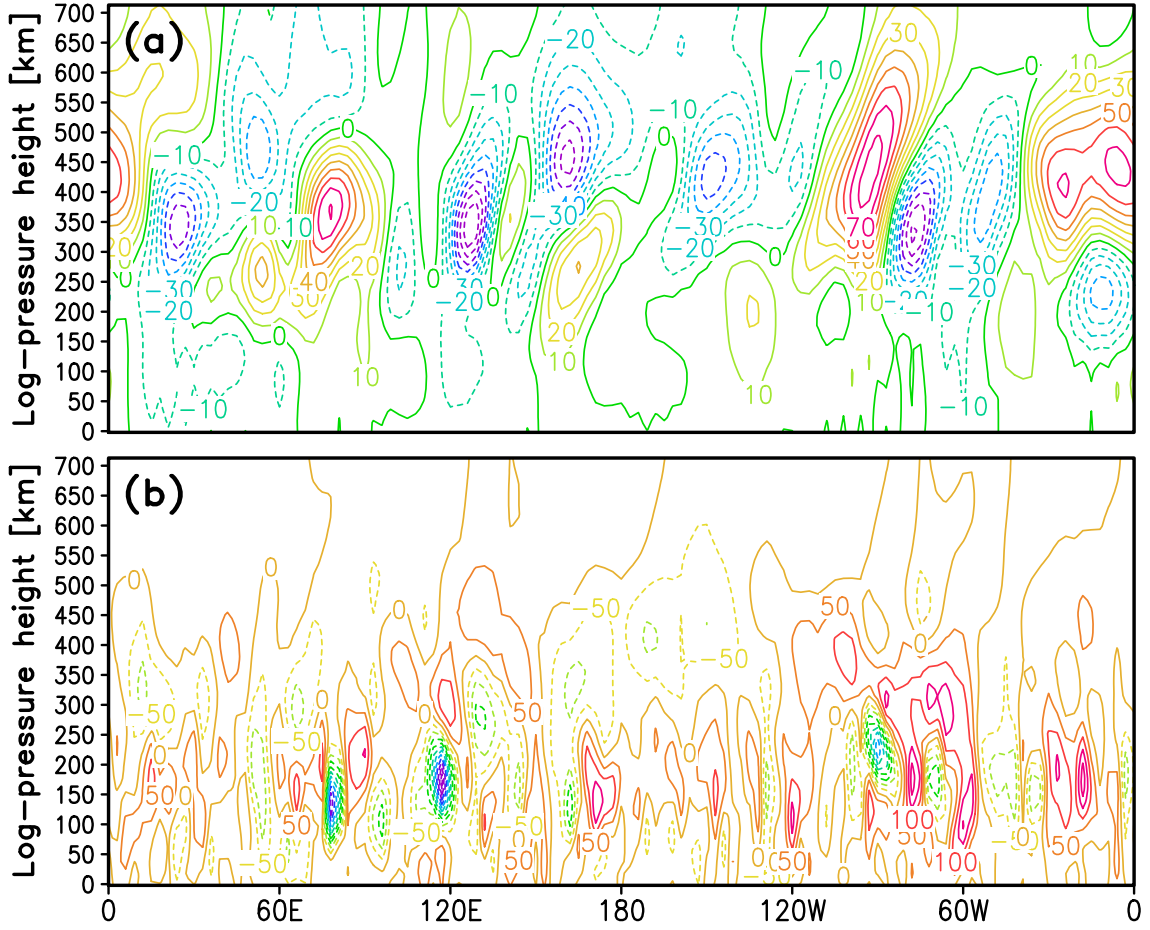


Figure 5.5: Longitude-height cross-sections of the simulated non-zonal disturbances of the meridional velocity, $v' = v - \bar{v}$ (in m s^{-1}), at (a) 20°S , and (b) 10°S .

Assuming for simplicity equinox conditions (or zero tilt of the rotational axis of the planet with respect to the orbital plane), it is plausible to consider that the resulting temperature is higher over the equator as it is exposed to larger incoming flux of stellar radiation. This can be accounted for in the model by prescribing a latitudinal dependence to the equilibrium temperature T_{eq} . Such temperature can arise if the main absorbers are located in the troposphere, as is the case with aerosols in the atmosphere of Saturn. Therefore, we impose $T_{eq}(\phi, z) = T_{eq}(z) + \Delta T_\phi(\phi, z)$, where ΔT_ϕ is parameterized after Menou and Rauscher (2009) such that T_{eq} at the poles is the same as in the cold giant run:

$$\Delta T_\phi(\phi, z) = F(z) [60^\circ \times (1/3 - \sin^2 \phi) + 40^\circ]. \quad (5.4)$$

The magnitude of temperature at the pole must satisfy two contradictory conditions. On one hand, it should be large enough so that effects are noticeable. On the other hand, it must be small enough in order not to alter the scale height significantly. In our simulations, the magnitude (60 K) was chosen rather arbitrary as a compromise between the two conditions. We also assume that this temperature change takes place only in the troposphere, thus leaving the stratosphere and its response unaffected directly:

$$F(z) = \sin\left(\frac{\pi}{2} \frac{z_{trop} - z}{z_{trop}}\right), \quad (5.5)$$

where z_{trop} is the log-scale height of the tropopause.

The simulated temperature in Figure 5.6a reflects the imposed meridional structure of T_{eq} . The equatorial minimum is now warmer by 10 K, and elevated higher by 50 to 100 km. The stratosphere in general is also warmer by 10 K, except immediately above the equatorial minimum. However, the major change occurred to the zonal wind. As seen from Figure 5.6b (contours), the prograde wind intensifies, and covers almost the entire globe, except for very weak easterly jets imposed at the lower boundary. This difference with the cold giant circulation is emphasized with color shades. Zonal winds increased by up to 300 m s^{-1} (in the flanks of the equatorial jet), and decreased by only 30 m s^{-1} near the lower boundary over the equator. The westerlies arisen according to the thermal wind relation are the result of the imposed meridional temperature gradient in the troposphere. Simulations (not shown here) confirm that the extent of prograde wind increases with ΔT_ϕ . The residual streamfunction in Figure 5.6c (contour lines) indicates that the two-cell equator-to-pole circulation was preserved, however, the pattern became more complex. The maximum of residual vertical velocities is shifted upward, and two return cells are formed in the lower troposphere. The return cells in the upper part of the modeling domain are apparently due to EP flux divergences associated with the enhanced dissipation of large-scale baroclinic wave near the top of the model. The vertical structure of non-zonal eddies is similar to the case of cold Saturn.

5.3.3 Warm giant planet with diurnally varying irradiation

The case above is highly idealistic, and was considered for methodological purposes only. Fast rotating planets that receive stellar irradiation appreciable enough to develop latitudinal temperature gradients, are almost certainly subject to diurnally varying heating. To account for this, we prescribed T_{eq} as

$$T_{eq}(\lambda, \phi, z, t) = T_{eq}(z) + \Delta T_\phi(\phi, z) + \delta T(\lambda, \phi, z, t), \quad (5.6)$$

where $T_{eq}(z)$ and ΔT_ϕ are the same as in in the simulations above, and

$$\delta T(\lambda, \phi, z, t) = 20^\circ \cos(\lambda + \Omega t) \cos(\phi) F(z). \quad (5.7)$$

Here the two cosine terms parameterize the star-following distribution of radiation fluxes on the sphere, and $F(z)$, same as in (5.5), defines the vertical extent of forcing in the troposphere. A similar expression but without time dependence was applied by Menou and Rauscher (2009) for simulating a tidally locked hot Jupiter. This setup imposes thermally driven diurnal tides in the lower atmosphere, leaving it free to penetrate into the stratosphere wherever the propagation conditions are favorable. The magnitude of diurnal temperature variations (20 K) was chosen arbitrarily, but keeping in mind that it must be noticeable for effects on the circulation to be seen, and small enough in order not to alter the density scale height significantly.

The simulated temperature and zonal wind shown in Figure 5.8 do not differ qualitatively from those presented in the previous subsection. The temperature in the stratosphere is by about 30 K lower in the equatorial region than in the cold giant case, and up to 10 K elsewhere. The zonal wind demonstrates a superrotation except in the equatorial troposphere with upward extensions of the westerly jets imposed at the lower boundary.

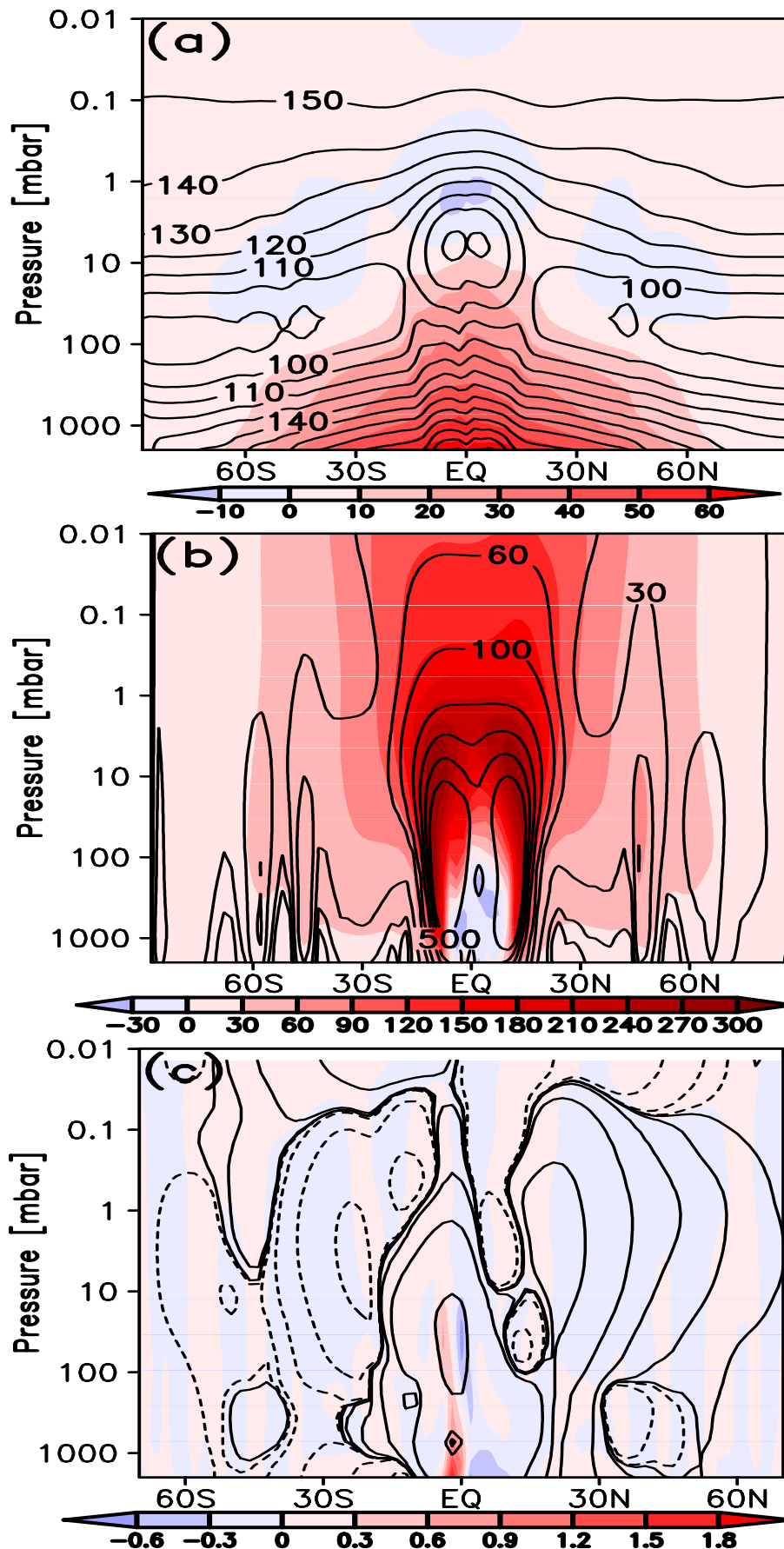


Figure 5.6: Latitude-height cross-sections of the fields simulated for the Saturn-like planet with the imposed meridional temperature gradient in the troposphere: (a) Temperature (contours) and deviations of the temperature from the “cold” giant case simulation (shaded); (b) mean zonal wind (contours) and deviations from the “cold” giant case; (c) residual meridional circulation (contours) and residual vertical velocity (shaded).

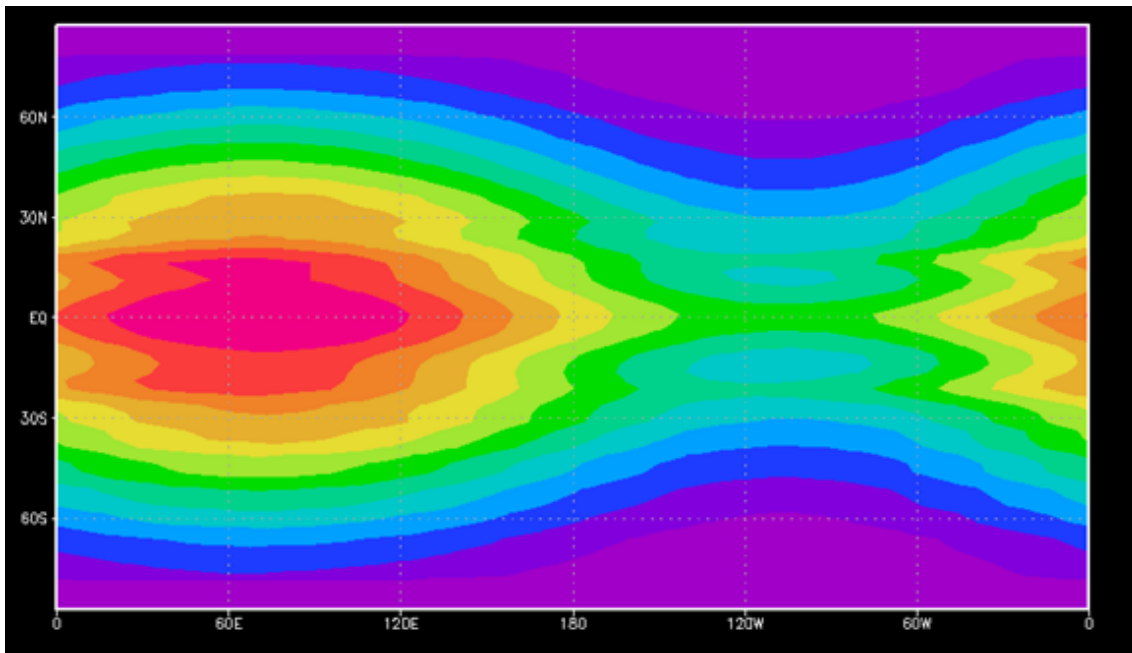


Figure 5.7: Latitude-longitude cross section snapshot showing the applied diurnally varying irradiation at the troposphere.

The most dramatic changes take place with the meridional circulation shown by contour lines in Figure 5.8c. They form a complex pattern with multiple cells, among which the most distinctive is the reversal of the broad cells in mid- and low latitudes. The dominating pattern now consists of a counter-clockwise transport in the Northern hemisphere, and clockwise in the Southern one. The direction of these cells is highlighted by residual vertical velocities plotted with color shades. Pink areas correspond to upward vertical motions, and, thus, explain the generally colder stratospheric temperatures in midlatitudes by adiabatic cooling associated with the simulated meridional transport. Such circulation was also obtained by West et al. (1992) for Jupiter, who included in their calculations heating due to absorption of solar radiation by atmospheric aerosols.

The other noticeable difference is the formation of two opposite circulation cells in the troposphere centered around 30°N and 30°S . Closer inspection shows that they are caused by the corresponding patches of the EP flux divergence. It follows from the zonally averaged equation (2.2) under scaling arguments, that the residual meridional velocity $\bar{v}^* \approx f^{-1}a_x$. Comparison shows that the distributions of v^* and a_x perfectly match outside an approximately $\pm 20^\circ$ band both in the troposphere and stratosphere. This implies that the simulated transport away from the equator is driven by eddies. Note that the meridional velocities are very weak there, and, generally, do not exceed 10 m s^{-1} . They are very sensitive to resolved eddies in the model, and to the associated EP flux divergence, in particular. Our tests with enhanced horizontal diffusion (not shown here) that imposes an additional damping on non-zonal disturbances demonstrates changing patterns of smaller-scale circulation cells. At the same time, the simulated overall pole-to-equator transport holds, although its magnitude varies. Two height-longitude snapshots of non-zonal disturbances of the meridional velocity, $v' = v - \bar{v}$, are given in Figure 5.9. They illustrate a highly irregular structure of eddies. The downward phase progression of v' in the strato-

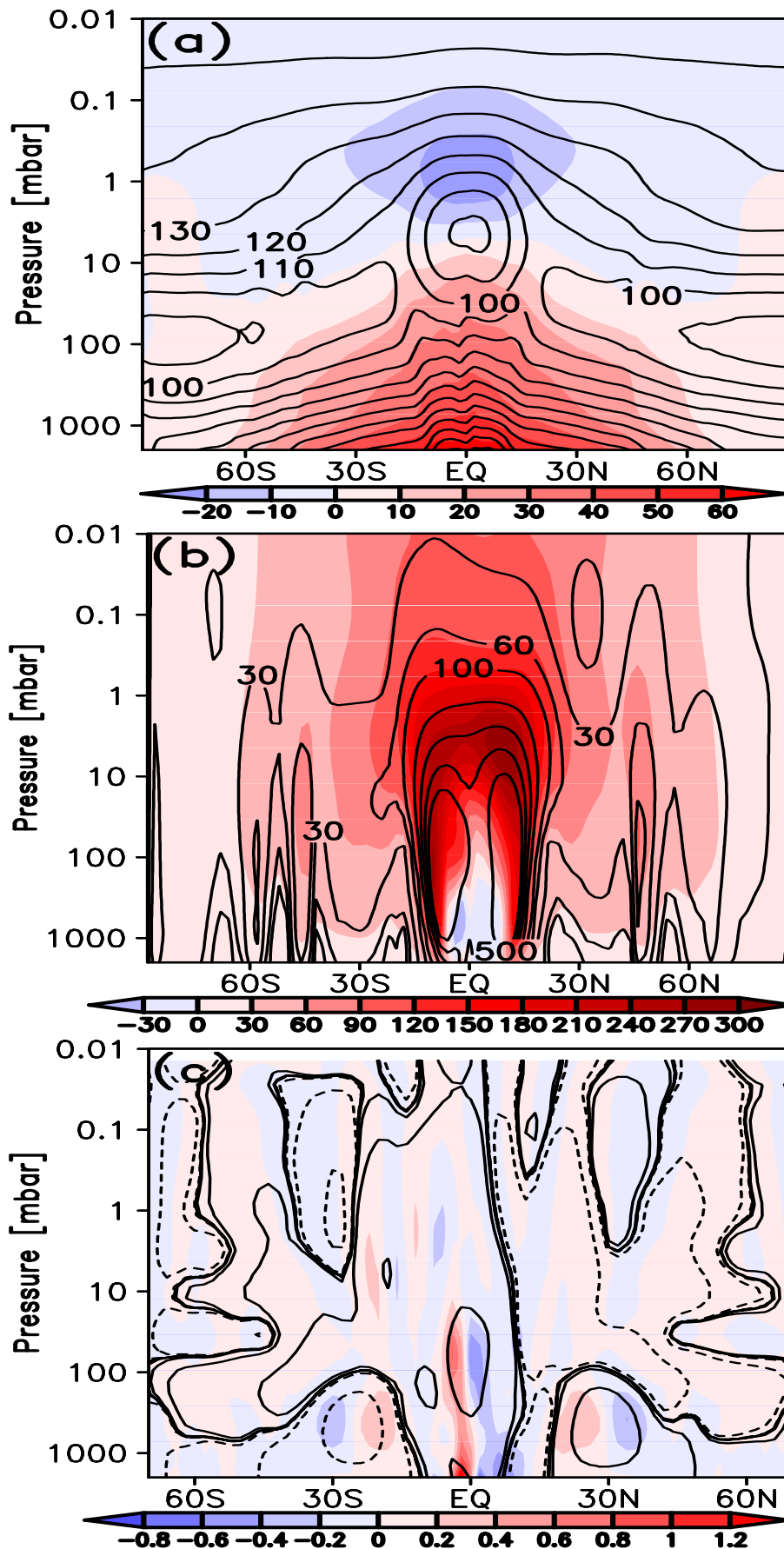


Figure 5.8: Same as in Figure 5.6, but for the simulation with the imposed meridional gradient and diurnal temperature variations.

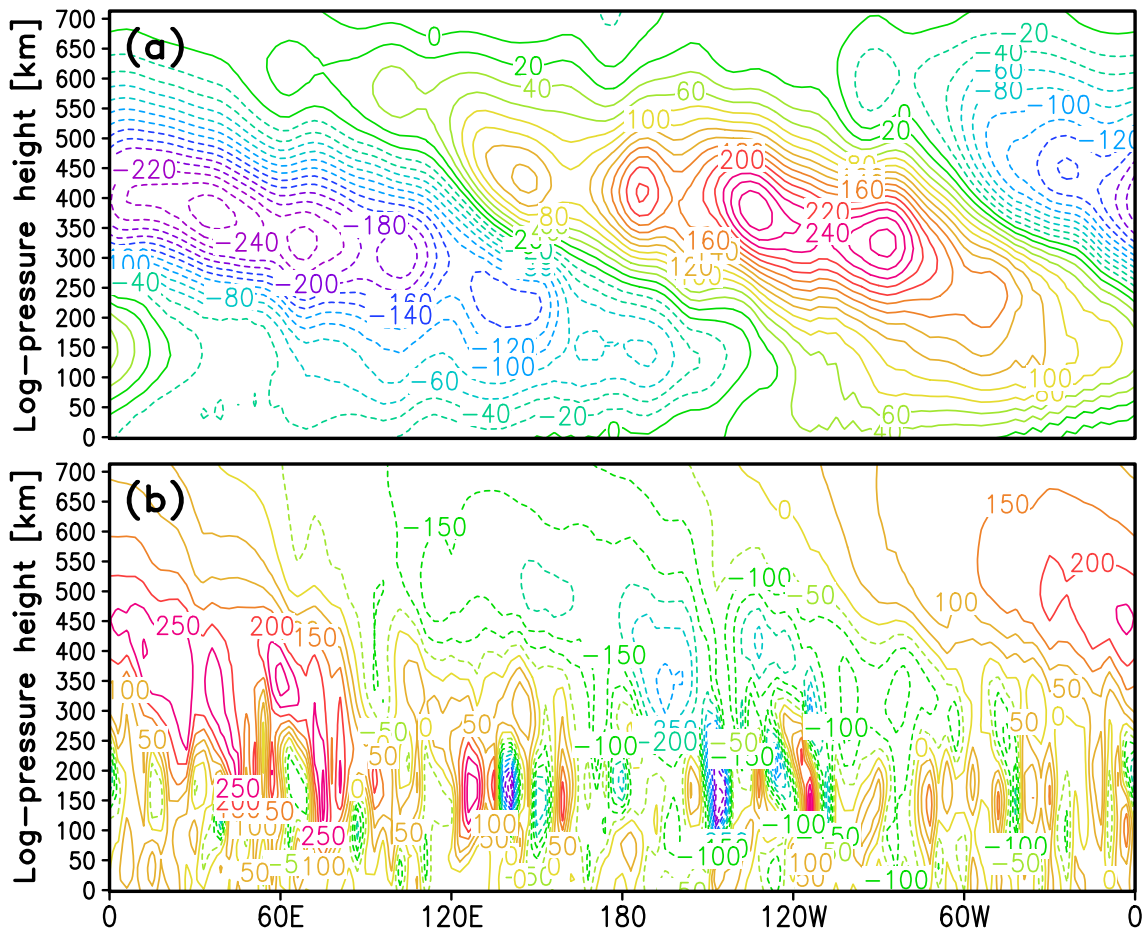


Figure 5.9: Same as in Figure 5.5, but for the simulation with the imposed meridional temperature gradient and diurnal temperature variations.

sphere points out to the upward (positive group velocity) propagation of the tide. Despite very modest variations of temperature in the troposphere, the tidal amplitude grows with height, and reaches its maximum up to 300 m s^{-1} at 20°S around 400–450 km, as seen in Figure 5.9a. Above, the amplitude decreases due to dissipation, and the released momentum is deposited to the mean flow. The tidal signature dominates in the stratosphere at all latitudes. At 10°S (Figure 5.9b), the tidal amplitude is weaker, while vertically trapped shallow eddies in the troposphere are exceptionally strong as in the benchmark simulation for a cold planet. Away from low latitudes, the tropospheric disturbances sharply decay, and the tidal oscillations with almost barotropic structure dominate the entire atmosphere. Such behavior is almost likely linked to the insufficient horizontal resolution in our model. As the Rossby radius of deformation decreases toward the pole, most of eddies become unresolved, and their effect on the circulation is not captured. Also not captured are effects of smaller-scale gravity waves, which, given a highly volatile circulation in the lower atmosphere, must be generated in abundance. Upon their vertical propagation, amplitudes of such waves grow exponentially, and cause significant dynamical and thermal impact on the mean circulation upon their dissipation and breaking. Parameterizations of gravity waves for GCMs accounting for all these effects are available (Yiğit et al. 2008), but their constraining for exoplanets is limited if not impossible at the moment.

5.4 Summary of results for “warm” gas giant planet simulations

These simulations with the three-dimensional general circulation model reveal how global circulations in the stratospheres of cold gas giant planets change if heating due to absorption of stellar radiation increases. Such planets in the solar System (Jupiter and Saturn) are at a considerable distance from the Sun, and their atmospheres receive relatively little radiative energy compared to that from their interiors. On the other hand, discoveries of gas giant exoplanets at very close orbits to their stars (hot Jupiters) as well as giants that are not tidally locked allow to assume that there are planets at intermediate orbits, which rotate fast, and whose atmospheres are driven both from the interior and by an in-situ heating.

Despite a highly idealized setup and apparently not sufficient horizontal resolution, our experiments demonstrated several important common features.

1. Circulation in the stratospheres of fast rotating giant planets is strongly driven by vertically propagating eddies. Especially sensitive to them is the meridional circulation, which is generally weak. While the Eulerian mean transport largely reflects the multiple tropospheric cells, the net (residual) circulation may differ significantly due to the Stokes drift produced by the waves.

2. Inclusion of a latitudinal temperature gradient in the troposphere alters the simulated winds in the stratosphere: the prograde zonal jet extends on the whole planet.

3. It is found that thermal tides included in the simulations effectively propagate upward, dominate in the stratosphere, and create a momentum forcing that affect the circulation in upper layers. Strong eddies in the troposphere are usually trapped vertically, and their effect is mainly to decelerate the local mean zonal wind.

4. Horizontal resolution and imposed diffusion strongly affect the simulated eddies, and, thus, the global circulation. Higher resolution is required to capture wave-mean flow interactions in the atmospheres of cold gas giant planets.

Our study also demonstrated an applicability of the dynamical solver of primitive equations for modeling atmospheric general circulations on Jupiter-type planets under a variety of conditions. It also showed a methodological suitability for studying atmospheric dynamics of giant gas exoplanets.

6 Conclusions

The aim of this thesis was to study the dynamics of the stratospheres of gas giant planets. Although Jupiter and Saturn were intensively explored observationally and theoretically, the stratospheric circulations on these planets still remain largely unknown. In order to achieve the goal, a three-dimensional general circulation model (GCM) has been developed, and a series of numerical simulations have been performed.

Peculiarities of atmospheric dynamics on gas giants demanded serious modifications to the dynamical core suitable for terrestrial-like planets. They include changing horizontal and vertical spacing, the time integration algorithm, the implementation of parameterized subgrid-scale processes, and a new horizontal diffusion scheme. The code of the developed gridpoint primitive equation model was highly optimized, parallelized, vectorized, and made portable to deliver a performance, which would, in turn, allow high-resolution simulations. Extensive sensitivity simulations have been performed to estimate the impact of the imposed diffusion, and to optimize the model between requirements of model stability and reproducing strong winds and eddies. These simulations proved an importance of resolving the fundamental length scale, the Rossby radius of deformation, and its effects on the simulated flow.

This modeling study clarified many aspects of the stratospheric circulation on gas giants, which were not approached before, because of scarcity of observations and limited number of three-dimensional GCMs suitable for middle atmospheres of gas giants. Among them are vertical extensions of the tropospheric zonal jets, and the meridional circulation. It was found that the jets decrease with altitude, more steeply on Saturn than on Jupiter. The simulations predict weak meridional circulation with two equator-to-pole cells superimposed on the multiple cells in the lower stratosphere associated with tropospheric zones and bands. This agrees with observations of traces of Shoemaker-Levy 9 comet on Jupiter. Being weak, the meridional circulation is very sensitive to diabatic heating and cooling. Thus, an accurate accounting for spatial distributions of heating rates by radiatively active trace gases and aerosols is required.

The model successfully reproduces very strong eddy activity in the equatorial regions of Saturn and Jupiter. In particular, it reproduces the so-called “chevrons”, which have not been simulated before. Our numerical experiments show that they are vertically trapped, and, apparently, have barotropic origin structure. Their main effect is to decelerate the local zonal jets. The model is able to reproduce the observed hotspots and thermal waves on Jupiter. On Jupiter, the dominant harmonic has the wavenumber 6, and periods around 80 Jupiter days. This is close to the found ~ 96 day wave in the North Equatorial Band (Li et al. 2006b). A similar analysis on Saturn reveals the wavenumber 9 harmonic, in accordance with the observations (Liming et al. 2008). Higher into the stratosphere and away from the equator, various vertically propagating planetary waves were simulated

with the GCM.

An idealized experiment was also designed and performed to explore how the circulation on a Solar System-like Saturn changes if the planet moves closer to the star. This represents a transiting case between “cold” and “hot” exoplanet Jupiters, which have been detected in large quantities. These simulations of a “warm” gas giant revealed the importance of eddies in driving the middle atmospheres, and showed that the prograde equatorial jet spreads to the whole globe with an increase of stellar irradiation.

The results of numerical experiments indicate that the developed 3-dimensional GCM is suitable for modeling the middle atmospheres of gas giant planets. The future more realistic simulations will require implementation of accurate physical parameterizations, a radiative heating/cooling scheme foremost, and increase of resolution.

List of symbols

a	Planetary radius
c_p	Specific heat capacity at constant pressure
dx	Distance increment along the longitude λ
dy	Distance increment along the latitude ϕ
f	Coriolis parameter
\mathbf{F}	EP flux vector
g	Acceleration of gravity
H	Density scale height
k	Thermal conduction coefficient
k_β	Wavenumber
K_H	Diffusion coefficient
L	Characteristic length scale
L_D	Rossby radius of deformation
L_β	Rhines length scale
N	Brunt-Väisälä frequency (buoyancy frequency)
N_ϕ	Number of grid points in latitude
p	Pressure
p_s	Reference pressure
$Q(T)$	Heating/cooling rate at a given temperature
R	Specific gas constant
Re	Reynolds number
T	Characteristic temperature
T	Temperature
T_{eff}	Global average blackbody temperature
T_{eq}	Equilibrium temperature
U	Root mean square fluid velocity
U_c	Characteristic horizontal wind speed
u	Wind component along the longitude λ
u'	Eddy deviation from mean zonal wind speed
u_{obs}	Observed zonal wind
V	Characteristic velocity of the flow
v	Wind component along the latitude ϕ
v'	Eddy deviation from mean meridional wind speed
w	Wind component along the log-pressure height z
w^*	Residual vertical velocity
w'	Eddy deviation from mean vertical wind speed
w_a	Adiabatic vertical velocity

List of symbols

z	Height above a fiducial surface
α	Robert-Asselin-Williams filter coefficient
$\alpha_{Asselin}$	Robert-Asselin filter coefficient
β	Latitudinal northward gradient of the Coriolis parameter
Γ	Lapse rate
Γ_d	Dry adiabatic lapse rate
κ	R/c_p , ratio of specific gas constant to specific heat capacity at constant pressure
λ	Longitude
μ	Dynamic viscosity of the fluid
∇	Gradient in the spherical coordinates
ν	Kinematic viscosity of the fluid
ν_{mol}	Kinematic molecular viscosity of the fluid
Ω	Planetary rotational frequency
ϕ	Latitude
Φ	Planetary potential
Ψ	Residual mean circulation
ψ	Eulerian mean meridional transport
ρ	Density
τ_u	Characteristic zonal wind relaxation time
τ_{dyn}	Characteristic dynamical timescale
τ_{rad}	Radiative relaxation time
θ	Potential temperature
θ'	Eddy deviation from mean potential temperature

Bibliography

- Achilleos, N., Miller, S., Tennyson, J., Aylward, A. D., Mueller-Wodarg, I., Rees, D., 1998, JIM: A time-dependent, three-dimensional model of Jupiter's thermosphere and ionosphere, *Journal of Geophysical Research: Planets*, 103, 20 089–20 112
- Achterberg, R. K., Flasar, F. M., 1996, Planetary-Scale Thermal Waves in Saturn's Upper Troposphere, *Icarus*, 119, 350 – 369
- Allison, M., 1990, Planetary waves in Jupiter's equatorial atmosphere, *Icarus*, 83, 282 – 307
- Andrews, D. G., Holton, J. R., Leovy, C. B., 1987, *Middle atmosphere dynamics*, Academic Press, San Diego, Calif
- Appleby, J. F., Hogan, J. S., 1984, Radiative-convective equilibrium models of Jupiter and Saturn, *Icarus*, 59, 336 – 366
- Arakawa, A., Lamb, V. R., 1977, Computational Design of the Basic Dynamical Processes of the UCLA General Circulation Model, *General Circulation Models of the Atmosphere, Methods in Computational Physics: Advances in Research and Applications*, Elsevier, 17, 173 – 265
- Arakawa, A., Moorthi, S., 1988, Baroclinic Instability in Vertically Discrete Systems, *Journal of Atmospheric Sciences*, 45, 1688–1708
- Arregi, J., Rojas, J. F., Hueso, R., Sánchez-Lavega, A., 2009, Gravity waves in Jupiter's equatorial clouds observed by the Galileo orbiter, *Icarus*, 202, 358 – 360
- Asselin, R., 1972, Frequency Filter for Time Integrations, *Monthly Weather Review*, 100, 487
- Atkinson, D. H., Pollack, J. B., Seiff, A., 1996, Galileo Doppler Measurements of the Deep Zonal Winds at Jupiter, *Science*, 272, 842–843
- Atkinson, D. H., Pollack, J. B., Seiff, A., 1998, The Galileo Probe Doppler Wind Experiment: Measurement of the deep zonal winds on Jupiter, *Journal of Geophysical Research: Planets*, 103, 22 911–22 928
- Atreya, S. K., Wong, A., 2005, *Coupled Clouds and Chemistry of the Giant Planets - A Case for Multiprobes*, in *The Outer Planets and their Moons*, Space Sciences Series of ISSI, ISBN 978-1-4020-3362-9

- Atreya, S. K., Wong, M. H., Owen, T. C., Mahaffy, P. R., Niemann, H. B., de Pater, I., Drossart, P., Th Encrenaz, 1999, A comparison of the atmospheres of Jupiter and Saturn: deep atmospheric composition, cloud structure, vertical mixing, and origin, *Planetary and Space Science*, 47, 1243 – 1262
- Aurnou, J., Heimpel, M., Allen, L., King, E., Wicht, J., 2008, Convective heat transfer and the pattern of thermal emission on the gas giants, *Geophysical Journal International*, 173, 793–801
- Aurnou, J. M., Olson, P. L., 2001, Strong zonal winds from thermal convection in a rotating spherical shell, *Geophysical Research Letters*, 28, 2557–2559
- Baines, K. H., Momary, T. W., Fletcher, L. N., Showman, A. P., Roos-Serote, M., Brown, R. H., Buratti, B. J., Clark, R. N., Nicholson, P. D., 2009, Saturn's north polar cyclone and hexagon at depth revealed by Cassini/VIMS, *Planetary and Space Science*, 57, 1671 – 1681
- Baldwin, M. P., Gray, L. J., Dunkerton, T. J., Hamilton, K., Haynes, P. H., Randel, W. J., Holton, J. R., Alexander, M. J., Hirota, I., Horinouchi, T., Jones, D. B. A., Kinnerson, J. S., Marquardt, C., Sato, K., Takahashi, M., 2001, The quasi-biennial oscillation, *Reviews of Geophysics*, 39, 179–229
- Banfield, D., Gierasch, P. J., Bell, M., Ustinov, E., Ingersoll, A. P., Vasavada, A. R., West, R. A., Belton, M. J. S., 1998, Jupiter's Cloud Structure from Galileo Imaging Data, *Icarus*, 135, 230 – 250
- Bagenal, F., Dowling, T. E., McKinnon, W. B., 2004, in *Jupiter: The Planet, Satellites and Magnetosphere*, F. Bagenal, T. E. Dowling, W. B. McKinnon, Eds., Cambridge Univ. Press, Cambridge
- Barnet, C. D., Beebe, R. F., Conrath, B. J., 1992, A seasonal radiative-dynamic model of Saturn's troposphere, *Icarus*, 98, 94–107
- Batteen, M. L., Han, Y. J., 1981, On the computational noise of finite-difference schemes used in ocean models, *Tellus*, 33, 387–396
- Beebe, R. F., Ingersoll, A. P., Hunt, G. E., Mitchell, J. L., Müller, J., 1980, Measurements of wind vectors, eddy momentum transports, and energy conversions in Jupiter's atmosphere from Voyager 1 images, *Geophysical Research Letters*, 7, 1–4
- Bézar, B., Gautier, D., Conrath, B., 1984, A seasonal model of the Saturnian upper troposphere: Comparison with Voyager infrared measurements, *Icarus*, 60, 274 – 288
- Bézar, B., Lellouch, E., Strobel, D., Maillard, J., Drossart, P., 2002, Carbon Monoxide on Jupiter: Evidence for Both Internal and External Sources, *Icarus*, 159, 95–111
- Brewer, A. W., 1949, Evidence for a world circulation provided by the measurements of helium and water vapor distribution in the stratosphere, *Quart. J. Roy. Meteor. Soc.*, 75, 351–363

- Busse, F. H., 1976, A simple model of convection in the Jovian atmosphere, *Icarus*, 29, 255 – 260
- Busse, F. H., 2002, Convective flows in rapidly rotating spheres and their dynamo action, *Physics of Fluids*, 14, 1301–1314
- Cavalié, T., Billebaud, F., Dobrijevic, M., Fouchet, T., Lellouch, E., Encrenaz, T., Brillet, J., Moriarty-Schieven, G. H., Wouterloot, J. G. A., Hartogh, P., 2009, First observation of CO at 345 GHz in the atmosphere of Saturn with the JCMT: New constraints on its origin, *Icarus*, 203, 531–540
- Cavalié, T., Hartogh, P., Billebaud, F., Dobrijevic, M., Fouchet, T., Lellouch, E., Encrenaz, T., Brillet, J., Moriarty-Schieven, G. H., 2010, A cometary origin for CO in the stratosphere of Saturn?, *Astron. and Astrophys.*, 510, A88
- Cavalié, T., Biver, N., Hartogh, P., Dobrijevic, M., Billebaud, F., Lellouch, E., Sandqvist, A., Brillet, J., Lecacheux, A., Hjalmarson, Å., Frisk, U., Olberg, M., Odin Team, 2012, Odin space telescope monitoring of water vapor in the stratosphere of Jupiter, *Planet. Space Sci.*, 61, 3–14
- Cavalié, T., Feuchtgruber, H., Lellouch, E., de Val-Borro, M., Jarchow, C., Moreno, R., Hartogh, P., Orton, G., Greathouse, T. K., Billebaud, F., Dobrijevic, M., Lara, L. M., González, A., Sagawa, H., 2013, Spatial distribution of water in the stratosphere of Jupiter from Herschel HIFI and PACS observations, *Astronomy and Astrophysics*, 553, A21
- Chan, K. L., Mayr, H. G., 2008, A shallow convective model for Jupiter’s alternating wind bands, *Journal of Geophysical Research: Planets*, 113
- Charney, J. G., Flierl, G. R., 1981, Oceanic Analogues of Large-Scale Atmospheric Motions, in *Evolution of Physical Oceanography*, edited by B. Warren and C. Wunsch, pp. 502–546
- Charney, J. G., Phillips, N. A., 1953, Numerical Integration of the Quasi-Geostrophic Equations for Barotropic and Simple Baroclinic Flows, *J. Meteor.*, 10, 71–99
- Cho, J. Y. K., Polvani, L. M., 1996, The emergence of jets and vortices in freely evolving, shallow-water turbulence on a sphere, *Physics of Fluids*, 8, 1531–1552
- Cho, J. Y. K., Menou, K., Hansen, B. M. S., Seager, S., 2008, Atmospheric Circulation of Close-in Extrasolar Giant Planets. I. Global, Barotropic, Adiabatic Simulations, *ApJ*, 675, 817–845
- Choi, D. S., Showman, A. P., Brown, R. H., 2009, Cloud features and zonal wind measurements of Saturn’s atmosphere as observed by Cassini/VIMS, *Journal of Geophysical Research (Planets)*, 114, 4007
- Christensen, U. R., 2001, Zonal flow driven by deep convection in the major planets, *Geophysical Research Letters*, 28, 2553–2556

- Conrath, B. J., Gierasch, P. J., 1983, Evidence for disequilibrium of ortho and para hydrogen on Jupiter from Voyager IRIS measurements, *Nature*, 306, 571
- Conrath, B. J., Gierasch, P. J., 1984, Global variation of the para hydrogen fraction in Jupiter's atmosphere and implications for dynamics on the outer planets, *Icarus*, 57, 184 – 204
- Conrath, B. J., Pirraglia, J. A., 1983, Thermal structure of Saturn from Voyager infrared measurements: Implications for atmospheric dynamics, *Icarus*, 53, 286 – 292
- Conrath, B. J., Flasar, F. M., Pirraglia, J. A., Gierasch, P. J., Hunt, G. E., 1981, Thermal structure and dynamics of the Jovian atmosphere. II - Visible cloud features, *JGR*, 86, 8769–8775
- Conrath, B. J., Hanel, R. A., Samuelson, R. E., 1989, Thermal structure and heat balance of the outer planets, in *Origin and evolution of planetary and satellite atmospheres*, edited by S. K. Atreya et al., Univ. of Arizona Press, Tucson, Ariz., 53
- Conrath, B. J., Gierasch, P. J., Leroy, S. S., 1990, Temperature and circulation in the stratosphere of the outer planets, *Icarus*, 83, 255 – 281
- Conrath, B. J., Gierasch, P. J., Ustinov, E. A., 1998, Thermal Structure and Para Hydrogen Fraction on the Outer Planets from Voyager IRIS Measurements, *Icarus*, 135, 501 – 517
- Cook, A. F., Duxbury, T. C., Hunt, G. E., 1979, First results on Jovian lightning, *Nature*, 280, 794–794
- Courant, R., Friedrichs, K., Lewy, H., 1967 (1928), On the partial difference equations of mathematical physics, *IBM Journal of Research and Development*, 11(2), 215–234
- Del Genio, A. D., Barbara, J. M., 2012, Constraints on Saturn's tropospheric general circulation from Cassini ISS images, *Icarus*, 219, 689 – 700
- Del Genio, A. D., Achterberg, R. K., Baines, K. H., Flasar, F. M., Read, P. L., Sánchez-Lavega, A., Showman, A. P., 2009, Saturn Atmospheric Structure and Dynamics, in *Saturn from Cassini-Huygens*, pp. 113–159
- Deming, D., Reuter, D., Jennings, D., Bjoraker, G., McCabe, G., Fast, K., Wiedemann, G., 1997, Observations and Analysis of Longitudinal Thermal Waves on Jupiter, *Icarus*, 126, 301 – 312
- Dobson, G. M. B., 1956, Origin and distribution of the polyatomic molecules in the atmosphere, *Proc. R. Soc. London*, 236, 187–193
- Dowling, T. E., 1995, DYNAMICS OF JOVIAN ATMOSPHERES, *Annual Review of Fluid Mechanics*, 27, 293–334
- Dowling, T. E., Fischer, A. S., Gierasch, P. J., Harrington, J., LeBeau, Jr., R. P., Santori, C. M., 1998, The Explicit Planetary Isentropic-Coordinate (EPIC) Atmospheric Model, *Icarus*, 132, 221 – 238

- Dyudina, U. A., Genio, A. D. D., Ingersoll, A. P., Porco, C. C., West, R. A., Vasavada, A. R., Barbara, J. M., 2004, Lightning on Jupiter observed in the line by the Cassini imaging science subsystem, *Icarus*, 172, 24–36
- Flasar, F. M., 1986, Global dynamics and thermal structure of Jupiter's atmosphere, *Icarus*, 65, 280 – 303
- Flasar, F. M., Gierasch, P. J., 1986, Mesoscale Waves as a Probe of Jupiter's Deep Atmosphere, *J. Atmos. Sci.*, 43, 2683–2707
- Flasar, F. M., Kunde, V. G., Abbas, M. M., Achterberg, R. K., Ade, P., Barucci, A., Bézard, B., Bjoraker, G. L., Brasunas, J. C., Calcutt, S., Carlson, R., Césarsky, C. J., Conrath, B. J., Coradini, A., Courtin, R., Coustenis, A., Edberg, S., Edgington, S., Ferrari, C., Fouchet, T., Gautier, D., Gierasch, P. J., Grossman, K., Irwin, P., Jennings, D. E., Lellouch, E., Mamoutkine, A. A., Marten, A., Meyer, J. P., Nixon, C. A., Orton, G. S., Owen, T. C., Pearl, J. C., Prangé, R., Raulin, F., Read, P. L., Romani, P. N., Samuelson, R. E., Segura, M. E., Showalter, M. R., Simon-Miller, A. A., Smith, M. D., Spencer, J. R., Spilker, L. J., Taylor, F. W., 2004, Exploring The Saturn System In The Thermal Infrared: The Composite Infrared Spectrometer, *Space Sci. Rev.*, 115, 169–297
- Flasar, F. M., Kunde, V. G., Achterberg, R. K., Conrath, B. J., Simon-Miller, A. A., Nixon, C. A., Gierasch, P. J., Romani, P. N., Bézard, B., Irwin, P., Bjoraker, G. L., Brasunas, J. C., Jennings, D. E., Pearl, J. C., Smith, M. D., Orton, G. S., Spilker, L. J., Carlson, R., Calcutt, S. B., Read, P. L., Taylor, F. W., Parrish, P., Barucci, A., Courtin, R., Coustenis, A., Gautier, D., Lellouch, E., Marten, A., Prangé, R., Biraud, Y., Fouchet, T., Ferrari, C., Owen, T. C., Abbas, M. M., Samuelson, R. E., Raulin, F., Ade, P., Césarsky, C. J., Grossman, K. U., Coradini, A., 2004, An intense stratospheric jet on Jupiter, *Nature*, 427, 132–135
- Flasar, F. M., Achterberg, R. K., Conrath, B. J., Pearl, J. C., Bjoraker, G. L., Jennings, D. E., Romani, P. N., Simon-Miller, A. A., Kunde, V. G., Nixon, C. A., Bézard, B., Orton, G. S., Spilker, L. J., Spencer, J. R., Irwin, P. G. J., Teanby, N. A., Owen, T. C., Brasunas, J., Segura, M. E., Carlson, R. C., Mamoutkine, A., Gierasch, P. J., Schinder, P. J., Showalter, M. R., Ferrari, C., Barucci, A., Courtin, R., Coustenis, A., Fouchet, T., Gautier, D., Lellouch, E., Marten, A., Prangé, R., Strobel, D. F., Calcutt, S. B., Read, P. L., Taylor, F. W., Bowles, N., Samuelson, R. E., Abbas, M. M., Raulin, F., Ade, P., Edgington, S., Pilorz, S., Wallis, B., Wishnow, E. H., 2005, Temperatures, Winds, and Composition in the Saturnian System, *Science*, 307, 1247–1251
- Fletcher, L. N., Irwin, P. G. J., Teanby, N. A., Orton, G. S., Parrish, P. D., R. de Kok, Howett, C., Calcutt, S. B., Bowles, N., Taylor, F. W., 2007, Characterising Saturn's vertical temperature structure from Cassini/CIRS, *Icarus*, 189, 457 – 478
- Fletcher, L. N., Achterberg, R. K., Greathouse, T. K., Orton, G. S., Conrath, B. J., Simon-Miller, A. A., Teanby, N., Guerlet, S., Irwin, P. G. J., Flasar, F. M., 2010, Seasonal change on Saturn from Cassini/CIRS observations, 2004-2009, *Icarus*, 208, 337 – 352

- Fletcher, L. N., Orton, G. S., de Pater, I., Mousis, O., 2010, Jupiter's stratospheric hydrocarbons and temperatures after the July 2009 impact from VLT infrared spectroscopy, *Astr. Astrophys.*, 524, A46
- Fletcher, L. N., Baines, K. H., Momary, T. W., Showman, A. P., Irwin, P. G. J., Orton, G. S., Roos-Serote, M., Merlet, C., 2011, Saturn's tropospheric composition and clouds from Cassini/VIMS 4.6-5.1 μm nightside spectroscopy, *Icarus*, 214, 510–533
- Fletcher, L. N., Hesman, B. E., Achterberg, R. K., Irwin, P. G. J., Bjoraker, G., Gorius, N., Hurley, J., Sinclair, J., Orton, G. S., Legarreta, J., García-Melendo, E., Sánchez-Lavega, A., Read, P. L., Simon-Miller, A. A., Flasar, F., 2012, The origin and evolution of Saturn's 2011-2012 stratospheric vortex, *Icarus*, 221, 560 – 586
- Fletcher, L. N., Swinyard, B., Salji, C., Polehampton, E., Fulton, T., Sidher, S., Lellouch, E., Moreno, R., Orton, G., Cavalié, T., Courtin, R., Rengel, M., Sagawa, H., Davis, G. R., Hartogh, P., Naylor, D., Walker, H., Lim, T., 2012, Sub-millimetre spectroscopy of Saturn's trace gases from Herschel/SPIRE, *Astron. and Astrophys.*, 539, A44
- Fouchet, T., Lellouch, E., Bézard, B., Feuchtgruber, H., Drossart, P., Encrenaz, T., 2000, Jupiter's hydrocarbons observed with ISO-SWS: vertical profiles of C_2H_6 and C_2H_2 , detection of $\text{CH}_3\text{C}_2\text{H}$, *Astron. Astrophys.*, 355, L13–L17
- Fouchet, T., Lellouch, E., Feuchtgruber, H., 2003, The hydrogen ortho-to-para ratio in the stratospheres of the giant planets, *Icarus*, 161, 127–143
- Fouchet, T., Guerlet, S., Strobel, D. F., Simon-Miller, A. A., Bézard, B., Flasar, F. M., 2008, An equatorial oscillation in Saturn's middle atmosphere, *Nature*, 453, 200 – 202
- Friedson, A. J., 1999, New Observations and Modelling of a QBO-Like Oscillation in Jupiter's Stratosphere, *Icarus*, 137, 34 – 55
- Friedson, A. J., Moses, J. I., 2012, General circulation and transport in Saturn's upper troposphere and stratosphere, *Icarus*, 218, 861 – 875
- Friedson, A. J., West, R. A., Hronek, A. K., Larsen, N. A., Dalal, N., 1999, Transport and Mixing in Jupiter's Stratosphere Inferred from Comet S-L9 Dust Migration, *Icarus*, 138, 141 – 156
- García-Melendo, E., Sánchez-Lavega, Hueso, R., 2007, Numerical models of Saturn's long-lived anticyclones, *Icarus*, 191, 665 – 677
- García-Melendo, E., Sánchez-Lavega, A., Rojas, J., Pérez-Hoyos, S., Hueso, R., 2009, Vertical shears in Saturn's eastward jets at cloud level, *Icarus*, 201, 818 – 820
- García-Melendo, E., Sánchez-Lavega, A., Rojas, J. F., Pérez-Hoyos, S., Hueso, R., 2009, Vertical shears in Saturn's eastward jets at cloud level, *Icarus*, 201, 818 – 820
- García-Melendo, E., Sánchez-Lavega, A., Legarreta, J., Perez-Hoyos, S., Hueso, R., 2010, A strong high altitude narrow jet detected at Saturn's equator, *Geophysical Research Letters*, 37

- Gavrilov, M. B., Tošić, I. A., 1998, Propagation of the Rossby waves on two dimensional rectangular grids, *Meteorology and Atmospheric Physics*, 68, 119–125
- Gibbard, S., Levy, E. H., Lunine, J. I., 1995, Generation of lightning in Jupiter's water cloud, *Nature*, 378, 592–595
- Gierasch, P. J., 1991, Jupiter's stratosphere mapped, *Nature*, 351, 103–104
- Gierasch, P. J., 1996a, Dynamics of the atmosphere of Jupiter, *Endeavour*, 20, 144 – 149
- Gierasch, P. J., 1996b, Dynamics of the atmosphere of Jupiter, *Endeavour*, 20, 144 – 149
- Gierasch, P. J., 2004, Stability of jets on Jupiter and Saturn, *Icarus*, 167, 212 – 219
- Gierasch, P. J., Conrath, B. J., 1993, Dynamics of the atmospheres of the outer planets: Post-Voyager measurement objectives, *Journal of Geophysical Research: Planets*, 98, 5459–5469
- Gierasch, P. J., Conrath, B. J., Magalhães, J. A., 1986, Zonal mean properties of Jupiter's upper troposphere from voyager infrared observations, *Icarus*, 67, 456 – 483
- Gierasch, P. J., Ingersoll, A. P., Banfield, D., Ewald, S. P., Helfenstein, P., Simon-Miller, A., Vasavada, A., Breneman, H. H., Senske, D. A., Galileo Imaging Team, 2000, Observation of moist convection in Jupiter's atmosphere, *Nature*, 403, 628–630
- Golitsyn, G. S., 1979, Atmospheric dynamics on the outer planets and some of their satellites, *Icarus*, 38, 333 – 341
- Grasset, O., Dougherty, M. K., Coustenis, A., Bunce, E. J., Erd, C., Titov, D., Blanc, M., Coates, A., Drossart, P., Fletcher, L. N., Hussmann, H., Jaumann, R., Krupp, N., Lebreton, J. P., Prieto-Ballesteros, O., Tortora, P., Tosi, F., Hoolst, T. V., 2013, JUPITER ICy moons Explorer (JUICE): An ESA mission to orbit Ganymede and to characterise the Jupiter system, *Planetary and Space Science*, 78, 1 – 21
- Greathouse, T. K., Lacy, J. H., Bézard, B., Moses, J. I., Griffith, C. A., Richter, M. J., 2005, Meridional variations of temperature, C_2H_2 and C_2H_6 abundances in Saturn's stratosphere at southern summer solstice, *Icarus*, 177, 18 – 31
- Guerlet, S., Fouchet, T., Bézard, B., Simon-Miller, A. A., Flasar, F. M., 2009, Vertical and meridional distribution of ethane, acetylene and propane in Saturn's stratosphere from CIRS/Cassini limb observations, *Icarus*, 203, 214 – 232
- Guerlet, S., Fouchet, T., Bézard, B., Moses, J. I., Fletcher, L. N., Simon-Miller, A. A., Flasar, F. M., 2010, Meridional distribution of CH_3C_2H and C_4H_2 in Saturn's stratosphere from CIRS/Cassini limb and nadir observations, *Icarus*, 209, 682 – 695
- Guerlet, S., Fouchet, T., Bézard, B., Flasar, F. M., Simon-Miller, A. A., 2011, Evolution of the equatorial oscillation in Saturn's stratosphere between 2005 and 2010 from Cassini/CIRS limb data analysis, *Geophysical Research Letters*, 38

- Guillot, T., 2005, THE INTERIORS OF GIANT PLANETS: Models and Outstanding Questions, *Annual Review of Earth and Planetary Sciences*, 33, 493–530
- Hanel, R. A., Conrath, B. J., Herath, L. W., Kunde, V. G., Pirraglia, J. A., 1981, Albedo, internal heat, and energy balance of Jupiter: Preliminary results of the Voyager Infrared Investigation, *Journal of Geophysical Research: Space Physics*, 86, 8705–8712
- Hanel, R. A., Conrath, B. J., Kunde, V. G., Pearl, J. C., Pirraglia, J. A., 1983, Albedo, internal heat flux, and energy balance of Saturn, *Icarus*, 53, 262 – 285
- Hartogh, P., Medvedev, A. S., Kuroda, T., Saito, R., Villanueva, G., Feofilov, A. G., Kutepov, A. A., Berger, U., 2005, Description and climatology of a new general circulation model of the Martian atmosphere, *J. Geophys. Res.*, 110,E11008
- Hartogh, P., Lellouch, E., Crovisier, J., Banaszkiwicz, M., Bensch, F., Bergin, E. A., Billebaud, F., Biver, N., Blake, G. A., Blecka, M. I., Blommaert, J., Bockelée-Morvan, D., Cavalié, T., Cernicharo, J., Courtin, R., Davis, G., Decin, L., Encrenaz, P., Encrenaz, T., González, A., de Graauw, T., Hutsemékers, D., Jarchow, C., Jehin, E., Kidger, M., Küppers, M., de Lange, A., Lara, L.-M., Lis, D. C., Lorente, R., Manfroid, J., Medvedev, A. S., Moreno, R., Naylor, D. A., Orton, G., Portyankina, G., Rengel, M., Sagawa, H., Sánchez-Portal, M., Schieder, R., Sidher, S., Stam, D., Swinyard, B., Sztutowicz, S., Thomas, N., Thornhill, G., Vandenbussche, B., Verdugo, E., Waelkens, C., Walker, H., 2009, Water and related chemistry in the solar system. A guaranteed time key programme for Herschel, *Planetary and Space Science*, 57, 1596–1606
- Hartogh, P., Lellouch, E., Moreno, R., Bockelée-Morvan, D., Biver, N., Cassidy, T., Rengel, M., Jarchow, C., Cavalié, T., Crovisier, J., Helmich, F. P., Kidger, M., 2011, Direct detection of the Enceladus water torus with Herschel, *Astron. and Astrophys.*, 532, L2
- Heimpel, M., Aurnou, J., Wicht, J., 2005, Simulation of equatorial and high-latitude jets on Jupiter in a deep convection model, *Nature*, 438, 193–196
- Helled, R., Schubert, G., Anderson, J. D., 2009, Jupiter and Saturn rotation periods, *Planetary and Space Science*, 57, 1467 – 1473
- Hesman, B. E., Jennings, D. E., Sada, P. V., BJORAKER, G. L., Achterberg, R. K., Simon-Miller, A. A., Anderson, C. M., Boyle, R. J., Nixon, C. A., Fletcher, L. N., McCabe, G. H., 2009, Saturn's latitudinal C₂H₂ and C₂H₆ abundance profiles from Cassini/CIRS and ground-based observations, *Icarus*, 202, 249 – 259
- Hickey, M. P., Walterscheid, R. L., Schubert, G., 2000, Gravity Wave Heating and Cooling in Jupiter's Thermosphere, *Icarus*, 148, 266 – 281
- Holton, J. R., 1975, The dynamic meteorology of the stratosphere and mesosphere, *Meteorological Monograph*, 15
- Hueso, R., Sánchez-Lavega, A., 2004, A three-dimensional model of moist convection for the giant planets II: Saturn's water and ammonia moist convective storms, *Icarus*, 172, 255–271

- Ingersoll, A. P., 1990, Atmospheric dynamics of the outer planets, *Science*, 248, 308–315
- Ingersoll, A. P., Beebe, R. F., Mitchell, J. L., Garneau, G. W., Yagi, G. M., Müller, J., 1981, Interaction of eddies and mean zonal flow on Jupiter as inferred from Voyager 1 and 2 images, *Journal of Geophysical Research: Space Physics*, 86, 8733–8743
- Ingersoll, A. P., Gierasch, P. J., Banfield, D., Vasavada, A. R., Galileo Imaging Team, 2000, Moist convection as an energy source for the large-scale motions in Jupiter's atmosphere, *Nature*, 403, 630–632
- Ingersoll, A. P. et al., 2004, Dynamics of Jupiter's Atmosphere (Ch. 6), in *Jupiter: The Planet, Satellites and Magnetosphere* (eds Bagenal, F., McKinnon, W. and Dowling, T.), Cambridge Univ. Press, Cambridge, pp. 105–128
- Kar, S. K., Turco, R. P., Mechoso, C. R., Arakawa, A., 1994, A Locally One-Dimensional Semi-Implicit Scheme for Global Gridpoint Shallow-Water Models, *Mon. Wea. Rev.*, 122, 205–222
- Karkoschka, E., Tomasko, M., 2005, Saturn's vertical and latitudinal cloud structure 1991–2004 from HST imaging in 30 filters, *Icarus*, 179, 195–221
- Kunde, V. G., Flasar, F. M., Jennings, D. E., Bézard, B., Strobel, D. F., Conrath, B. J., Nixon, C. A., Bjoraker, G. L., Romani, P. N., Achterberg, R. K., Simon-Miller, A. A., Irwin, P., Brasunas, J. C., Pearl, J. C., Smith, M. D., Orton, G. S., Gierasch, P. J., Spilker, L. J., Carlson, R. C., Mamoutkine, A. A., Calcutt, S. B., Read, P. L., Taylor, F. W., Fouchet, T., Parrish, P., Barucci, A., Courtin, R., Coustenis, A., Gautier, D., Lellouch, E., Marten, A., Prangé, R., Biraud, Y., Ferrari, C., Owen, T. C., Abbas, M. M., Samuelson, R. E., Raulin, F., Ade, P., Césarsky, C. J., Grossman, K. U., Coradini, A., 2004, Jupiter's Atmospheric Composition from the Cassini Thermal Infrared Spectroscopy Experiment, *Science*, 305, 1582–1587
- Leovy, C. B., Friedson, A. J., Orton, G. S., 1991, The quasiquadrennial oscillation of Jupiter's equatorial stratosphere, *Nature*, 354, 380–382
- Leslie, L. M., Purser, R. J., 1992, A comparative study of the performance of various vertical discretization schemes, *Meteorology and Atmospheric Physics*, 50, 61–73
- Li, L., Ingersoll, A. P., Vasavada, A. R., Porco, C. C., Genio, A. D. D., Ewald, S. P., 2004, Life cycles of spots on Jupiter from Cassini images, *Icarus*, 172, 9 – 23
- Li, L., Ingersoll, A. P., Huang, X., 2006a, Interaction of moist convection with zonal jets on Jupiter and Saturn, *Icarus*, 180, 113 – 123
- Li, L., Ingersoll, A. P., Vasavada, A. R., Simon-Miller, A. A., Achterberg, R. K., Ewald, S. P., Dyudina, U. A., Porco, C. C., West, R. A., Flasar, F. M., 2006b, Waves in Jupiter's atmosphere observed by the Cassini ISS and CIRS instruments, *Icarus*, 185, 416 – 429
- Li, L., Ingersoll, A. P., Vasavada, A. R., Simon-Miller, A. A., Del Genio, A. D., Ewald, S. P., Porco, C. C., West, R. A., 2006c, Vertical wind shear on Jupiter from Cassini images, *Journal of Geophysical Research (Planets)*, 111

- Li, L., Jiang, X., Ingersoll, A. P., Del Genio, A. D., Porco, C. C., West, R. A., Vasavada, A. R., Ewald, S. P., Conrath, B. J., Gierasch, P. J., Simon-Miller, A. A., Nixon, C. A., Achterberg, R. K., Orton, G. S., Fletcher, L. N., Baines, K. H., 2011, Equatorial winds on Saturn and the stratospheric oscillation, *Nature Geoscience*, 4, 750–752
- Li, X., Read, P. L., 2000, A mechanistic model of the quasi-quadrennial oscillation in Jupiter's stratosphere, *Planetary and Space Science*, 48, 637 – 669
- Lian, Y., Showman, A. P., 2010, Generation of equatorial jets by large-scale latent heating on the giant planets, *Icarus*, 207, 373 – 393
- Liang, M., Shia, R., Lee, A. Y., Allen, M., Friedson, A. J., Yung, Y. L., 2005, Meridional Transport in the Stratosphere of Jupiter, *The Astrophysical Journal Letters*, 635
- Liming, L., Gierasch, P. J., Achterberg, R. K., Conrath, B. J., Flasar, F. M., Vasavada, A. R., Ingersoll, A. P., Banfield, D., Simon-Miller, A. A., Fletcher, L. N., 2008, Strong jet and a new thermal wave in Saturn's equatorial stratosphere, *Geophysical Research Letters*, 35
- Lindzen, R. S. and Holton, J. R., 1968, A Theory of the Quasi-Biennial Oscillation, *Journal of Atmospheric Sciences*, 25, 1095–1107
- Liu, J., Schneider, T., 2010, Mechanisms of Jet Formation on the Giant Planets, *J. Atmos. Sci.*, 67, 3652–3672
- Magalhães, J. A., Weir, A. L., Conrath, B. J., Gierasch, P. J., Leroy, S. S., 1990, Zonal motion and structure in Jupiter's upper troposphere from voyager infrared and imaging observations, *Icarus*, 88, 39 – 72
- Manabe, S., Strickler, R. F., 1964, Thermal Equilibrium of the Atmosphere with a Convective Adjustment, *Journal of Atmospheric Sciences*, 21, 361–385
- Marchuk, G. I., Dymnikov, V. P., Zalesny, V. B., Lykossov, V. N., Galin, V. Y., 1987, *Mathematical Modeling of the General Ocean and Atmosphere Circulation*, Springer-Verlag, New York
- Matcheva, K. I., Strobel, D. F., 1999, Heating of Jupiter's Thermosphere by Dissipation of Gravity Waves Due to Molecular Viscosity and Heat Conduction, *Icarus*, 140, 328 – 340
- Matcheva, K. I., Conrath, B. J., Gierasch, P. J., Flasar, F. M., 2005, The cloud structure of the jovian atmosphere as seen by the Cassini/CIRS experiment, *Icarus*, 179, 432 – 448
- Medvedev, A. S., Sethunadh, J., Hartogh, P., 2013, From cold to warm gas giants: A three-dimensional atmospheric general circulation modeling, *Icarus*, 225, 228 – 235
- Menou, K., Rauscher, E., 2009, Atmospheric Circulation of Hot Jupiters: A Shallow Three-Dimensional Model, *ApJ*, 700, 887–897

- Moreno, F., Sedano, J., 1997, Radiative Balance and Dynamics in the Stratosphere of Jupiter: Results from a Latitude-Dependent Aerosol Heating Model, *Icarus*, 130, 36 – 48
- Moses, J. I., Greathouse, T. K., 2005, Latitudinal and seasonal models of stratospheric photochemistry on Saturn: Comparison with infrared data from IRTF/TEXES, *Journal of Geophysical Research: Planets*, 110
- Moses, J. I., Bézard, B., Lellouch, E., Gladstone, G. R., Feuchtgruber, H., Allen, M., 2000, Photochemistry of Saturn's Atmosphere: I. Hydrocarbon Chemistry and Comparisons with ISO Observations, *Icarus*, 143, 244 – 298
- Niemann, H. B., Atreya, S. K., Carignan, G. R., Donahue, T. M., Haberman, J. A., Harpold, D. N., Hartle, R. E., Hunten, D. M., Kasprzak, W. T., Mahaffy, P. R., Owen, T. C., Way, S. H., 1998, The composition of the Jovian atmosphere as determined by the Galileo probe mass spectrometer, *Journal of Geophysical Research: Planets*, 103, 22 831–22 845
- Nixon, C. A., Achterberg, R. K., Conrath, B. J., Irwin, P. G. J., Teanby, N. A., Fouchet, T., Parrish, P. D., Romani, P. N., Abbas, M., LeClair, A., Strobel, D., Simon-Miller, A. A., Jennings, D. J., Flasar, F. M., Kunde, V. G., 2007, Meridional variations of C₂H₂ and C₂H₆ in Jupiter's atmosphere from Cassini CIRS infrared spectra, *Icarus*, 188, 47 – 71
- Ollivier, J. L., Dobrijévić, M., Parisot, J. P., 2000, New photochemical model of Saturn's atmosphere, *Planetary and Space Science*, 48, 699 – 716
- Orton, G. S., Friedson, A. J., Caldwell, J., Hammel, H. B., Baines, K. H., Bergstralh, J. T., Martin, T. Z., Malcom, M. E., West, R. A., Golisch, W. F., Griep, D. M., Kaminiski, C. D., Tokunaga, A. T., Baron, R., Shure, M., 1991, Thermal maps of Jupiter - Spatial organization and time dependence of stratospheric temperatures, 1980 to 1990, *Science*, 252, 537–542
- Orton, G. S., Yanamandra-Fisher, P. A., Fisher, B. M., Friedson, A. J., Parrish, P. D., Nelson, J. F., Bauermeister, A. S., Fletcher, L., Gezari, D. Y., Varosi, F., Tokunaga, A. T., Caldwell, J., Baines, K. H., Hora, J. L., Ressler, M. E., Fujiyoshi, T., Fuse, T., Hagopian, H., Martin, T. Z., Bergstralh, J. T., Howett, C., Hoffmann, W. F., Deutsch, L. K., van Cleve, J. E., Noe, E., Adams, J. D., Kassis, M., Tollestrup, E., 2008, Semi-annual oscillations in Saturn's low-latitude stratospheric temperatures, *Nature*, 453, 196–199
- Pearl, J. C., Conrath, B. J., 1991, The albedo, effective temperature, and energy balance of Neptune, as determined from Voyager data, *Journal of Geophysical Research: Space Physics*, 96, 18 921–18 930
- Pérez-Hoyos, S., Sánchez-Lavega, A., French, R. G., Rojas, J. F., 2005, Saturn's cloud structure and temporal evolution from ten years of Hubble Space Telescope images (1994-2003), *Icarus*, 176, 155–174

- Pérez-Hoyos, S., Sanz-Requena, J., Barrado-Izagirre, N., Rojas, J., Sánchez-Lavega, A., 2012, The 2009-2010 fade of Jupiter's South Equatorial Belt: Vertical cloud structure models and zonal winds from visible imaging, *Icarus*, 217, 256 – 271
- Pirraglia, J., 1984, Meridional energy balance of Jupiter, *Icarus*, 59, 169 – 176
- Plumb, R. A., 2002, Stratospheric Transport, *Journal of the Meteorological Society of Japan. Ser. II*, 80, 793–809
- Porco, C. C., West, R. A., McEwen, A., Del Genio, A. D., Ingersoll, A. P., Thomas, P., Squyres, S., Dones, L., Murray, C. D., V. Johnson, T., Burns, J. A., Brahic, A., Neukum, G., Veverka, J., Barbara, J. M., Denk, T., Evans, M., Ferrier, J. J., Geissler, P., Helfenstein, P., Roatsch, T., Throop, H., Tiscareno, M., Vasavada, A. R., 2003, Cassini Imaging of Jupiter's Atmosphere, Satellites, and Rings, *Science*, 299, 1541–1547
- Rages, K., Beebe, R., Senske, D., 1999, Jovian Stratospheric Hazes: The High Phase Angle View from Galileo, *Icarus*, 139, 211–226
- Ramanathan, V., Coakley, J. A., 1978, Climate modeling through radiative-convective models, *Reviews of Geophysics*, 16, 465–489
- Rauscher, E., Menou, K., 2010, Three-dimensional Modeling of Hot Jupiter Atmospheric Flows, *ApJ*, 714, 1334–1342
- Read, P. L., Conrath, B. J., Fletcher, L. N., Gierasch, P. J., Simon-Miller, A. A., Zuchowski, L. C., 2009, Mapping potential vorticity dynamics on Saturn: Zonal mean circulation from Cassini and Voyager data, *Planetary and Space Science*, 57, 1682 – 1698
- Reuter, D. C., Simon-Miller, A. A., Lunsford, A., Baines, K. H., Cheng, A. F., Jennings, D. E., Olkin, C. B., Spencer, J. R., Stern, S. A., Weaver, H. A., Young, L. A., 2007, Jupiter Cloud Composition, Stratification, Convection, and Wave Motion: A View from New Horizons, *Science*, 318, 223
- Rhines, P. B., 1975, Waves and turbulence on a beta-plane, *Journal of Fluid Mechanics*, 69, 417–443
- Roman, M. T., Banfield, D., Gierasch, P. J., 2013, Saturn's cloud structure inferred from Cassini ISS, *Icarus*, 225, 93–110
- Saito, R., 2006, Influence of the Surface on the Atmospheric Circulation of Mars: Study with a General Circulation Model, Ph. D Thesis, Technische Universität Braunschweig, ISBN 978-3-936586-72-5
- Salyk, C., Ingersoll, A. P., Lorre, J., Vasavada, A., Genio, A. D. D., 2006, Interaction between eddies and mean flow in Jupiter's atmosphere: Analysis of Cassini imaging data, *Icarus*, 185, 430 – 442
- Sanchez-Lavega, A., 2002, Observations of Saturn's Ribbon Wave 14 Years after Its Discovery, *Icarus*, 158, 272–275

- Sánchez-Lavega, A., Acarreta, J., Hueso, R., Rojas, J., Lecacheux, J., Colas, F., Gómez, J., 1998, An Overview of Saturn's Equatorial Storms: 1990 - 1997, *Astrophysics and Space Science*, 263, 351–354
- Sanchez-Lavega, A., Hueso, R., Ramón Acarreta, J., 1998, A system of circumpolar waves in Jupiter's stratosphere, *Geophysical Research Letters*, 25, 4043–4046
- Sanchez-Lavega, A., Orton, G. S., Morales, R., Lecacheux, J., Colas, F., Fisher, B., Fukumura-Sawada, P., Golisch, W., Griep, D., Kaminski, C., Baines, K., Rages, K., West, R., 2001, The Merger of Two Giant Anticyclones in the Atmosphere of Jupiter, *Icarus*, 149, 491 – 495
- Sánchez-Lavega, A., Pérez-Hoyos, S., Rojas, J. F., Hueso, R., French, R. G., 2003, A strong decrease in Saturn's equatorial jet at cloud level, *Nature*, 423, 623–625
- Sánchez-Lavega, A., Orton, G. S., Hueso, R., García-Melendo, E., Pérez-Hoyos, S., Simon-Miller, A., Rojas, J. F., Gómez, J. M., Yanamandra-Fisher, P., Fletcher, L., Joels, J., Kemerer, J., Hora, J., Karkoschka, E., de Pater, I., Wong, M. H., Marcus, P. S., Pinilla-Alonso, N., Carvalho, F., Go, C., Parker, D., Salway, M., Valimberti, M., Wesley, A., Pujic, Z., 2008, Depth of a strong jovian jet from a planetary-scale disturbance driven by storms, *Nature*, 451, 437–440
- Sánchez-Lavega, A., Orton, G. S., Hueso, R., Pérez-Hoyos, S., Fletcher, L. N., García-Melendo, E., Gomez-Forrellad, J. M., de Pater, I., Wong, M., Hammel, H. B., Yanamandra-Fisher, P., Simon-Miller, A., Barrado-Izagirre, N., Marchis, F., Mousis, O., Ortiz, J. L., García-Rojas, J., Cecconi, M., Clarke, J. T., Noll, K., Pedraz, S., Wesley, A., Kalas, P., McConnell, N., Golisch, W., Griep, D., Sears, P., Volquardsen, E., Reddy, V., Shara, M., Binzel, R., Grundy, W., Emery, J., Rivkin, A., Thomas, C., Trilling, D., Bjorkman, K., Burgasser, A. J., Campins, H., Sato, T. M., Kasaba, Y., Ziffer, J., Mirzoyan, R., Fitzgerald, M., Bouy, H., International Outer PLANET Watch Team IOPW-PVOL, 2011, Long-term evolution of the aerosol debris cloud produced by the 2009 impact on Jupiter, *Icarus*, 214, 462–476
- Sánchez-Lavega, A., del Río-Gaztelurrutia, T., Delcroix, M., Legarreta, J. J., Gómez-Forrellad, J. M., Hueso, R., García-Melendo, E., Pérez-Hoyos, S., Barrado-Navascués, D., Lillo, J., 2012, Ground-based observations of the long-term evolution and death of Saturn's 2010 Great White Spot, *Icarus*, 220, 561 – 576
- Sayanagi, K. M., Showman, A. P., 2007, Effects of a large convective storm on Saturn's equatorial jet, *Icarus*, 187, 520 – 539
- Sayanagi, K. M., Showman, A. P., Dowling, T. E., 2008, The Emergence of Multiple Robust Zonal Jets from Freely Evolving, Three-Dimensional Stratified Geostrophic Turbulence with Applications to Jupiter, *Journal of Atmospheric Sciences*, 65, 3947
- Sayanagi, K. M., Dyudina, U. A., Ewald, S. P., Fischer, G., Ingersoll, A. P., Kurth, W. S., Muro, G. D., Porco, C. C., West, R. A., 2013, Dynamics of Saturn's great storm of 2010-2011 from Cassini ISS and RPWS, *Icarus*, 223, 460 – 478

- Schinder, P. J., Flasar, F. M., Marouf, E. A., French, R. G., McGhee, C. A., Kliore, A. J., Rappaport, N. J., Barbinis, E., Fleischman, D., Anabtawi, A., 2011, Saturn's equatorial oscillation: Evidence of descending thermal structure from Cassini radio occultations, *Geophysical Research Letters*, 38
- Schlesinger, R. E., Uccellini, L. W., Johnson, D. R., 1983, The Effects of the Asselin Time Filter on Numerical Solutions to the Linearized Shallow-Water Wave Equations, *Monthly Weather Review*, 111
- Schneider, T., Liu, J., 2009, Formation of Jets and Equatorial Superrotation on Jupiter, *Journal of Atmospheric Sciences*, 66, 579
- Schubert, G., Hickey, M. P., Walterscheid, R. L., 2003, Heating of Jupiter's thermosphere by the dissipation of upward propagating acoustic waves, *Icarus*, 163, 398–413
- Seiff, A., 2000, Astronomy: Dynamics of Jupiter's atmosphere, *Nature*, 403, 603–605
- Shapiro, R., 1970, Smoothing, filtering, and boundary effects, *Rev. Geophys. Space Phys.*, 8, 359–387
- Showman, A. P., 2002, Planetary atmospheres: the giant planets and their satellites. in *The Encyclopedia of Atmospheric Science/ Jupiter and the Outer Planets*, in *Encyclopedia of Atmospheric Sciences*, (Ed.) Editor-in-Chief: Holton, J. R., pp. 1730 – 1745, Academic Press, Oxford, ISBN 978-0-12-227090-1
- Showman, A. P., Polvani, L. M., 2011, Equatorial Superrotation on Tidally Locked Exoplanets, *The Astrophysical Journal*, 738, 71
- Showman, A. P., Gierasch, P. J., Lian, Y., 2006, Deep zonal winds can result from shallow driving in a giant-planet atmosphere, *Icarus*, 182, 513–526
- Showman, A. P., Cooper, C. S., Fortney, J. J., Marley, M. S., 2008a, Atmospheric circulation of hot Jupiters: Three-dimensional circulation models of HD 209458b and HD 189733b with simplified forcing, *The Astrophysical J.*, 682, 559–576
- Showman, A. P., Menou, K., Cho, J. Y., 2008b, Atmospheric circulation of hot Jupiters: a review of current understanding. In *Extreme Solar Systems*, *Astron. Soc. Pacific (ASP) Conference Series*, Editors: Fischer, D., Rasio, F. A., Thorsett, S. E., Wolszczan, A. et al.
- Showman, A. P., Fortney, J. J., Lian, Y., Marley, M. S., Freedman, R. S., Knutson, H. A., Charbonneau, D., 2009, Atmospheric Circulation of Hot Jupiters: Coupled Radiative-Dynamical General Circulation Model Simulations of HD 189733b and HD 209458b, *The Astrophysical Journal*, 699, 564
- Showman, A. P., Cho, J. Y-K., Menou, K., 2010, Atmospheric circulation of exoplanets, in *Exoplanets*, Univ. Arizona Press, pp. 471–516
- Simon-Miller, A. A., Gierasch, P. J., 2010, On the long-term variability of Jupiter's winds and brightness as observed from Hubble, *Icarus*, 210, 258 – 269

- Simon-Miller, A. A., Banfield, D., Gierasch, P. J., 2001, Color and the Vertical Structure in Jupiter's Belts, Zones, and Weather Systems, *Icarus*, 154, 459 – 474
- Simon-Miller, A. A., Conrath, B. J., Gierasch, P. J., Orton, G. S., Achterberg, R. K., Flasar, F. M., Fisher, B. M., 2006, Jupiter's atmospheric temperatures: From Voyager IRIS to Cassini CIRS, *Icarus*, 180, 98–112
- Simon-Miller, A. A., Poston, B. W., Orton, G. S., Fisher, B., 2007, Wind variations in Jupiter's equatorial atmosphere: A QO counterpart ?, *Icarus*, 186, 192–203
- Simon-Miller, A. A., Rogers, J. H., Gierasch, P. J., Choi, D., Allison, M. D., Adamoli, G., Mettig, H.-J., 2012, Longitudinal variation and waves in Jupiter's south equatorial wind jet, *Icarus*, 218, 817 – 830
- Sinclair, J. A., Irwin, P. G. J., Fletcher, L. N., Moses, J. I., Greathouse, T. K., Friedson, A. J., Hesman, B., Hurley, J., Merlet, C., 2013, Seasonal variations of temperature, acetylene and ethane in Saturn's atmosphere from 2005 to 2010, as observed by Cassini-CIRS, *Icarus*, 225, 257 – 271
- Smith, B. A., Soderblom, L. A., Johnson, T. V., Ingersoll, A. P., Collins, S. A., Shoemaker, E. M., Hunt, G. E., Masursky, H., Carr, M. H., Davies, M. E., Cook, A. F., Boyce, J. M., Owen, T., Danielson, G. E., Sagan, C., Beebe, R. F., Veverka, J., McCauley, J. F., Strom, R. G., Morrison, D., Briggs, G. A., Suomi, V. E., 1979, The Jupiter System Through the Eyes of Voyager 1, *Science*, 204, 951–972
- Smith, B. A., Soderblom, L., Batson, R. M., Bridges, P. M., Inge, J. L., Masursky, H., Shoemaker, E., Beebe, R. F., Boyce, J., Briggs, G., Bunker, A., Collins, S. A., Hansen, C., Johnson, T. V., Mitchell, J. L., Terrile, R. J., Cook, A. F., Cuzzi, J. N., Pollack, J. B., Danielson, G. E., Ingersoll, A. P., Davies, M. E., Hunt, G. E., Morrison, D., Owen, T., Sagan, C., Veverka, J., Strom, R., Suomi, V. E., 1982, A new look at the Saturn system - The Voyager 2 images, *Science*, 215, 504–537
- Stam, D. M., Banfield, D., Gierasch, P. J., Nicholson, P. D., Matthews, K., 2001, Near-IR Spectrophotometry of Saturnian Aerosols-Meridional and Vertical Distribution, *Icarus*, 152, 407 – 422
- Vasavada, A. R., Showman, A. P., 2005, Jovian atmospheric dynamics: an update after Galileo and Cassini, *Reports on Progress in Physics*, 68, 1935
- Vincent, M. B., Clarke, J. T., Ballester, G. E., Harris, W. M., West, R. A., Trauger, J. T., Evans, R. W., Stapelfeldt, K. R., Crisp, D., Burrows, C. J., III, J. S. G., Griffiths, R. E., Hester, J. J., Hoessel, J. G., Holtzman, J. A., Mould, J. R., Scowen, P. A., Watson, A. M., Westphal, J. A., 2000, Mapping Jupiter's Latitudinal Bands and Great Red Spot Using HST/WFPC2 Far-Ultraviolet Imaging, *Icarus*, 143, 189 – 204
- Weidenschilling, S., Lewis, J., 1973, Atmospheric and cloud structures of the Jovian planets, *Icarus*, 20, 465 – 476
- West, R. A., Friedson, A. J., Appleby, J. F., 1992, Jovian large-scale stratospheric circulation, *Icarus*, 100, 245 – 259

- West, R. A., Karkoschka, E., Friedson, A. J., Seymour, M., Baines, K. H., Hammel, H. B., 1995, Impact Debris Particles in Jupiter's Stratosphere, *Science*, 267, 1296–1301
- West, R. A., Baines, K. H., Karkoschka, E., Sánchez-Lavega, A., 2009, Clouds and Aerosols in Saturn's Atmosphere, In *Saturn from Cassini-Huygens*, ISBN 978-1-4020-9216-9
- Wickett, M. E., Duffy, P. B., Rodrigue, G., 2000, A reduced grid for a parallel global ocean general circulation model, *Ocean Modelling*, 2, 85 – 107
- Williams, G. P., 2003, Jovian Dynamics. Part III: Multiple, Migrating, and Equatorial Jets, *Journal of the Atmospheric Sciences*, 60, 1270
- Williams, P., 2011, The RAW filter: An improvement to the Robert-Asselin filter in semi-implicit integrations, *Mon. Wea. Rev.*, 139, 1996–2007
- Williams, P. D., 2009, A Proposed Modification to the Robert-Asselin Time Filter, *Monthly Weather Review*, 137, 2538
- Wu, Z., Battisti, D. S., Sarachik, E. S., 2000, Rayleigh Friction, Newtonian Cooling, and the Linear Response to Steady Tropical Heating, *Journal of Atmospheric Sciences*, 57, 1937–1957
- Yamazaki, Y. H., Skeet, D. R., Read, P. L., 2004, A new general circulation model of Jupiter's atmosphere based on the UKMO Unified Model: Three-dimensional evolution of isolated vortices and zonal jets in mid-latitudes, *Planetary and Space Science*, 52, 423 – 445
- Yano, J., Talagrand, O., Drossart, P., 2003, Outer planets: Origins of atmospheric zonal winds, *Nature*, 421, 36
- Yano, J.-I., 1994, A critical review on the dynamics of Jovian atmospheres, *Chaos*, 4, 287–297
- Yelle, R. V., Griffith, C. A., Young, L. A., 2001, Structure of the Jovian Stratosphere at the Galileo Probe Entry Site, *Icarus*, 152, 331 – 346
- Yiğit, E., Aylward, A. D., Medvedev, A. S., 2008, Parameterization of the effects of vertically propagating gravity waves for thermosphere general circulation models: Sensitivity study, *J. Geophys. Res.*, 113
- Young, L. A., Yelle, R. V., Young, R., Seiff, A., Kirk, D. B., 1997, Gravity waves in Jupiter's thermosphere, *Science*, 276, 108–111
- Young, L. A., Yelle, R. V., Young, R., Seiff, A., Kirk, D. B., 2005, Gravity waves in Jupiter's stratosphere, as measured by the Galileo ASI experiment, *Icarus*, 173, 185 – 199
- Young, R. E., 2003, The Galileo probe: how it has changed our understanding of Jupiter, *New Astronomy Reviews*, 47, 1 – 51

- Young, R. E., Smith, M. A., Sobeck, C. K., 1996, Galileo Probe: In situ Observations of Jupiter's Atmosphere, *Science*, 272, 837–838
- Zhang, X., West, R., Banfield, D., Yung, Y., 2013, Stratospheric aerosols on jupiter from cassini observations, *Icarus*, 226, 159–171
- Zuchowski, L., Yamazaki, Y., Read, P., 2009a, Modeling Jupiter's cloud bands and decks: 2. Distribution and motion of condensates, *Icarus*, 200, 563 – 573
- Zuchowski, L. C., Yamazaki, Y. H., Read, P. L., 2009b, Modeling Jupiter's cloud bands and decks: 1. Jet scale meridional circulations, *Icarus*, 200, 548 – 562

Acknowledgements

First and foremost I would like to thank my supervisor Dr. Alexander S. Medvedev for his guidance at all stages of this work and sharing of immense knowledge in the subject. I greatly appreciate his patience, thoughtful consideration and prompt responses to my questions and queries. Moreover, I learned the best coding practices, a great deal about the models and the theory of the general circulation of the atmospheres from him. He has been a constant pillar of support throughout my PhD. Without his guidance, support and inspiration, I would not have been able to complete this work successfully.

I am particularly indebted to my supervisor Dr. Paul Hartogh for his support, encouragement and valuable scientific advices at all stages of my PhD work. His vast experience helped my PhD work in various ways. I express my sincere indebtedness to him for giving me a unique opportunity to develop a new three-dimensional GCM. I owe a great debt of gratitude for his help during critical periods of my PhD journey and I am very grateful for the motivation, support and his willingness to act as a referee to make this PhD thesis a possibility.

I thankfully extend my deep sense of gratitude to Prof. Dr. Heike Rauer for accepting me as a PhD student in the Technische Universität Berlin. I am grateful for all considerations, helps and supports given to me throughout my PhD. I greatly appreciate for her prompt replies to my queries and for always being very kind.

I take this opportunity to thank Dr. Bernhard Bandow for his suggestions to optimizing the code for efficient computing and Dr. Ladi Rezac for his helpful discussions. I would also like to thank Prof. Naoki Terada, Tohoku University for giving me access to the SX-9 computational facility.

I am especially thankful to my friends and colleagues for their support and encouragement on all fronts. I acknowledge the support of this PhD work by Max Planck Institute for Solar System Research (MPS) and the "International Max Planck Research School (IMPRS) on Physical Processes in the Solar System and Beyond" through my PhD fellowship.

Last, but by no means least, I would like to thank my family for their love, support and encouragement.

Jisesh Ajitha Sethunadh: Three-dimensional modeling of the stratospheres of gas giants

Stratospheres of giant gas planets of the Solar System (Jupiter and Saturn) extend above the cloud top layers near the tropopause to the lower thermosphere. Their stratospheric dynamics are poorly understood, and are very distinctive from that of terrestrial-like planets due to peculiarities of the gas giants: the size, fast rotation, absence of solid surfaces, weak radiative forcing, and strong influence of the interiors.

The main objectives of this work were to develop a three-dimensional general circulation model (GCM) suitable for simulating the stratospheres of gas giants, and to apply it for studying the global circulations in the stratospheres of Jupiter, Saturn, and generic extrasolar planets. The simulated mean fields and non-zonal disturbances were compared with available observations, and showed a good agreement in low latitudes, where the model resolution was the most sufficient. The developed GCM showed methodological suitability for studying atmospheric dynamics of giant gas planets under a variety of conditions.



uni-edition

ISBN 978-3-944072-04-3